DTRA-TR-99-42

Technical Report

Radiation Imaging Diagnostic for Plasma Radiation Sources

Approved for public release; distribution is unlimited

May 2004

Prepared for:
Defense Threat Reduction Agency
8725 John J. Kingman Road, MS-6201
Fort Belvoir, VA 22060-6201

BEST AVAILABLE COPY

DSWA-01-96-C-0171

Rahul R. Prasad, et. al

Prepared by:

Alameda Applied Sciences Corporation
2235 Polvorosa Ave., Suite 230
San Leandro, CA 94577

20040616 041

DESTRUCTION NOTICE:

Destroy this report when it is no longer needed.
Do not return to sender.

PLEASE NOTIFY THE DEFENSE THREAT REDUCTION AGENCY, ATTN: BDMI, 8725 JOHN J. KINGMAN ROAD, MS-6201, FT BELVOIR, VA 22060-6201, IF YOUR ADDRESS IS INCORRECT, IF YOU WISH IT DELETED FROM THE DISTRIBUTION LIST, OR IF THE ADDRESSEE IS NO LONGER EMPLOYED BY YOUR ORGANIZATION.

REPORT DOCUMENTATION PAGE

Form Approved

Public reporting burden for this collection of information is estimated to average 1 hour per response, including the time for reviewing instructions, searching existing data sources, gathering and maintaining the data needed, and completing and reviewing the collection of information. Send comments regarding this burden, estimate or any other aspect of this collection of information, including suggestions for reducing this burden, to Washington Headquarters Services, Directorate for Information Operations and Reports, 1215 Jefferson Davis Highway, Suite 1204, Arlington, VA 22202-4302, and to the Office of Management and Budget, Paperwork Reduction Project (0704-0188), Washington, DC 20503.

1. AGENCY USE ONLY *(Leave blank)*	2. REPORT DATE	3. REPORT TYPE AND DATES COVERED
	May 2004	Technical 960912 - 990911

4. TITLE AND SUBTITLE

Radiation Imaging Diagnostic for Plasma Radiation Sources

5. FUNDING NUMBERS

C – DSWA01-96-C-0171
PE – 4662
PR – AB
TA – GE
WU – DH52896

6. AUTHOR(S)

Rahul R. Parasad, Alexander C. Crisman, Steven Gensler, Niansheng Qi and Mahadevan Krishnan

7. PERFORMING ORGANIZATION NAME(S) AND ADDRESS(ES)

Alameda Applied Sciences Corporation
2235 Polvorosa Drive,
San Leandro, CA 94577

8. PERFORMING ORGANIZATION REPORT NUMBER

9. SPONSORING/MONITORING AGENCY NAME(S) AND ADDRESS(ES)

Defense Threat Reduction Agency
8725 John J. Kingman Road, MS-6201
Fort Belvoir, VA 22060-6201

TDNS/Davis

10. SPONSORING/MONITORING AGENCY REPORT NUMBER

DTRA-TR-99-42

11. SUPPLEMENTARY NOTES

This work was sponsored by the Defense Threat Reduction Agency under RDT&E RMC Code B 4662 D AB GE 3E10 25904D.

12a. DISTRIBUTION/AVAILABILITY STATEMENT

Approved for public release, distribution unlimited.

12b. DISTRIBUTION CODE

13. ABSTRACT *(Maximum 200 words)*

This report describes a two-dimensional, time-resolved, x-ray imaging camera. This camera has a detector face that consists of a pixilated, 6x12 array of 72, 1x1x0.5mm discrete diamond detectors. The camera captured x-ray images of Argon z-pinches produced by the Defense Threat Reduction Agency's Double-EAGLE flash x-ray accelerator, located in San Leandro, CA. The Argon z-pinch was imaged on to this array through a pinhole with a 1:1 magnification. A portion of the pinch that was 6x12mm in area was imaged on to the camera faceplate, with spatial resolution of 1mm. The coverage of the pinch may easily be altered by altering the magnification of the pinhole camera. Magnifications >2:1 further improve the spatial resolution, but at the expense of field of coverage. The temporal resolution of the diamonds is <1 ns. Images of K-shell emission (3.1-4 keV) from Argon z-pinches that were resolved to 400 ps, show bright spots of emission that wax and wane along the pinch length. This level of imaging detail in such z-pinches is unprecedented. The diamond detectors are sensitive to radiation down to 5 eV, hence by use of suitable filters, the softer, L-shell emissions from the Argon z-pinch (50-800 eV) may also be imaged.

14. SUBJECT TERMS

X-rays Plasma Radiation Sources Plasma Diagnostics
Imaging Z-pinches

15. NUMBER OF PAGES

88

16. PRICE CODE

17. SECURITY CLASSIFICATION OF REPORT	18. SECURITY CLASSIFICATION OF THIS PAGE	19. SECURITY CLASSIFICATION OF ABSTRACT	20. LIMITATION OF ABSTRACT
UNCLASSIFIED	UNCLASSIFIED	UNCLASSIFIED	SAR

NSN 7540-01-280-5500

Standard Form 298 (Rev. 2-89)
Prescribed by ANSI Sta. 239-1298-102

CONVERSION TABLE

Conversion Factors for U.S. Customary to metric (SI) units of measurement.

MULTIPLY →	BY →	TO GET
TO GET ←	BY ←	DIVIDE

angstrom	1.000 000 x E -10	meters (m)
atmosphere (normal)	1.013 25 x E +2	kilo pascal (kPa)
bar	1.000 000 x E +2	kilo pascal (kPa)
barn	1.000 000 x E -28	meter^2 (m^2)
British thermal unit (thermochemical)	1.054 350 x E +3	joule (J)
calorie (thermochemical)	4.184 000	joule (J)
cal (thermochemical/cm^2)	4.184 000 x E -2	mega joule/m^2 (MJ/m^2)
curie	3.700 000 x E +1	*giga bacquerel (GBq)
degree (angle)	1.745 329 x E -2	radian (rad)
degree Fahrenheit	$t_k = (t°f + 459.67)/1.8$	degree kelvin (K)
electron volt	1.602 19 x E -19	joule (J)
erg	1.000 000 x E -7	joule (J)
erg/second	1.000 000 x E -7	watt (W)
foot	3.048 000 x E -1	meter (m)
foot-pound-force	1.355 818	joule (J)
gallon (U.S. liquid)	3.785 412 x E -3	meter^3 (m^3)
inch	2.540 000 x E -2	meter (m)
jerk	1.000 000 x E +9	joule (J)
joule/kilogram (J/kg) radiation dose absorbed	1.000 000	Gray (Gy)
kilotons	4.183	terajoules
kip (1000 lbf)	4.448 222 x E +3	newton (N)
kip/inch^2 (ksi)	6.894 757 x E +3	kilo pascal (kPa)
ktap	1.000 000 x E +2	newton-second/m^2 ($N-s/m^2$)
micron	1.000 000 x E -6	meter (m)
mil	2.540 000 x E -5	meter (m)
mile (international)	1.609 344 x E +3	meter (m)
ounce	2.834 952 x E -2	kilogram (kg)
pound-force (lbs avoirdupois)	4.448 222	newton (N)
pound-force inch	1.129 848 x E -1	newton-meter (N-m)
pound-force/inch	1.751 268 x E +2	newton/meter (N/m)
pound-force/foot^2	4.788 026 x E -2	kilo pascal (kPa)
pound-force/inch^2 (psi)	6.894 757	kilo pascal (kPa)
pound-mass (lbm avoirdupois)	4.535 924 x E -1	kilogram (kg)
pound-mass-foot^2 (moment of inertia)	4.214 011 x E -2	kilogram-meter^2 ($kg-m^2$)
pound-mass/foot^3	1.601 846 x E +1	kilogram-meter^3 (kg/m^3)
rad (radiation dose absorbed)	1.000 000 x E -2	**Gray (Gy)
roentgen	2.579 760 x E -4	coulomb/kilogram (C/kg)
shake	1.000 000 x E -8	second (s)
slug	1.459 390 x E +1	kilogram (kg)
torr (mm Hg, 0^0 C)	1.333 22 x E -1	kilo pascal (kPa)

*The bacquerel (Bq) is the SI unit of radioactivity; 1 Bq = 1 event/s.
**The Gray (GY) is the SI unit of absorbed radiation.

Table of Contents

Section Page

Conversion Table ii
Figures iv

1 INTRODUCTION 1

2 CAMERA DESIGN AND PRINCIPLE OF OPERATION 3

2.1 Design of the Camera 3
2.2 Assembly of the Diamond Camera 11
2.3 Principle of Operation 16

3 EARLY EXPERIMENTS 18

3.1 Design of the 3X3 Prototype Camera 18
3.2 Fabrication of the 3X3 Prototype Camera 21
3.3 Crosstalk 22

3.3.1 Crosstalk Calculation 22
3.3.2 Circuits for Modeling Crosstalk 23
3.3.3 Estimate of Capacitance and Inductance between a Pair of Assemblies 24
3.3.4 Calculated Crosstalk from Capacitive and Inductive Coupling 25
3.3.5 Experimental Measurement of Crosstalk 26

3.4 Test of the 3X3 Array on DM2 28

4 Bias Circuit 37

5 Calibration at Sandia National Laboratory 39

6 Camera Validation on Double-Eagle 50

6.1 Design of Double-Eagle Beam Line 51
6.2 Spatial Resolution 54
6.3 Temporal Resolution 59
6.4 Comparison of K-shell and K+L Shell Images 62
6.5 Effect of Magnification 64
6.6 Cable Multiplexing 66

7 Conclusion 68

7.1 Second Calibration at SNL 68
7.2 Future Work 72

8 REFERENCES 77

DISTRIBUTION LIST DL-1

Figures

Figure		Page
2-1	Photograph of diamond camera	3
2-2	Photograph of diamond camera with housing removed	4
2-3	Schematic drawing of the camera	5
2-4	Engineering drawing of the vacuum feed-through flare.	7
2-5	Engineering drawing of the plate that houses the Suhner MMCX connectors	8
2-6	Engineering drawing of the diamond array holder plate	9
2-7	Schematic drawing for the "Intermediary Plate" situated within Module 1.	10
2-8	Schematic drawing of the housing of the diamond camera	10
2-9	Vacuum feed-through flange	11
2-10	Schematic drawing of a pair of stainless steel shims	11
2-11	Schematic drawing of a diamond-shim assembly: it is essentially a pair of stainless steel shims soldered to a diamond pixel	12
2-12	Suhner connector and cable (from Microstock) used in the diamond detector assembly	12
2-13	Schematic drawing of a diamond detector assembly	13
2-14	Photograph of a diamond detector assembly	14
2-15	Side view picture revealing the organizing property of the "Intermediary Plate"	15
2-16	Top view of the diamond array. The scale shows dimensions in mm	15
2-17	Schematic drawing showing a diamond metal-insulator-metal detector	16
3-1	Drawing of the 3x3 prototype diamond camera	18
3-2	Photographs of the diamond assemblies	19
3-3	Vacuum flange with 9 Lemo jack-jack connectors	19
3-4	Bulkhead plate for the Microtech connectors	20
3-5	The diamond detector support plate	20
3-6	Photographs of the 3x3 prototype diamond camera. Entire assembly (top) and detail of the detector array (bottom)	21
3-7	The Bias Circuit for a Diamond Radiation Detector	22
3-8	Circuit for the Capacitive Coupling Calculation	23
3-9	Circuit for the Inductive Coupling Calculation	23
3-10	Pixel orientations: EDGE TO EDGE and FACE TO FACE and a slide view of the assembly showing the height of the coupling region	24
3-11	Diagrams of the experimental circuit elements	26
3-12	Measured crosstalk signals: Face to Face orientation	27
3-13	Measured crosstalk signals: Edge to Edge orientation	27
3-14	Schematic diagram showing the pixel numbering in the 3x3 array	28
3-15	Signals recorded on channels 1 through 4 on DM2 shot 518. The signals on channel 1 and 3 were clipped	29

Figures (Continued)

Figure		Page
3-16	Signals recorded on channels 5 through 9 on DM2 shot 518. Channel 6 produced no signal and is not displayed.	29
3-17	Pixel 4 signal from DM2 shot 518 shown with an expanded time scale.	30
3-18	Low pass filtered signals recorded on channels 1 through 4 (solid curves) superimposed upon the raw signals (dashed curves) recorded for shot 518.	31
3-19	Low pass filtered signals recorded on channels 5 through 9 (solid curves) superimposed upon the raw signals recorded (dashed curves) for shot 518.	31
3-20	Corrected signals from pixels 1 through 4 on DM2 shot 518 using the correction algorithm described in the text. Note the flat baselines.	32
3-21	Corrected signals from pixels 5 through 9 on DM2 shot 518 using the correction algorithm described in the text. Note the flat baselines.	33
3-22	Signals digitized from pixels 1 through 4 on DM2 shot 524. As described in the text only pixel 3 from this set was biased.	33
3-23	Signals digitized from pixels 5 through 9 on DM2 shot 524. As described in the text only pixel 5 from this set was biased.	34
3-24	Corrected signals from pixels 1 through 4 on DM2 shot 524 using the correction algorithm described in the text.	35
3-25	Corrected signals from pixels 5 through 9 on DM2 shot 524 using the correction algorithm described in the text.	35
4-1	Layout of the 75 channel bias circuit and housing.	37
4-2	Data showing a fast pulse measured directly using a Tektronix SCD5000 5 GHz digital oscilloscope (solid curve) and passing through the detector bias circuit (dashed curve).	38
5-1	X-ray output from the laser plasma source at SNL, measured by the calibrated SNL PIN diode.	39
5-2	X-ray output from the laser plasma source at SNL, measured by one of the diamond detectors within the diamond camera.	41
5-3	Sensitivity of pixels 1,1 through 3,12 in the diamond camera.	43
5-4	Sensitivity of pixels 1,1 through 1,8. Data from both sets of shots are shown.	44
5-5	Sensitivity of pixels 1,9 through 3,12 in the diamond camera.	46
5-6	Sensitivity of pixels 4,1 through 6,12 in the diamond camera.	47
5-7	AASC standard diamond radiation detector.	49
6-1	Schematic of the beam line used for the validation tests on Double-EAGLE.	52
6-2	Schematic drawing showing the pinhole mount at the end of the 2.75" conflat flange.	53
6-3	Schematic showing the beam line layout on Double-EAGLE and the beam line used for the diamond camera during the validation tests.	54
6-4	Ar L-shell spectrum and the transmission of 2 μm of aluminized Kimfol.	55
6-5	Ar L-shell spectrum as transmitted through the 2 μm Kimfol filter and the transmission of the Kimfol.	55
6-6	Integrated Ar L-shell spectrum in front of the Kimfol filters, behind 1 μm of Kimfol and behind 2 μm of Kimfol.	56

Figures (Continued)

Figure		Page
6-7	Sequence of K+L shell images from shot 4067.	57
6-8	Comparison of the MPI "zipper array" image and the radially integrated z vs. t image obtained with the diamond camera. The MPI image is courtesy of Drs. J. Levine and J. Riordan of MPI.	58
6-9	Sequence of four K+L shell images from shot 4066.	60
6-10	Three 400ps frames from shot 4066, separated by 0, 800 ps and 2.8 ns.	61
6-11	A composite 5 ns frame created from the 400 ps images acquired in shot 4066, incorporating the three frames showed in Figure 6-10.	61
6-12	Sequence of four K-shell images from shot 4063.	62
6-13	400 ps frames at the peak of x-ray output from two shots. The frame on the upper half is a K+L image, the frame on the lower half a K-shell image.	63
6-14	Sequence of four K-shell images from shot 4060, acquired with 1:1 magnification.	64
6-15	Comparison of two 400 ps at the peak of x-ray output. The image in the upper was acquired with 1:2.3 de-magnification, the image in the lower half with 1:1 magnification.	65
6-16	Temporal trace of a single pixel from the diamond camera (black) superimposed on a multiplexed trace (red) consisting of the original trace (left peak) and a ≈120 ns delayed version of the trace (right peak).	67
7-1	Photograph showing shipping damage to the diamond camera.	69
7-2	Photograph showing damage to the detector array face.	69
7-3	Comparison of the sensitivity of five AASC diamond radiation detectors measured in September 1998 and in June 1999.	70
7-4	X-ray output from the laser plasma calibration source as measured by a DRD. The upper trace was acquired in 1998 at 200 ps/sample. The lower trace was acquired in 1999 at 100 ps/sample.	71
7-5	Calibration factors for pixels 1,1 through 3,4.	73
7-6	Calibration factors for pixels 3,5 through 5,4.	74
7-7	Calibration factors for pixels 5,5 through 6,12.	75
7-8	Suggested configuration of double slits to image both the K and K+L shell emissions on a single shot.	76

Table		
3-1	Peak signals measured on Shot 524 and their ratios to the peaks of pixels 3 and 5	36
5-1	Ratio of output measured along the diamond camera beam line and the reference beam	41
5-2	Average sensitivity of each pixel of the diamond camera	48
5-3	Sensitivity of five diamond radiation detectors also calibrated at Sandia	49

Section 1

Introduction

Alameda Applied Sciences Corporation (AASC) was awarded this contract, effective September 12, 1996, to develop a diamond radiation imaging camera for plasma radiation sources. This camera has a detector face that consists of an array of 72, 1×1×0.5 mm diamonds, configured as a 6×12 array of 72 discrete detectors. The program to build, test, refine, and deliver the radiation imaging camera was scheduled to cover a 35 month period ending on August 11, 1999. The diamond camera has been constructed, calibrated and validated. This document is the Final Report of the contract.

The diamond camera has 1 mm x 1 mm pixels that are arranged in a closed packed configuration with an 85% open area. The camera was first calibrated at the Laser Plasma Calibration Laboratory at Sandia National Laboratory and then used to obtain images of Ar implosions on Double-EAGLE. Images of the K-shell and the K+L shell emitting regions of long pulse implosions were obtained with two magnifications: 1:1 and 1:2.3 (demagnification). Data from these tests are shown in later sections.

The highlights of these tests were:

- The camera was clearly able to resolve the ≈1 ns laser produced plasma x-ray pulse at Sandia National Laboratory. The rise time measured was ≈200 ps, limited not by the camera, but by the digitizers available for the test.

- The camera acquired z-pinch images with 400 ps resolution, limited by the digitizers available. The earlier Sandia tests have shown that the camera is capable of imaging z-pinches with <200 ps resolution. Integration over several 400 ps frames was used to create 5 ns frames, typical of gated micro-channel plate (MCP) based time resolved x-ray cameras. These integrated images showed that certain features of the z-pinch dynamics are missed at the poorer temporal resolution offered by the gated MCP instruments. (It should be noted that gated MCPs at Sandia achieve 1 ns frames, but the DTRA inventory typically has 5 ns frames.

- With 1:1 magnification and a 0.5-mm diameter pinhole, the spatial resolution of the camera was shown to be 1 mm. With 4:1 magnification this resolution might be increased to 250 μm.

- Using the camera in de-magnified mode (1:2.3) showed that larger sections of the pinch may be imaged to determine the overall structure and z-axis variation of the pinch.

- The choice of appropriate filters enabled the camera to image the K-shell and the K+L shell images from an Argon pinch. The camera may also be used to image all the UV emissions from the pinch without a filter. This is possible because the diamond detectors used in the camera are insensitive to visible light and are robust, thus not easily damaged by debris. Images of the UV emission will shed light on the early phases of the radial implosion.

- Two or more pixels can be delayed with respect to each other and multiplexed into the same digitizer channel, without loss of signal fidelity. Such an arrangement reduces the number of digitizer channels needed to use this camera and makes it easier to use.

The 6x12 pixel format of the camera lends itself well to imaging z-pinches, since the axial extent is typically much larger than the radial extent. The use of a double slit arrangement will enable the selective choice of magnification for the radial and axial directions. For example, the radial direction might be imaged with 1:1 magnification to provide a 6-mm field of view with 1-mm resolution. The axial magnification may, however, be configured as a 1:3 de-magnification to provide a 36-mm field of view with 3-mm spatial resolution.

Yet another possibility suggests itself. In this case, the radial magnification is as before 1:1. However, the axial de-magnification is increased to 1:5 to image the 30-mm axial extent of a pinch on to only 6 rows of pixels. This allows the two halves of the camera to be configured to acquire, simultaneously, images of K-shell and K+L shell radiation from a single shot. Digital subtraction of such images will provide spatially and temporally resolved L shell emissions that will prove to be useful in analyzing the early phases of the z-pinch dynamics.

The addition of 24 pixels to upgrade the camera from a 6x12 to a 6x16 array will further enhance the utility of a camera that has already proven that it may be a useful tool for the z-pinch load designer. This addition will allow for increased field of view at high spatial resolution or increased resolution when imaging the entire pinch. While the addition of 24 pixels may appear to increase the digitizer channel requirement to prohibitive levels, this is not true. Experiments at Double-EAGLE have shown that 2 pixels can be successfully delayed and multiplexed into a single digitizer channel. This multiplexing can be increased to accommodate 4 pixels into one digitizer channel. In this case, the upgraded, 96-pixel camera will require only 24 digitizer channels. This number is available at most Nuclear Weapons Effects Simulator facilities.

The rest of this report is organized as follows: Section 2 describes the design and principle of operation of the camera. Section 3 presents data from early experiments showing the lack of crosstalk between pixels. The 75-channel bias box is described in section 4. Data from calibration tests at Sandia National Laboratory are presented in Section 5. The Double-EAGLE validation tests are discussed in Section 6. The report concludes in Section 7 with conclusions, a new calibration at Sandia National Laboratory and a plan for future experiments.

Section 2

Camera Design and Principle of Operation

The diamond camera is designed to provide time-resolved x-ray and ultra-violet images of z-pinches. This section describes the design and the principle of operation of the camera. It begins with the design of the camera. Details of the assembly of each element are then provided, showing how the design was realized. This section concludes with a discussion of the principle of operation of the camera.

2.1 Design of the Camera.

Figure 2-1 shows a photograph of the diamond camera. Figure 2-2 shows the camera with the housing removed, to reveal the details of the detector array and the assembly of the camera.

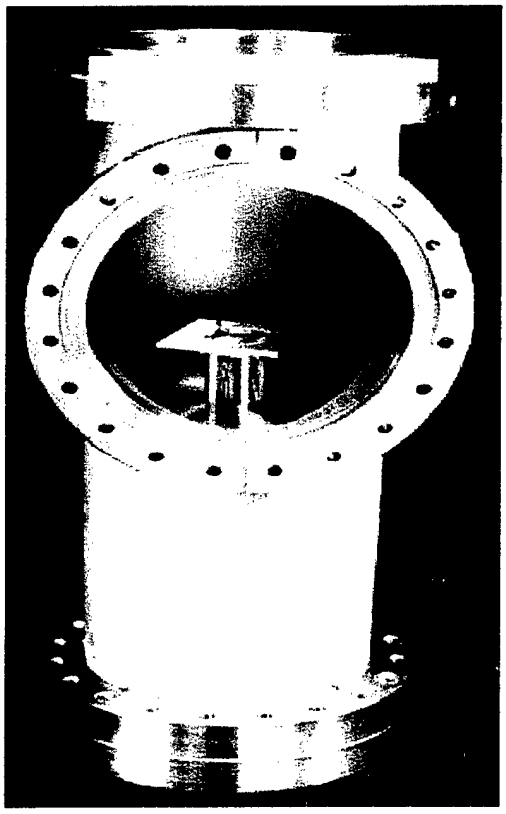

Figure 2-1. Photograph of diamond camera.

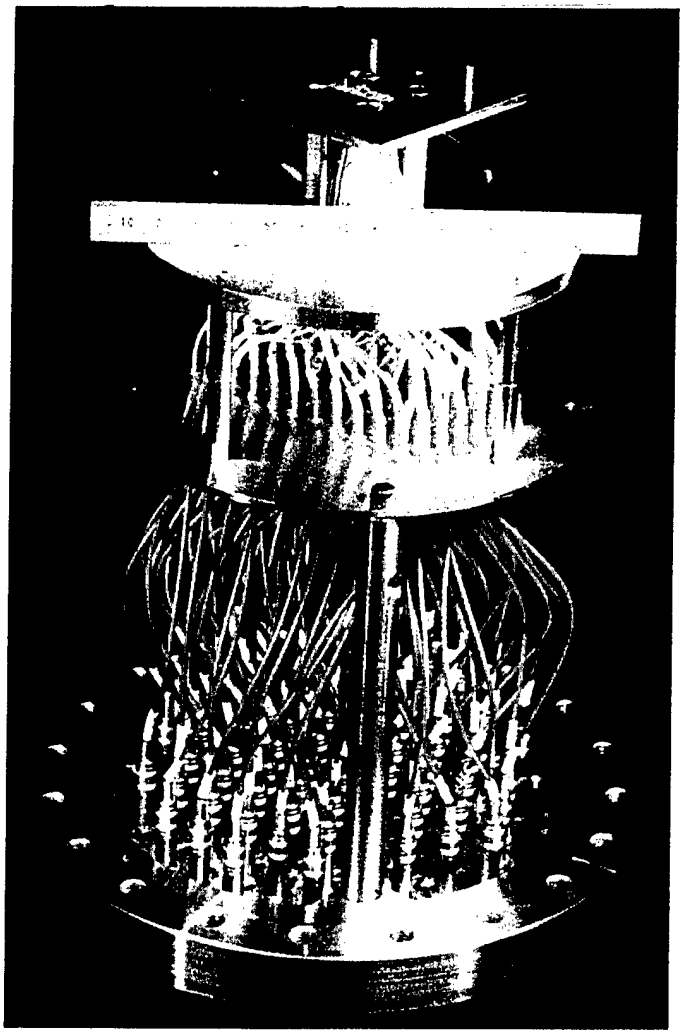

Figure 2-2. Photograph of diamond camera with housing removed.

Figure 2-3 shows a schematic drawing of the camera shown in Figure 2-2. The camera is divided into three modules: Module 1 is the diamond module, Module 2 is the vacuum interface module and Module 3 is the facility coaxial cable interface module. The diamond detectors are mounted on parallel plate strip-lines that straddle G-10 supports. These parallel plate lines transition to 50-Ω coaxial cable near the G-10 supports. These cables terminate at the other end in Suhner MMCX series connectors. RG-178 cable with Suhner MMCX series connectors at one end and Lemo connectors at the other connect the diamond detectors to the vacuum feed-through flange. Outside the vacuum, RG-174 cable is used to connect to the BNC connectors at the outside of the camera. These connectors are used to connect the detectors to the digitizers using coaxial cables at the simulator facility.

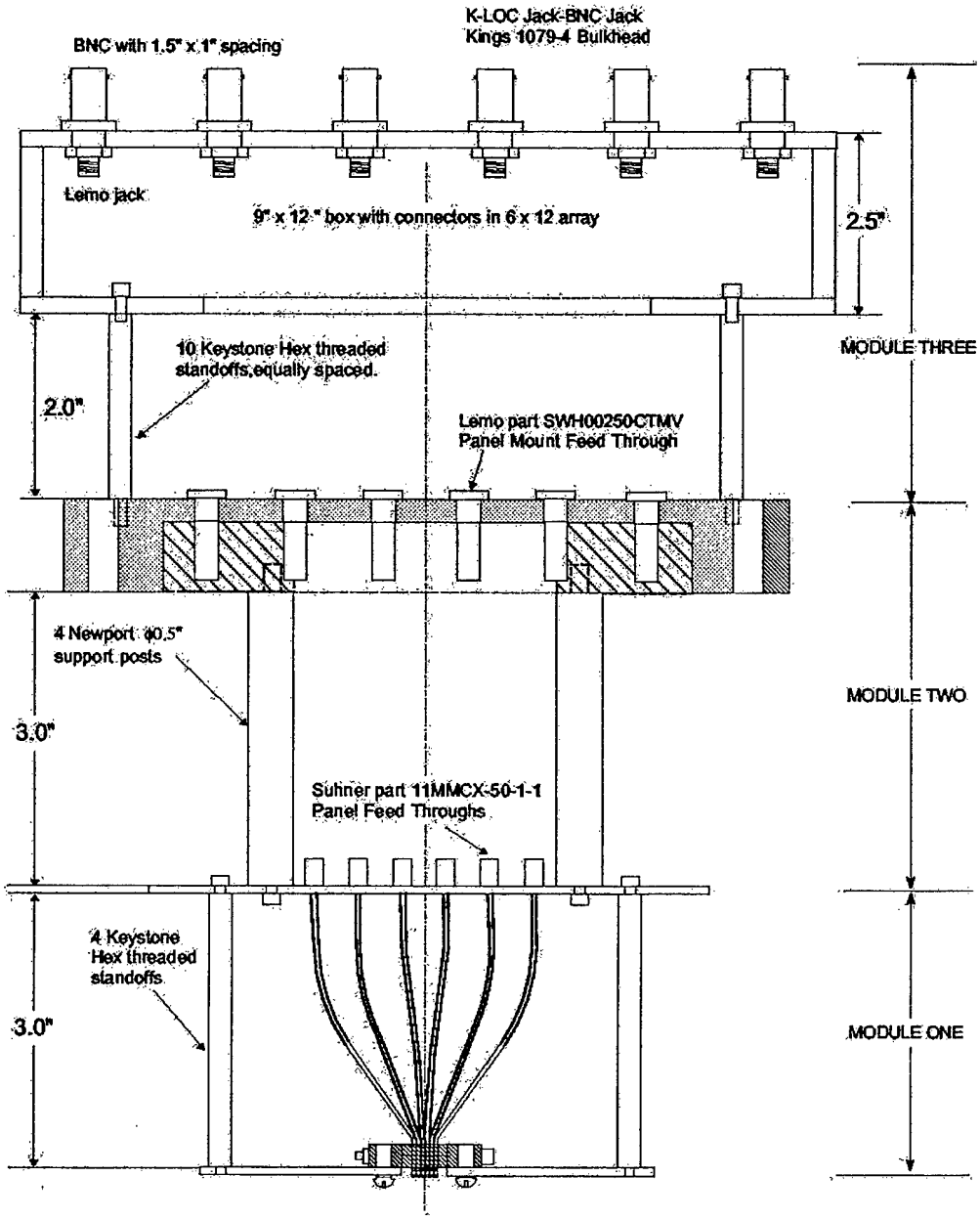

Figure 2-3. Schematic drawing of the camera.

Figures 2-4, 2-5 and 2-6 show the machine drawings for the three flanges shown in the assembly drawing (Figure 2-3). Figure 2-4 shows the detail of the vacuum feed-through flange. Seventy-two holes are drilled in this flange for the Lemo vacuum feed-throughs. In addition, provision is made to accommodate the posts that support the plate with the MMCX connectors and the plate that has the BNC connectors. The 72 connectors are not located in a 6x12 array because doing so would have increased the diameter of the flange to an unacceptable level, increasing the overall weight of the camera. Figure 2-5 shows the details of the plate for the Suhner series MMCX connectors. This plate has holes to mount the supports for the diamond array holder. The diamond array holder is shown in Figure 2-6. The diamond detectors are located within the central rectangular cut out. An intermediary plate is located between the plates shown in Figures 5 and 6. This plate, shown in Figure 2-7, significantly eased the assembly process by not only funneling the pixels towards a more concise area, but also forcing the coaxial cables into their desired ultimate vertical positions. Each individual pixel, once fed through the intermediary plate, can be lengthened or shortened to the desired height by the use of adjustable heat shrink tubing, which has an overall diameter too wide to pass through the machined holes.

The outer housing has been designed to allow for a flange that will assist in the alignment of the camera. It will also permit observation of the diamond detectors and any filters located directly in front of these detectors, both before and immediately after the shot, while the instrument is still under vacuum. A schematic drawing of this housing is shown in Figure 2-8. The housing consists of a "tee" with three 8" conflat flanges. The array, mounted as shown in Figure 2-3, is attached to the fixed flange shown in Figure 2-8. This assembly was shown in the photograph in Figure 2-1. The rotatable flange is attached to one of the machine beam lines. The flange at 90° to the axis of the tube is a tapped flange located as close to the tube as possible. A viewport on this flange will allow viewing of the diamond array while the camera is under vacuum, permitting alignment and observation of the integrity of any soft x-ray filter located near the diamond array.

This design allows for alignment of the camera using a bright light source at the pinch location. Additionally, filters can be mounted on the diamond array to use the array in the differentially filtered mode. In this configuration, different filters are used on different detectors to filter different parts of the spectrum. This allows for the accurate determination of the x-ray output as demonstrated by AASC during the Ar-Kr implosions on Phoenix (Krishnan 1996).

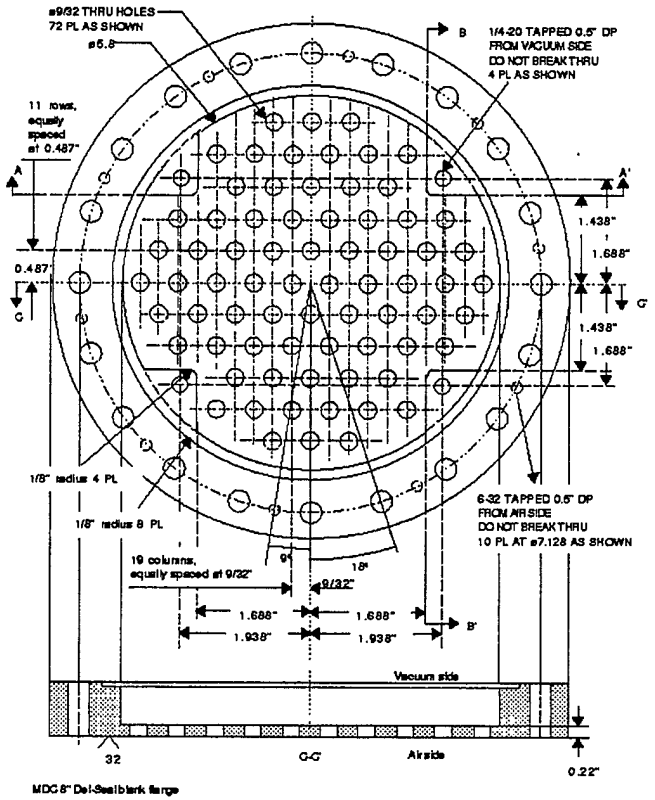

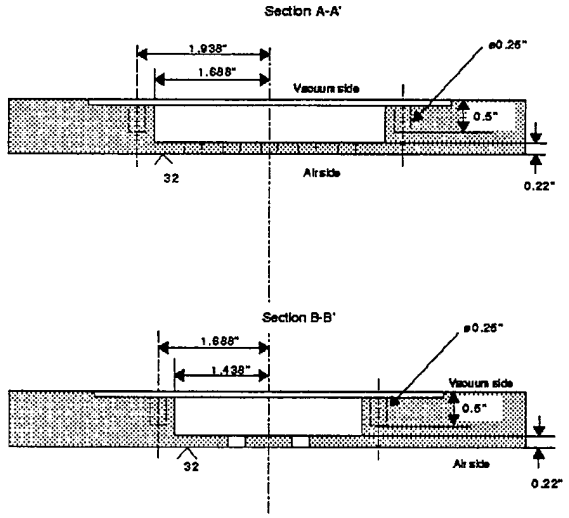

ALAMEDA APPLIED SCIENCES CORPORATION 2235 Polvorosa Avenue, Suite 230, San Leandro, CA 94577 Tel: 510-483-4156 Fax: 510-483-8107	
Drawn by: Ivon Tzonev Date: 10/30/97 Checked by: Date:	Title: Diamond Radiation Imaging Camera Vacuum Feed through flange
Tolerances, unless otherwise specified: x.x ± 0.05" x.xx ± 0.02" x.xxx ±0.005	Material: MDC 8" Del-Seal Blank flange AASC WILL SUPPLY FLANGE
Drawing No. AASC97D0083	Rev. A
Note: 1 piece required	

Figure 2-4. Engineering drawing of the vacuum feed-through flange.

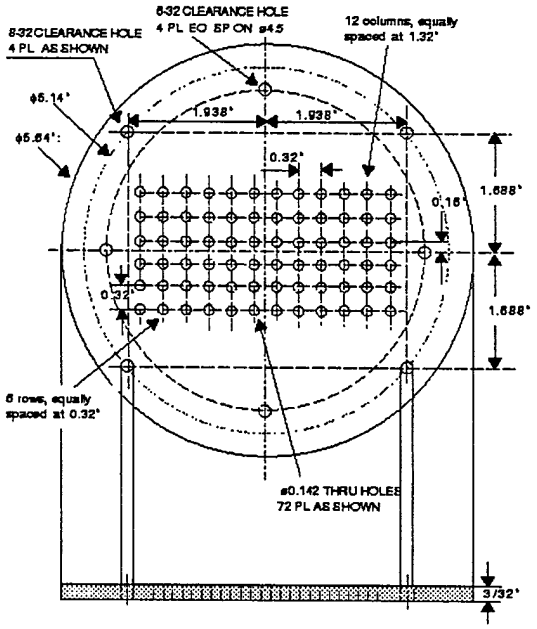

ALAMEDA APPLIED SCIENCES CORPORATION 2235 Polvorosa Avenue, Suite 230, San Leandro, CA 94577 Tel: 510-483-4156 Fax: 510-483-8107	
Drawn by: Ivon Tzonev Date: 10/30/97 Checked by: Date:	Title: Diamond Radiation Imaging Camera: Plate for Suhner miniature connectors
Tolerances, unless otherwise specified: x.x ± 0.05" x.xx ± 0.02" x.xxx ±0.005	Material: 303 SS
Drawing No. AASC97D0084	Rev. A
Note: 1 piece	

Figure 2-5. Engineering drawing of the plate that houses the Suhner MMCX connectors.

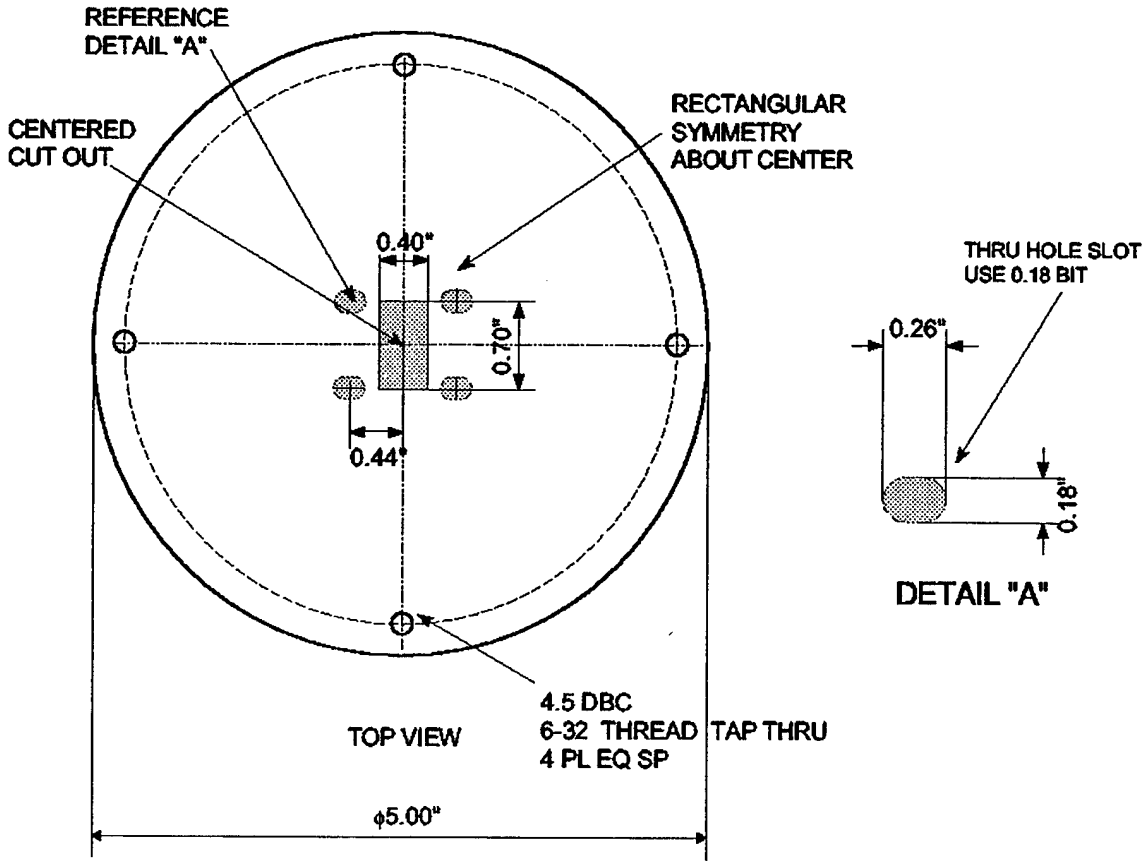

Drawn by: Ivon Tzonev	Date: 10/28/97	ALAMEDA APPLIED SCIENCES CORP. 2235 POLVOROSA AVE., SUITE 230 SAN LEANDRO, CA 94577 Tel: 510-483-4156 Fax 510-483-8107
Checked by	Date	
Dimensions in inches Tolerances, unless otherwise specified x.x ±0.05 x.xx ±0.02 x.xxx ±0.005		Title: Diamond Array Holder
Material: 303 SS PLATE 3/16 THICK		Drawing No.: AASC97D0085 — Rev.: A

Figure 2-6. Engineering drawing of the diamond array holder plate.

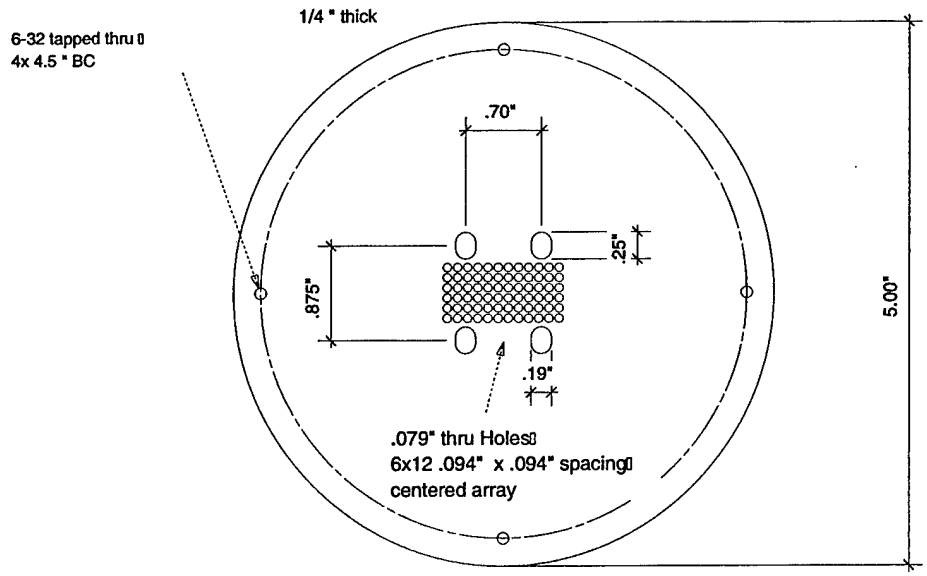

ALAMEDA APPLIED SCIENCES CORP. 2235 POLVOROSA AVE. SUITE 230 SAN LEANDRO, CA 94577 Tel: (510) 483-4156 Fax: (510) 483-8107		Title Diamond Camera Cable Guide	
Drawn by John Edighoffer	Date 5/19/98	Checked by	Date
		Tolerances (unless otherwise specified) X.X ±0.1 X.XX ±0.02 X.XXX ±0.002 Dimensions in inches	Materials 304 Stainless Steel Scale 1:1 Drawing Number AASC98D0012

Figure 2-7. Schematic drawing of the "Intermediary Plate" situated within Module 1.

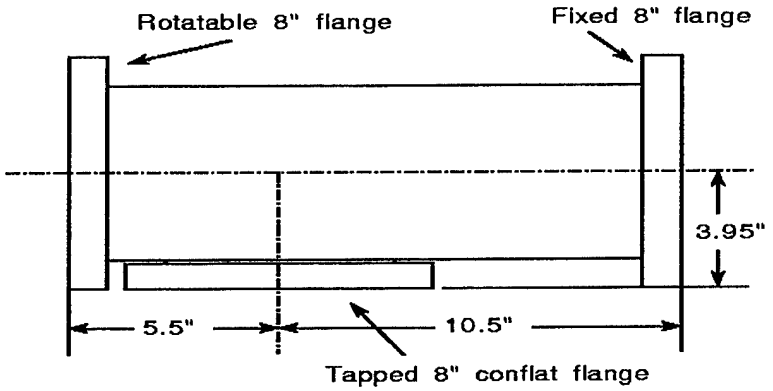

Figure 2-8. Schematic drawing of the housing of the diamond camera.

2.2 Assembly of the Diamond Camera.

The vacuum feed-through flange, shown in Figure 2-4, was the first sub-assembly completed and vacuum leak checked. The base pressure achieved was better than $5x10^{-7}$ Torr, limited by the test chamber. Figure 2-9 is a photograph of the assembled flange.

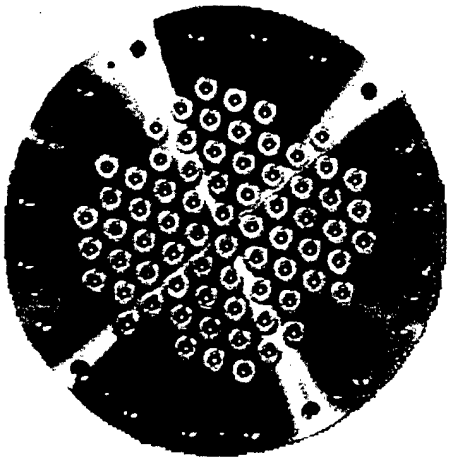

Figure 2-9. Vacuum feed-through flange.

The next sub-assembly was the diamond-shim assembly. This assembly consists of two 1 mm x 2 mil stainless steel shims, which are 10 mm and 14 mm long and a 1 mm x 1 mm x 0.5 mm thick diamond soldered between them. The shims are tinned with solder to ensure proper soldering to the diamond and to the 50-Ω coaxial cables with Suhner connectors. The size of the tinning on each shim is shown in Figure 2-10. Figure 2-11 shows a detail of a diamond-shim assembly.

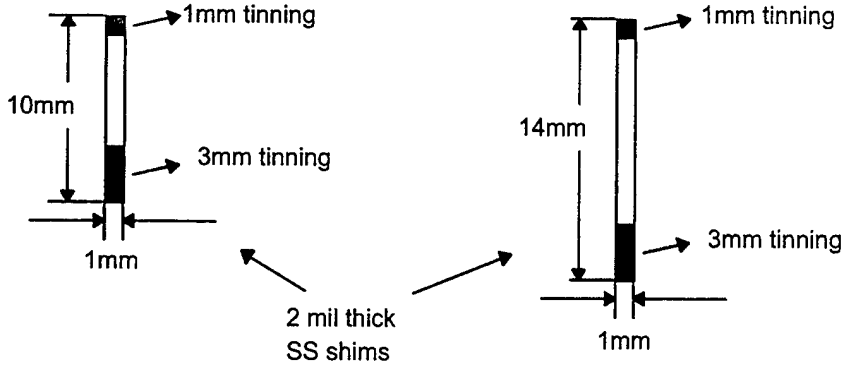

Figure 2-10. Schematic drawing of a pair of stainless steel shims.

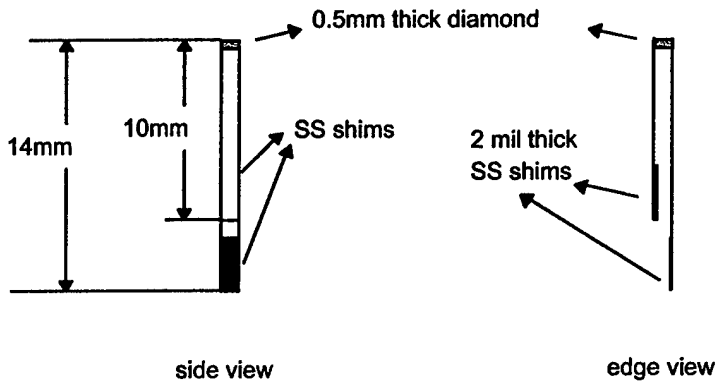

Figure 2-11. Schematic drawing of a diamond-shim assembly: it is essentially a pair of stainless steel shims soldered to a diamond pixel.

After the diamond pixel is soldered to the pair of shims, the 50-Ω coaxial cables are trimmed and soldered to the shims. The cables are 0.047" in diameter and 9.5 mm long. Each cable is attached to a Suhner jack connector (purchased from Microstock). The cables are trimmed as shown in Figure 2-12.

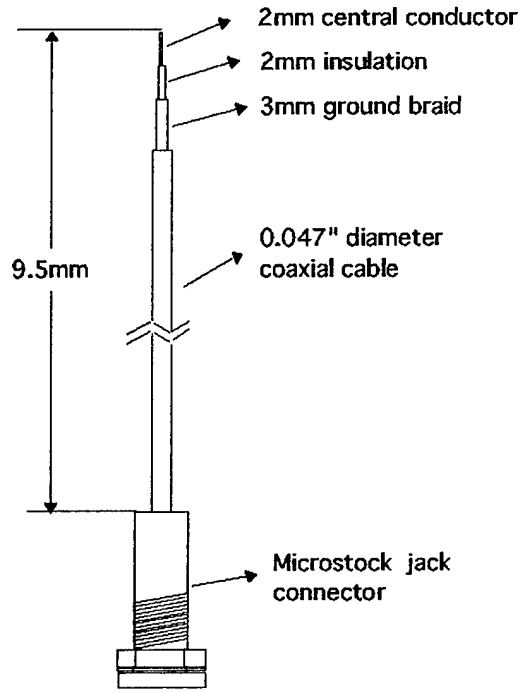

Figure 2-12. Suhner connector and cable (from Microstock) used in the diamond detector assembly.

The central conductor of the cable is soldered to the 10-mm long SS shim. The ground braid is soldered to the 14-mm long SS shim as shown in the drawing of the complete diamond detector assembly in Figure 2-13. Figure 2-14 shows a photograph of the assembled diamond detectors.

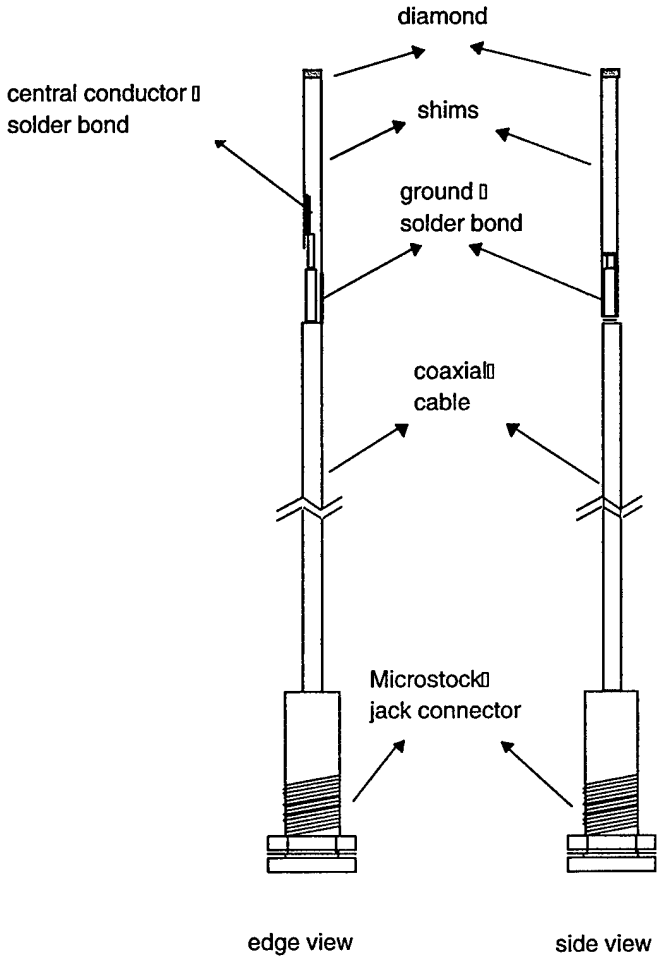

Figure 2-13. Schematic drawing of a diamond detector assembly.

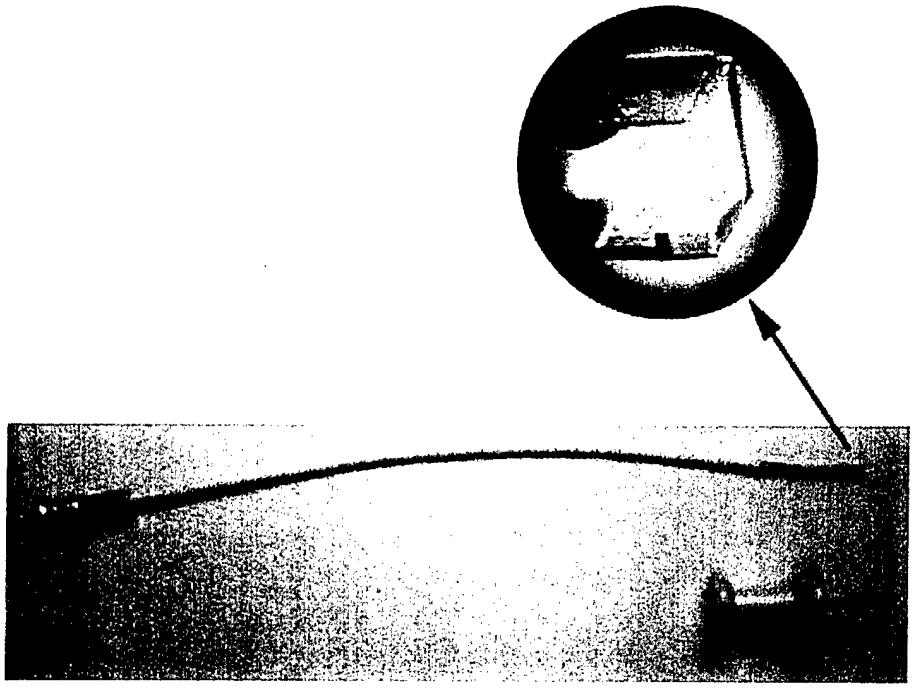

Figure 2-14. Photograph of a diamond detector assembly.

Upon the completion of the diamond detector assembly shown in Figure 2-14, the assembly was shipped to Paratech Inc. This company coated a thin layer of parylene on the diamond, shim and bare coax cable. This 0.0005" thick layer of parylene provides insulation between neighboring pixels in the completed assembly. Paratech took great care not to coat the front surface of the diamond with parylene. Further, the diamond faces were thoroughly cleaned prior to final assembly to ensure no spurious UV filtering due to coatings on the pixel faces.

Upon completion of the coating process each pixel was mounted on the Suhner connector plate (Figure 2-5) and the intermediary plate (Figure 2-7). Figure 2-15 shows a side view of the assembly, illustrating the function of the intermediary plate.

The top view of diamond camera is shown in Figure 2-16. The thin coating of Parylene on the stainless steel shims proved to be successful. The pixels when tested with 200 V yielded a minimal leakage current among neighboring pixels, never exceeding 5 nA.

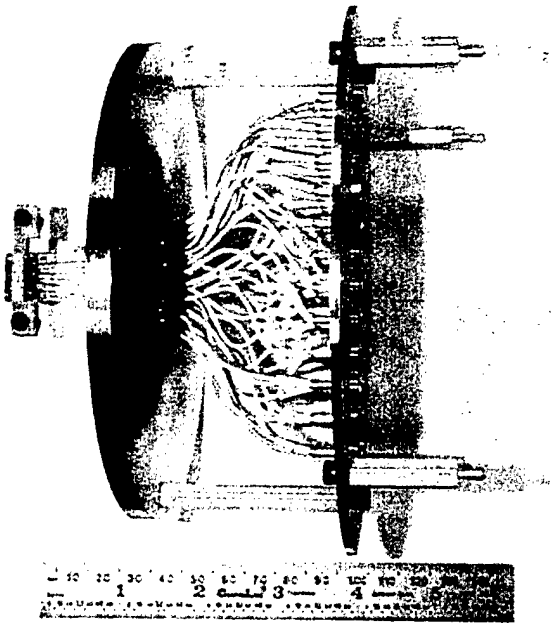

Figure 2-15. Side view picture revealing the organizing property of the "Intermediary Plate".

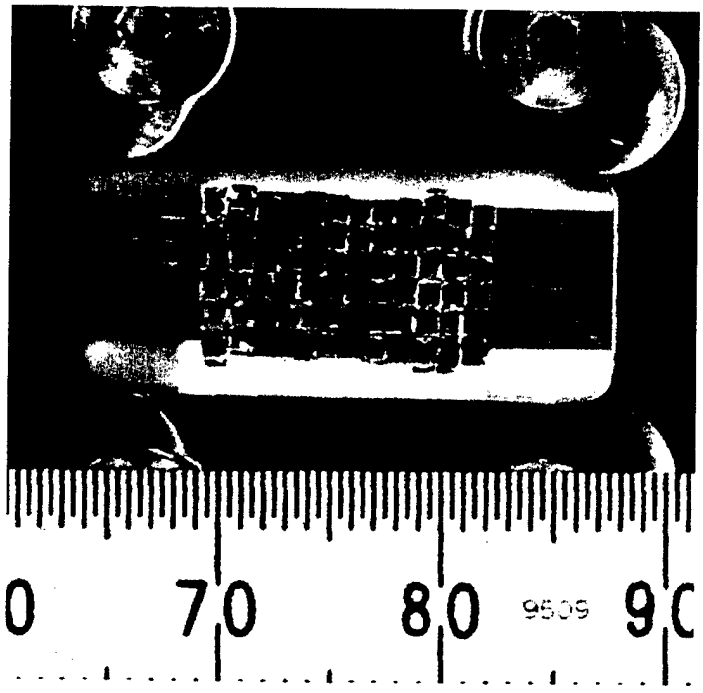

Figure 2-16. Top view of the diamond array. The scale shows dimensions in mm.

2.3 Principle of Operation.

The use of diamond in photoconductivity experiments began in 1923 (Gudden 1923). Since then advances in the technology used to metallize the diamond at the edges to enable electrical contacts has promoted the use of diamond as a photoconducting detector of radiation (Kania 1993), (Pan, Han, Kania 1993), (Pan, Kania 1993), (Spielman 1992). Extremely rapid turn-on and turn-off times (<100 ps) have been demonstrated with the use of fast x-ray excitation of the diamond detectors (Pan, Han, Kania, Plano, et al 1993), (Spielman 1992). Recent advances in chemical vapor deposition (CVD) technology have enabled the production of diamond films of the quality (at least in terms of the electrical and thermal properties) of natural diamond (Pan, Han, Kania, Plano, et al 1993). Diamond has a large band gap, radiation hardness, large saturated carrier velocity and low atomic number. This makes diamond a very attractive candidate as a radiation detector. The most common diamond radiation detectors (DRDs) are in the form of two terminal electronic devices with a metal-insulator-metal (MIM) structure (Kania 1993). This is the type of detector used in the diamond camera, which in essence consists of 72 individual diamond detectors. The insulator (diamond) is undoped and the metal caps form Ohmic contacts requiring no p-type or n-type junctions as is common with silicon based radiation detectors. Silicon cannot be operated with this structure because thermally generated leakage currents are high. These leakage currents in silicon are suppressed by the use of reverse biased junctions.

Diamond can detect any radiation (UV, x-rays, gamma rays, charged particles, neutrons, pions and other high-energy particles) that generates free carriers (electron-hole pairs) in the diamond. The fundamental mechanism of radiation detection in diamond is independent of the exciting radiation as long as it is more energetic than the band gap in diamond (5.5 eV). Figure 2-17 shows a schematic of a MIM diamond detector. A high resistivity diamond is sandwiched between two metal electrodes connected to an external voltage to provide an electric field across the device. Mobile charges produced as a result of absorbed radiation drift in this electric field and generate a current in the external circuit. The basic physics of the device is well explained in Ref. (Pan, Han, Kania, 1993). It is the fact the production of mobile charges in the diamond effectively reduces the resistance of the diamond that distinguishes it from silicon based detectors such as PIN diodes.

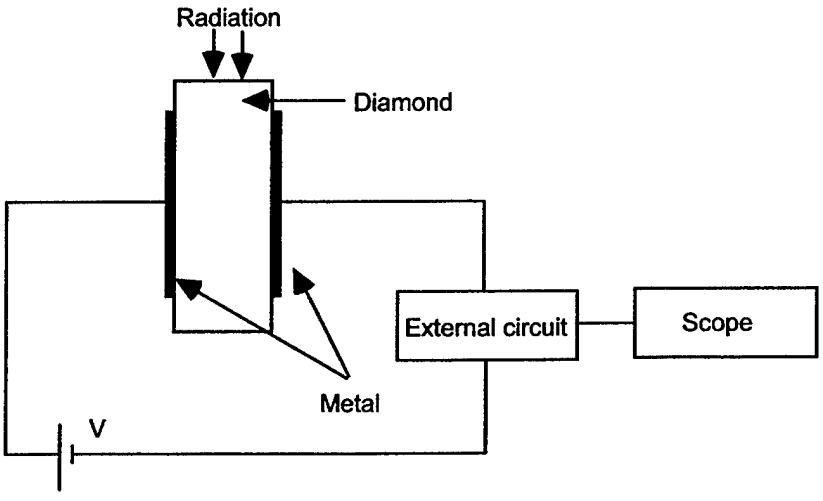

Figure 2-17. Schematic drawing showing a diamond metal-insulator-metal detector.

Because the sensitivity of the DRD depends linearly on the voltage applied across the device (for a given diamond thickness), DRDs exhibit a very desirable signal amplitude compression as the output signal approaches the DRD bias voltage. A simple algebraic correction can retrieve the effective signal that may be larger than the applied bias:

$$V_c = V_m / (1 - V_m / V_b) \qquad (2\text{-}1)$$

where V_b is the applied bias voltage, V_m is the measured signal, and V_c is the corrected signal (Spielman 1988). Thus, even in cases where a signal may unexpectedly approach saturation, useful and accurate information may still be obtained.

An image of the pinch is formed on the diamond detector array using a pinhole located between the source to be imaged and the camera. Each detector in the array thus "sees" a portion of the pinch. The signal read at the digitizer is therefore proportional to the intensity of the radiation on that particular pixel. Images of the pinch are then reconstructed using a two step procedure. First, the signal measured on each detector (pixel) is converted into the intensity emitted from the spatially resolved regions of the source using the calibration factor for each pixel. These calibration factors were determined at the laser produced plasma calibration source at Sandia National Laboratory. Then the images are reconstructed by creating 6x12 pixel arrays at each time during the digitized record. A computer program was written to accomplish this task. Thus, discrete images of the pinch, acquired at the digitizing rate of the digitizers are obtained. Details of the calibration and validation on Double-EAGLE follow in subsequent sections.

The use of filters allows the imaging of the x-ray or UV emissions from the pinch. The spatial resolution is determined by the magnification used (depends on the location of pinhole relative to the source and detector array). Since the diamond elements are 1 mm x 1 mm in area, a 2:1 magnification will lead to a 500 μm x 500 μm spatial resolution.

Section 3

Early Experiments

Prior to the assembly of the 6x12 pixel array camera, a 3x3 pixel prototype was constructed. The purpose of this prototype was to demonstrate the validity of the principle of operation of the camera and to address the issue of crosstalk between neighboring pixels. This section discusses these early experiments with the prototype camera.

3.1 Design of the 3x3 Prototype Camera.

The design of the prototype 3x3 camera is based on the 72-pixel camera design. A drawing of the prototype is shown in Figure 3-1. Nine diamond detector assemblies are mounted in three rows of three each on 1 mm wide Macor supports. The diamond assembly parallel plate transmission lines are connected to 0.050" diameter 50 Ω coax cables that terminate in C-Series plugs from Microtech. The 3x3 array uses Microtech C-series CP-40-1 plugs and CR-40-4F jack-jack panel feedthrough connectors to make the transition between the coax cable, connected to the stainless steel shims and the cable with Lemo connectors. The cables transition out of vacuum through Lemo feedthroughs connected to a 6" conflat flange.

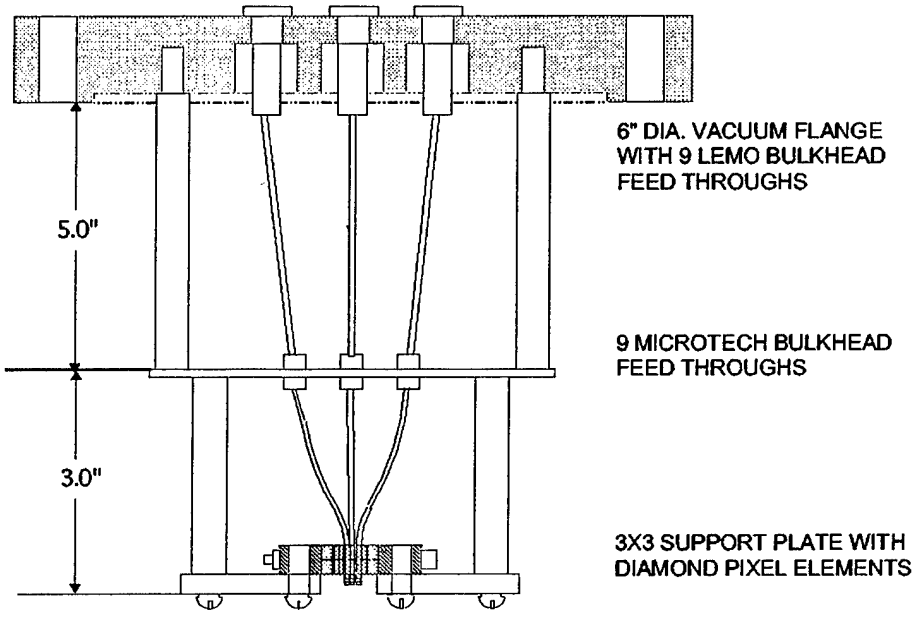

Figure 3-1. Drawing of the 3x3 prototype diamond camera.

Each diamond detector assembly in the 9 element array consists of the diamond detector and a pair of 0.002" thick, ~0.5" long stainless steel ribbons that connect two opposing diamond electrode edges to 0.05" diameter, 50 Ω coaxial cable. The stainless steel ribbons are coated with 0.0005" of Parylene to provide electrical insulation between elements. Ten diamond assemblies were built and coated with Parylene for the prototype camera. Figure 3-2 shows a few different views of the assemblies.

Figure 3-2. Photographs of the diamond assemblies.

Drawings of the 6" diameter vacuum flange, the bulkhead plate for the Microtech connectors and the detector support plate are shown in Figures 3-3, 3-4, and 3-5.

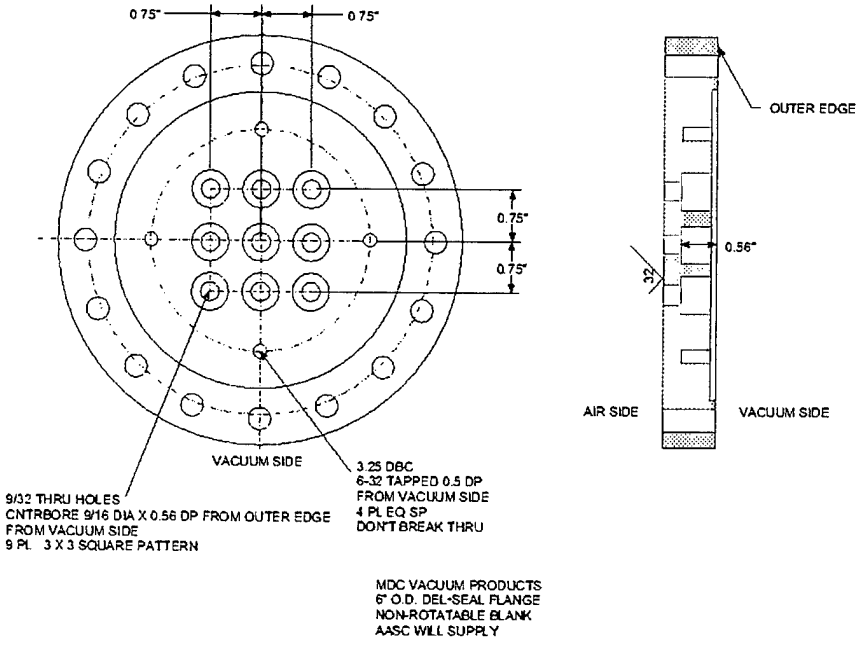

Figure 3-3. Vacuum flange with 9 Lemo jack-jack connectors.

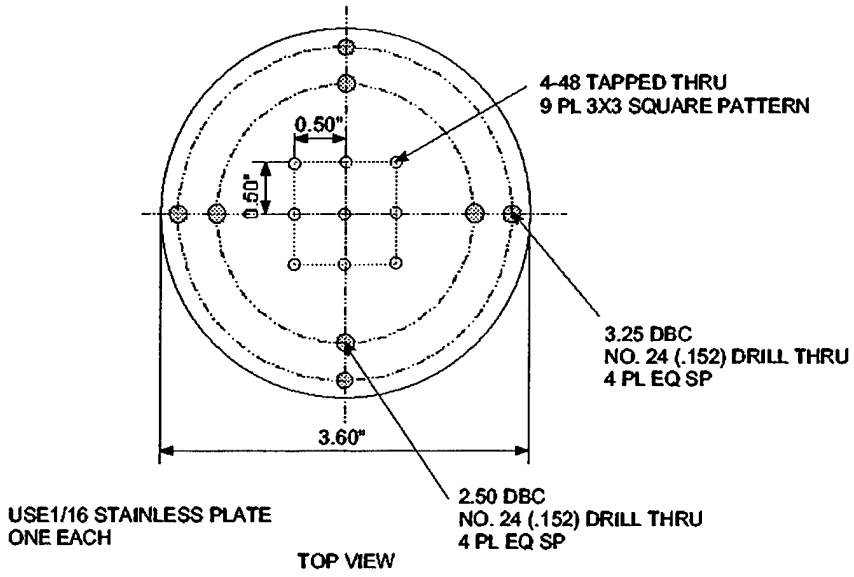

Figure 3-4. Bulkhead plate for the Microtech connectors.

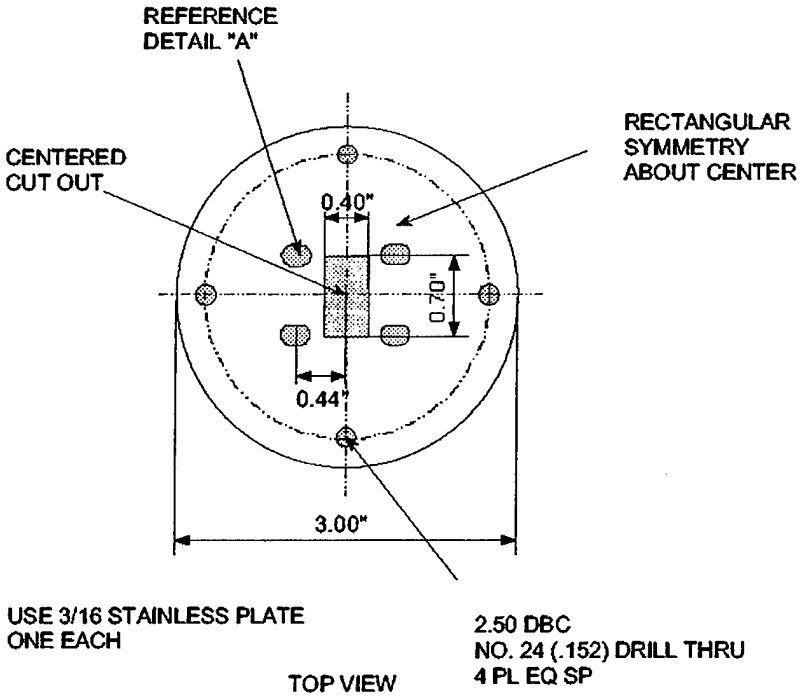

Figure 3-5. The diamond detector support plate.

3.2 Fabrication of the 3x3 Prototype Camera.

The 3x3 array camera was successfully fabricated and tested. Two photographs of this camera are shown in Figure 3-6. Experience gained from the assembly of this 3x3 array has been useful in guiding modifications to the design and assembly procedures of the 72-pixel camera. The details of this assembly are in Ref. (Prasad 1997).

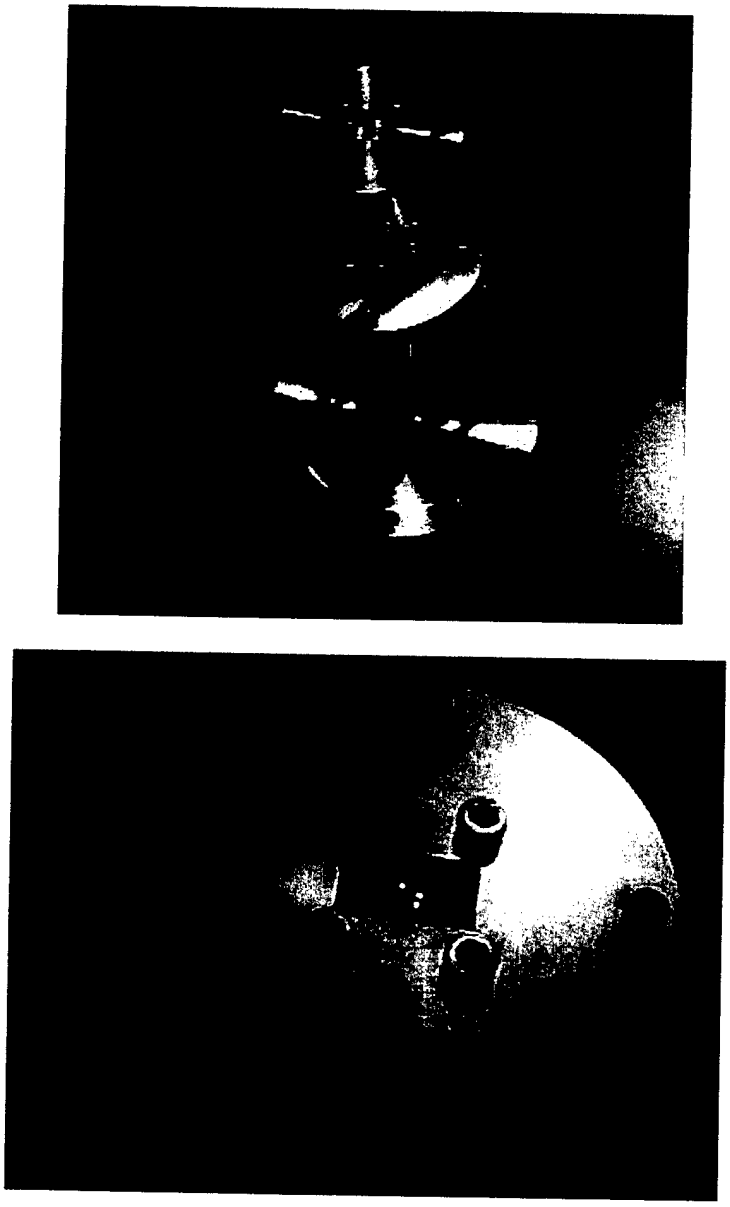

Figure 3-6. Photographs of the 3x3 prototype diamond camera. Entire assembly (top) and detail of the detector array (bottom).

3.3 Crosstalk.

This section describes the issue of crosstalk between adjacent pixels and describes an experiment to show that crosstalk does not pose a problem. We begin with a calculation that estimates the magnitude of the problem. Then we present an experiment that shows that the calculation is reasonably accurate.

3.3.1 Crosstalk Calculation.

A possible problem with the diamond camera is that crosstalk between the individual pixels could couple signals from one detector to another making measurements unreliable. The first ~1 cm of the signal path from the diamond detector pixels is carried on unshielded parallel lines and these are packed very tightly. This section is vulnerable to crosstalk. To address this issue crosstalk calculations were performed to determine the expected crosstalk between a pair of diamond assembly elements. This was done for two assembly orientations: face-to-face and edge-to-edge. A pair of transmission-line test assemblies, similar to the diamond assemblies, was then tested using a signal generator to experimentally measure the crosstalk amplitudes.

3.3.1.1 Detector Bias Circuit.

The diamond radiation detectors (DRDs) that make up the 72 pixels of the camera are typically biased to 100 V. A typical bias circuit for a single DRD is shown in Figure 3-7. V_{bias} is the bias voltage applied to the diamond pixel. V_{out} is the measured signal voltage. $R_{diamond}$ represents the diamond resistance.

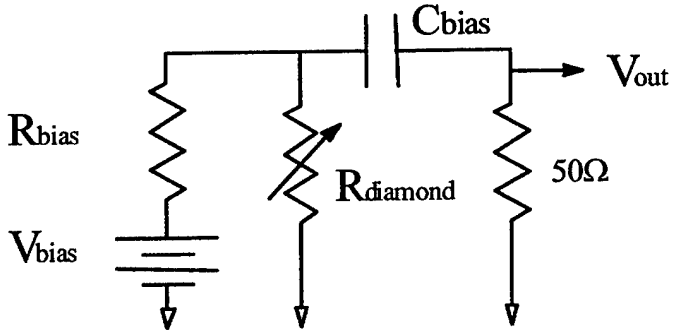

Figure 3-7. The Bias Circuit for a Diamond Radiation Detector.

3.3.2 Circuits for Modeling Crosstalk.

The following circuits, illustrated in Figures 3-8 and 3-9, are used to model the coupling between a pair of the camera pixel elements. Two orientations for the pair are considered and are shown in Figure 3-10.

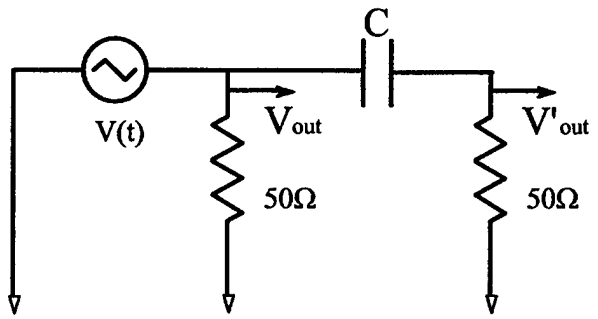

Figure 3-8. Circuit for the Capacitive Coupling Calculation.

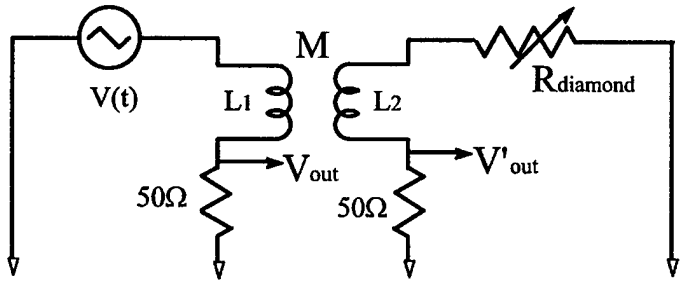

Figure 3-9. Circuit for the Inductive Coupling Calculation.

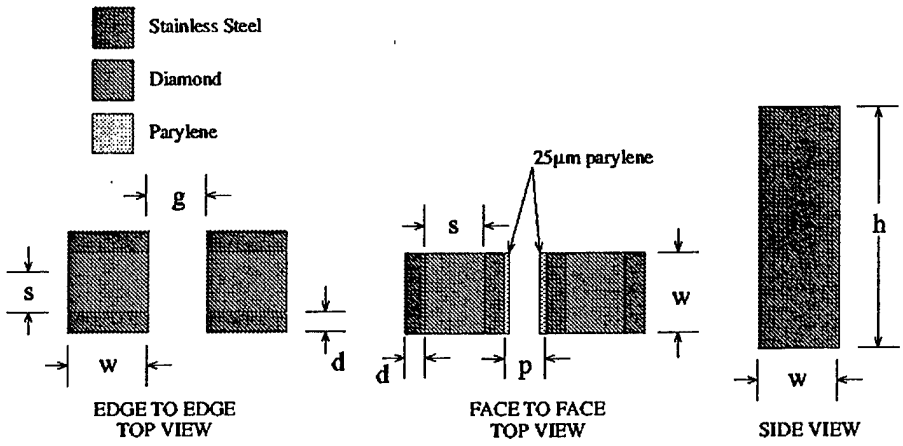

Figure 3-10. Pixel orientations: EDGE TO EDGE and FACE TO FACE and a side view of the assembly showing the height of the coupling region.

The geometric dimensions of the assemblies are:

s = space between one pixel's electrodes = 1000 mm

g = edge to edge gap = 200 mm

w = width of detector = 1000 mm

d = depth of shim stock = 50 mm

h = height of shim stock = 7000 mm.

3.3.3. Estimate of Capacitance and Inductance Between a Pair of Assemblies.

The capacitance between two diamond assemblies is estimated to be:

$$C = \varepsilon\frac{A}{d} \cong (2-3)\varepsilon_0\frac{Area}{\text{distance}} \qquad \varepsilon_0 = 8.85\times10^{-12}\,F/m \tag{3-1}$$

The inductance is estimated to be:

$M = K\sqrt{L_1 L_2} = KL$, K is the fraction of flux coupled from one inductor to the other.

$L \approx \mu_0 n^2 lA = \mu_0\frac{N^2 A}{l}$, where n is the turns/length, A = area, $n = N/l$, and N = the number of turns. $\mu_0 = 4\pi\times10^{-7}\,H/m$ (3-2)

Edge to Edge:

$$C_e \approx \varepsilon_0 \frac{dh}{g} \approx 15fF$$

$$M_e \approx K_e L \approx K_e \mu_0 \frac{N^2 A}{l} \approx K_e \mu_0 \frac{N^2 sh}{w}, \qquad K_e \approx 1 \text{ (worst case).} \qquad (3\text{-}3)$$

$M_e \approx 8.8$ nH.

Face to Face:

$$C_f \approx \varepsilon \frac{wh}{p}, \qquad C_f \approx 6.2pF, \qquad \varepsilon \approx 2.5\varepsilon_0 \qquad (3\text{-}4)$$

$M_f = K_f L = K_f M_e$ $\qquad K_f \approx 0.1$ (estimate)

$M_f \approx 880pH$

3.3.4 Calculated Crosstalk from Capacitive and Inductive Coupling.

For the following discussion, we will assume the signal on the primary detector has a 4 ns rise-time and a 10 ns FWHM.

For Capacitive Coupling:

$$VC = Q \Rightarrow \dot{V}C = I \Rightarrow \dot{V}RC = IR = V'_{out} \qquad (3\text{-}5)$$

$\dot{V} \approx \frac{V_{out}}{t_{rise}} \Rightarrow$ The fractional coupling between the primary and secondary elements is approximately:

$\frac{V'_{out}}{V_{out}} \approx \frac{RC}{t_{rise}}$ In addition, the secondary signals will pick up approximately:

Edge to Edge $\approx \frac{50\Omega \cdot 15fF}{4ns} \approx 0.02\%$

Face to Face $\approx \frac{50\Omega \cdot 6.2pF}{4ns} \approx 8\%.$

For Inductive Coupling:

$$L_1 \dot{I} = V_{L_1} \text{ and } \dot{I} = \frac{\dot{V}_{out}}{R} \Rightarrow \frac{L_1 \dot{V}_{out}}{R} = V_{L_1} \qquad (3\text{-}6)$$

by definition: $KV_{L_1} = -V'_{out} \Rightarrow$

$\frac{-KL_1 V_{out}}{R} = V'_{out} \Rightarrow \frac{-KL_1}{R}\frac{V_{out}}{t_{rise}} \approx V'_{out}$ Therefore, the fractional coupling is approximately:

$\frac{V'_{out}}{V_{out}} \approx \frac{-KL_1}{Rt_{rise}} \approx -\frac{M}{Rt_{rise}}$ In addition, we get secondary signals of:.

Edge to Edge $\approx \frac{-8.8nH}{50\Omega \cdot 4ns} \approx -4\%$

Face to Face $\approx \frac{-880pH}{50\Omega \cdot 4ns} \approx -0.4\%.$

Because the space between elements on the assembled camera will be very small, it is quite difficult to predict what the crosstalk between the separate pixels will be. These calculations are mainly used as a design tool.

3.3.5 Experimental Measurement of Crosstalk.

For the crosstalk measurements, a test circuit was built which consists of two transmission line assemblies as shown in Figure 3-11. The assemblies have dimensions similar to the diamond assemblies except the stainless strip lines are ≈3 cm long, whereas the diamond assemblies have ≈1 cm long strip lines. In place of the diamond, a piece of copper was used. Measurements were taken with the test assemblies in both the face-to-face and the edge-to-edge orientations. The pixel elements will have these orientations in the diamond camera.

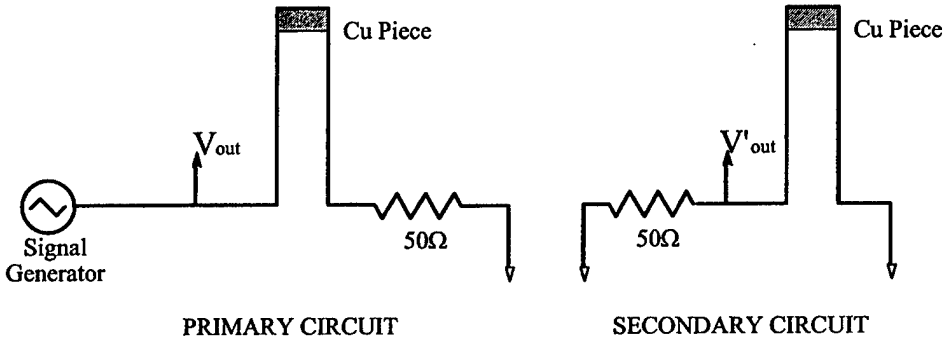

Figure 3-11. Diagrams of the experimental circuit elements.

Figures 3-12 and 3-13 show the results of the crosstalk measurements. The results shown in Figure 3-12 are from the face-to-face configuration. The primary signal measures about 2.5 volts and the crosstalk signal coupled into the secondary has an amplitude of about .07 volts. This corresponds to a 3% coupling. The edge-to-edge measurements in Figure 3-13 show a similar crosstalk coupling.

These bench-top crosstalk measurements were performed to determine whether any adjustments in the diamond assembly design are warranted. The answer is no. Of course, further crosstalk measurements were performed during the testing of the nine-pixel diamond camera on a PRS source and described later in this report.

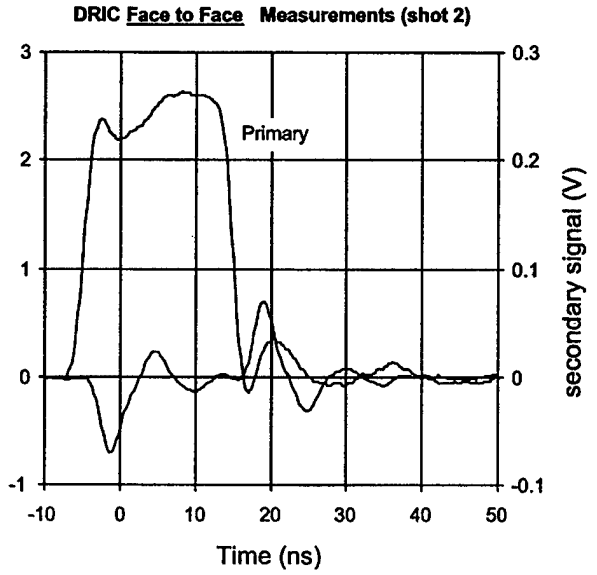

Figure 3-12. Measured crosstalk signals: Face to Face orientation.

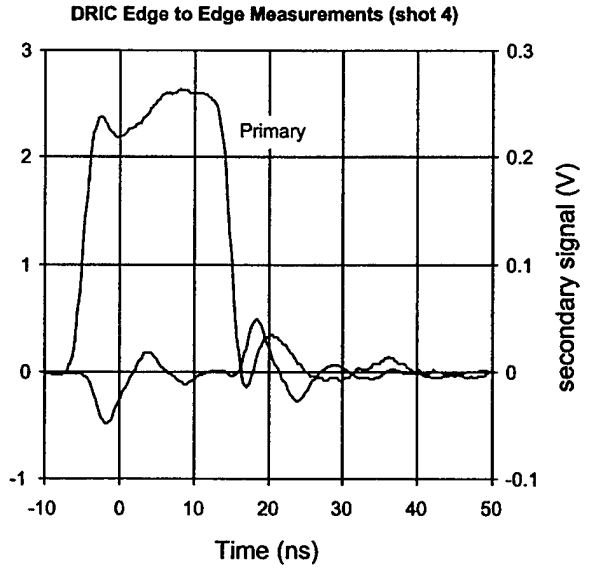

Figure 3-13. Measured crosstalk signals: Edge to Edge orientation.

3.4 Test of the 3x3 array on DM2.

This section presents data from the test of the camera on the Al wire PRS source on DM2. The data acquired on DM2 have a large noise level that tracks the machine current pulse. A digital technique developed to extract data from the signals captured on DM2 is also presented. This technique allows the capture of fast signals on machines such as DM2 without the use of expensive double shielded cables.

The 3x3 array was located on a beam line that was transverse to the pinch axis and about 80° from the horizontal. The diamond elements were 164 cm from the z-pinch axis. The camera was shielded from visible and UV radiation by a barrier of 8.3 μm thick Kapton that was coated with a ≈2000 Å layer of Aluminum. A -90 V battery was used to bias the detectors. No imaging pinhole was used to allow the determination of the relative sensitivity of the detectors. The numbering of the pixels in the 3x3 element array is shown schematically in Figure 3-14. During dc hold-off tests it was determined that two channels - 3 and 5 were shorted to each other. This occurred due to the peeling of the varnish used to insulate the connection between the coax cable and the parallel plate line to the diamond. The new technique developed for the 72-pixel instrument avoids this potential drawback.

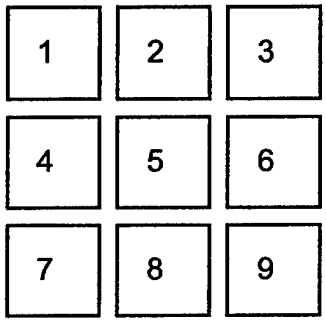

Figure 3-14. Schematic diagram showing the pixel numbering in the 3x3 array.

Figures 3-15 and 3-16 show the raw signals captured when all 9 detectors were biased on DM2 shot #518. The signals on channel 1 and 3 are clipped. There was no signal recorded on channel 6 due a broken connection that we were unable to trace due to limited experimental time. This trace is not shown in Figure 3-16.

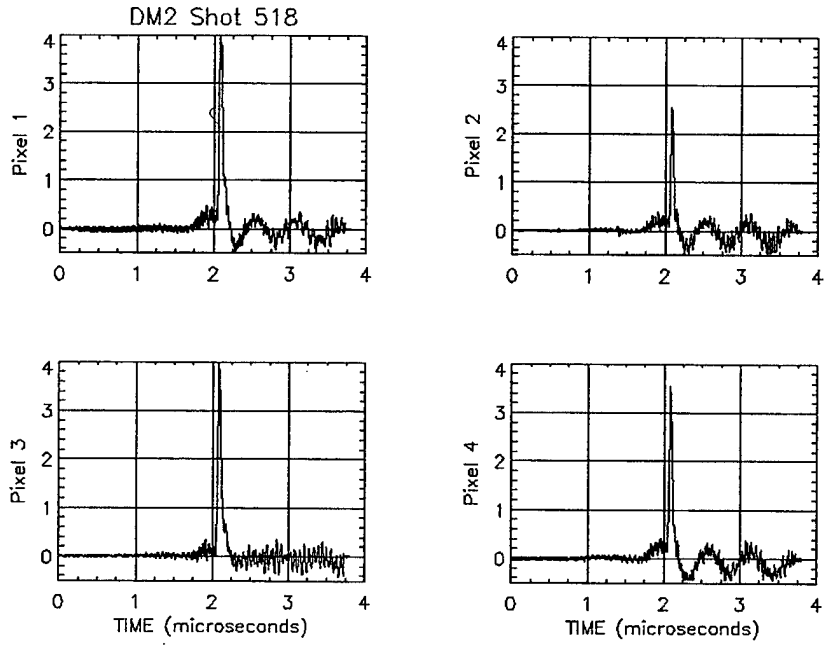

Figure 3-15. Signals recorded on channels 1 through 4 on DM2 shot 518. The signals on channel 1 and 3 were clipped.

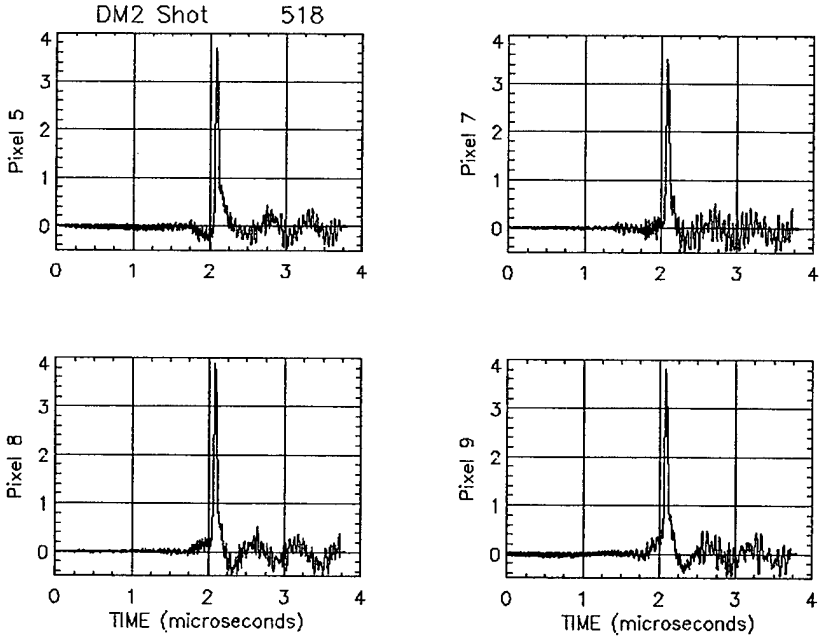

Figure 3-16. Signals recorded on channels 5 through 9 on DM2 shot 518. Channel 6 produced no signal and is not displayed.

Seven of the detectors show signal amplitudes that are within 10% of one another. One is about 40% lower. The x-ray output of shot 518 according to measurements made with calorimeters at MPI was 1.54 kJ. The transmission of the filters used was about 40%. The detectors are 1 mm x 1 mm in area and were located 164 cm away from the source. The full width at half maximum of the x-ray pulses is about 45 ns. Therefore, the sensitivity of pixel 4 is about 1.8×10^{-4} A/W for a 100 V bias. This is typical of diamond radiation detectors.

A noise component on the traces has a ≈0.6 μs period. This signal can be as large as ≈0.5 V. Compared to the ≈4 V x-ray pulse this represents a ≈12% noise floor. Such a noise level is unacceptable, since it would make measuring the crosstalk virtually impossible, given that it is expected to be less than 5% of the peak signal.

However, there is a mitigating factor. The signal of interest - the x-ray signal - has a full width at half maximum of about 45 ns (shown in Figure 3-17) while the noise has a period of about 600 ns. This difference in the frequency of the signal and the noise allows a simple procedure to remove the noise digitally, after the signal has been captured by a digitizer[1]. A simple low pass filter applied to the captured traces determines the magnitude of the noise level, while eliminating the signal (see Figures 3-18 and 3-19). As before the traces for channel 6 are not shown, since the pixel was non-functional.

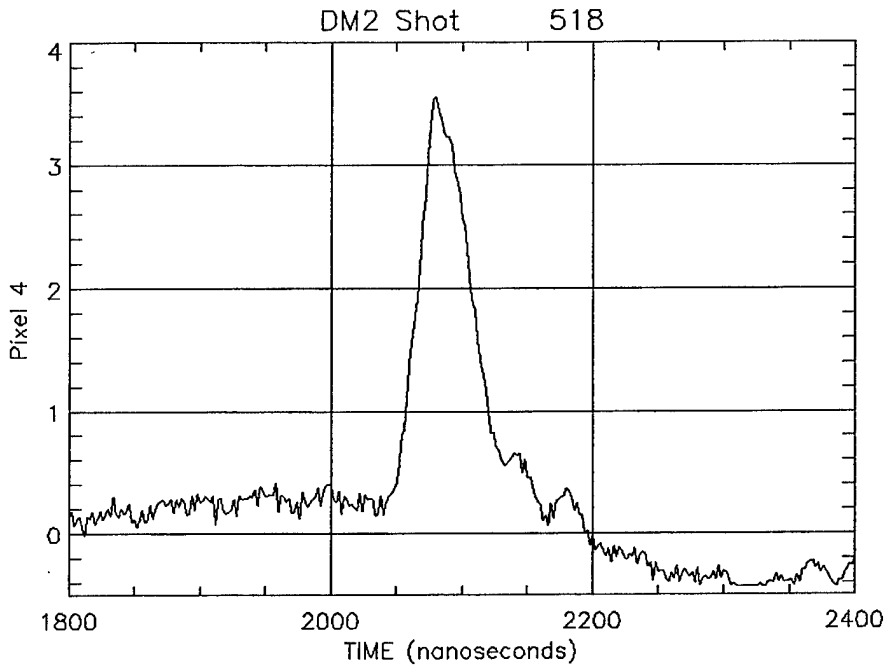

Figure 3-17. Pixel 4 signal from DM2 shot 518 shown with an expanded time scale.

[1] Prof. S. Majumdar assisted with this algorithm.

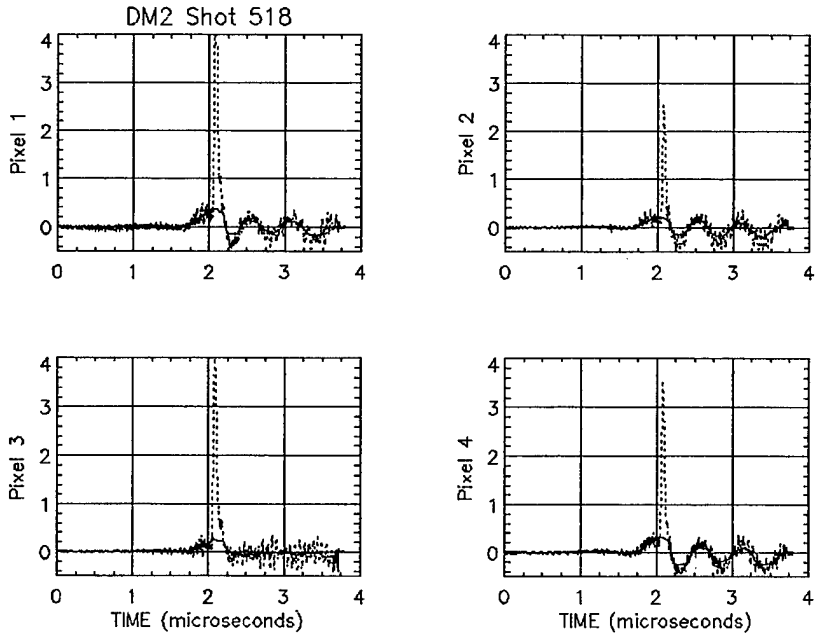

Figure 3-18. Low pass filtered signals recorded on channels 1 through 4 (solid curves) superimposed upon the raw signals (dashed curves) recorded for shot 518.

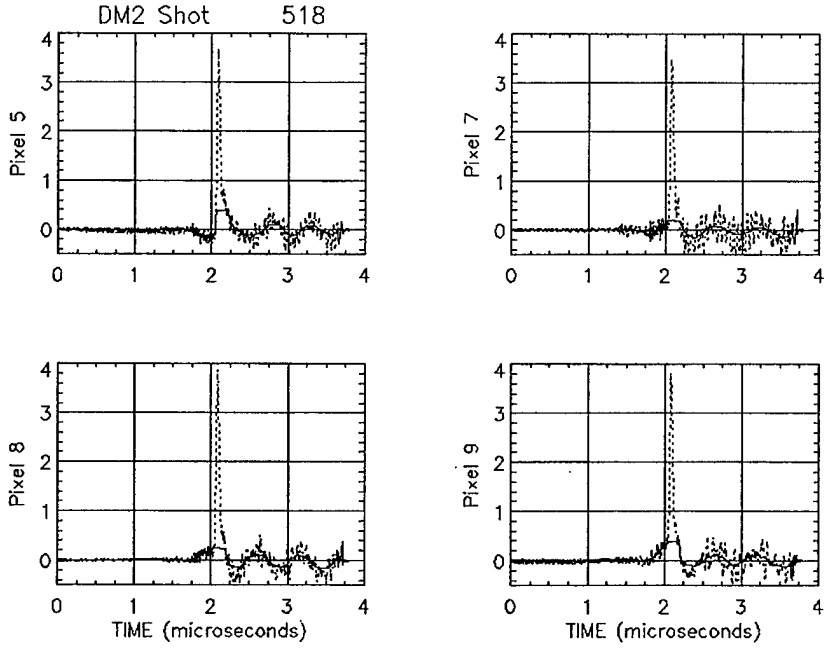

Figure 3-19. Low pass filtered signals recorded on channels 5 through 9 (solid curves) superimposed upon the raw signals recorded (dashed curves) for shot 518.

The noise can then be subtracted from the signal to yield the true x-ray pulse. Figures 3-20 and 3-21 show the corrected traces for DM2 shot 518. This simple technique can prove extremely effective when removing noise that occurs with a different frequency than the signal of interest.

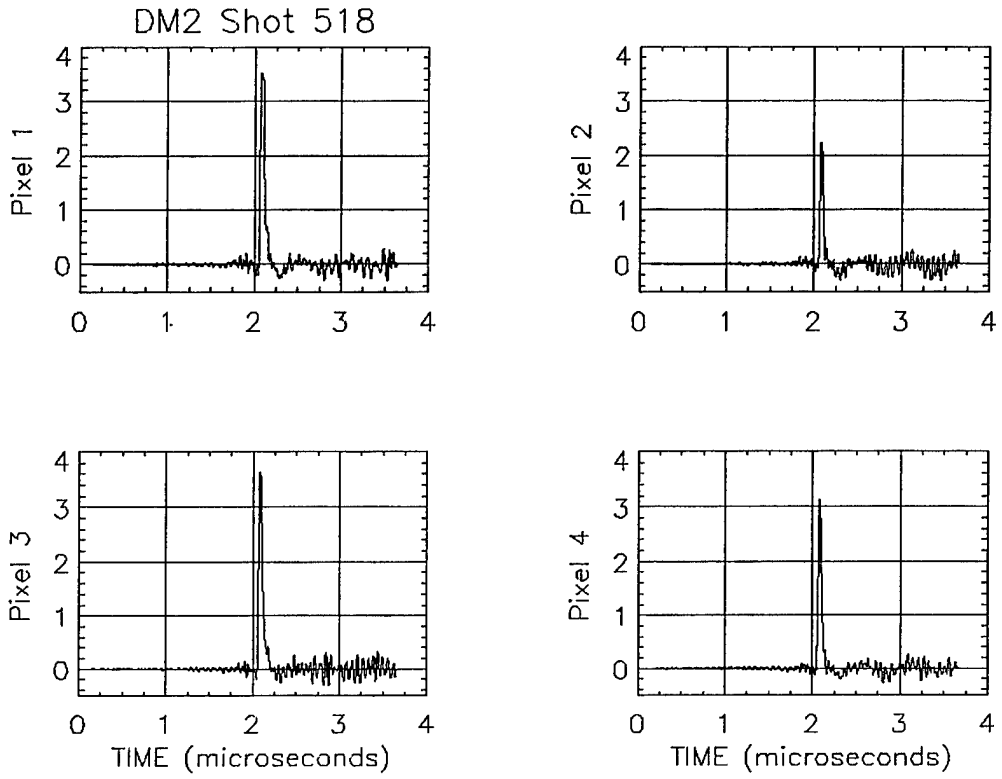

Figure 3-20. Corrected signals from pixels 1 through 4 on DM2 shot 518 using the correction algorithm described in the text. Note the flat baselines.

In order to measure crosstalk between pixels one pixel was biased while the others were not. Any signal recorded on the other channels is due to the crosstalk between adjacent pixels. The central pixel, number 5 was biased while the others were not. However, due to the short circuit between pixels 3 and 5 described earlier in this section pixel 3 was also biased. Figures 3-22 and 3-23 show the traces as captured by the digitizers on DM2 shot 524. The MPI calorimeters measured 3.5 kJ on this shot. The two biased pixels, 3 and 5 show good signals. The traces from the un-biased pixels show a signal that is indistinguishable from the noise level. However, the magnitude of the signal that is attributable to crosstalk can be recovered using the noise suppression algorithm described earlier.

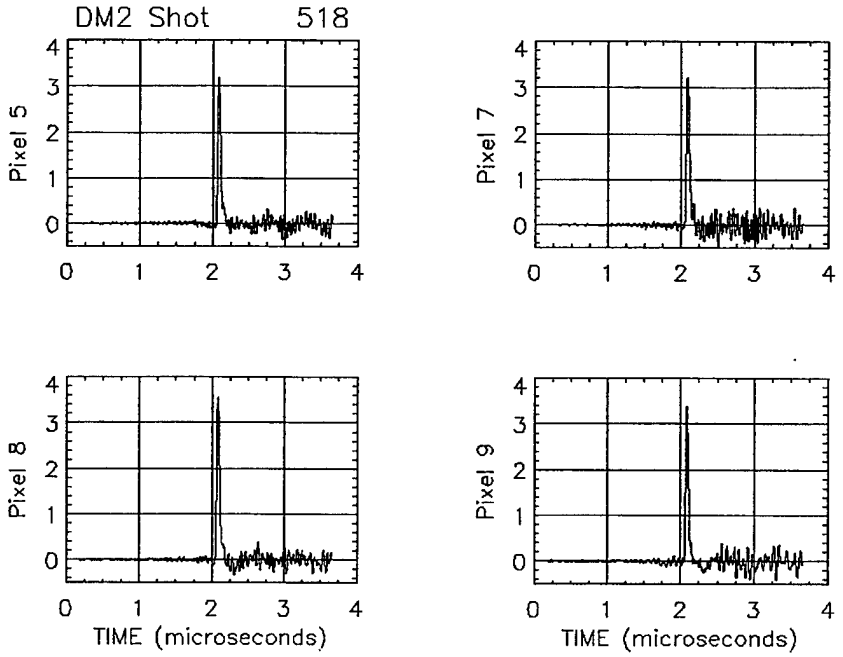

Figure 3-21. Corrected signals from pixels 5 through 9 on DM2 shot 518 using the correction algorithm described in the text. Note the flat baselines.

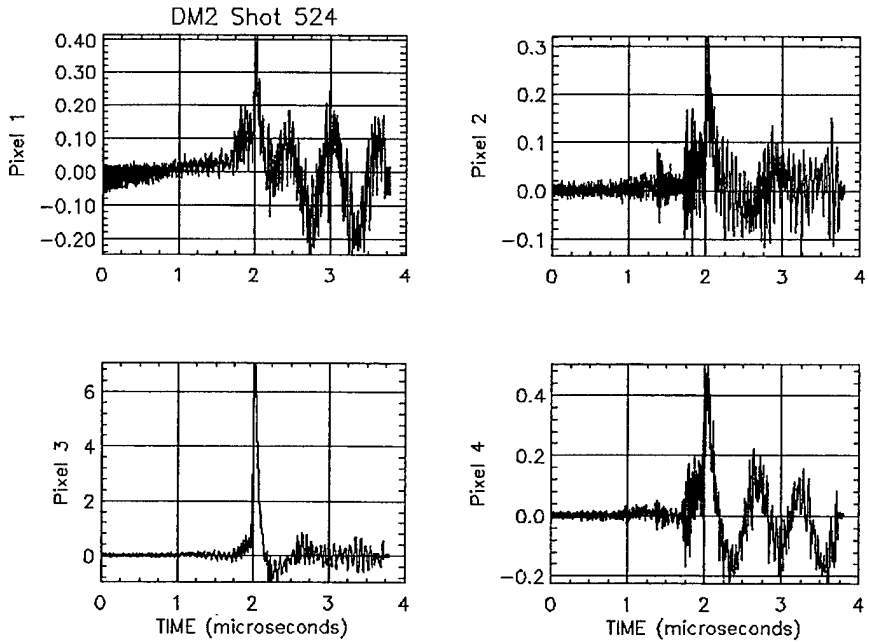

Figure 3-22. Signals digitized from pixels 1 through 4 on DM2 shot 524. As described in the text only pixel 3 from this set was biased.

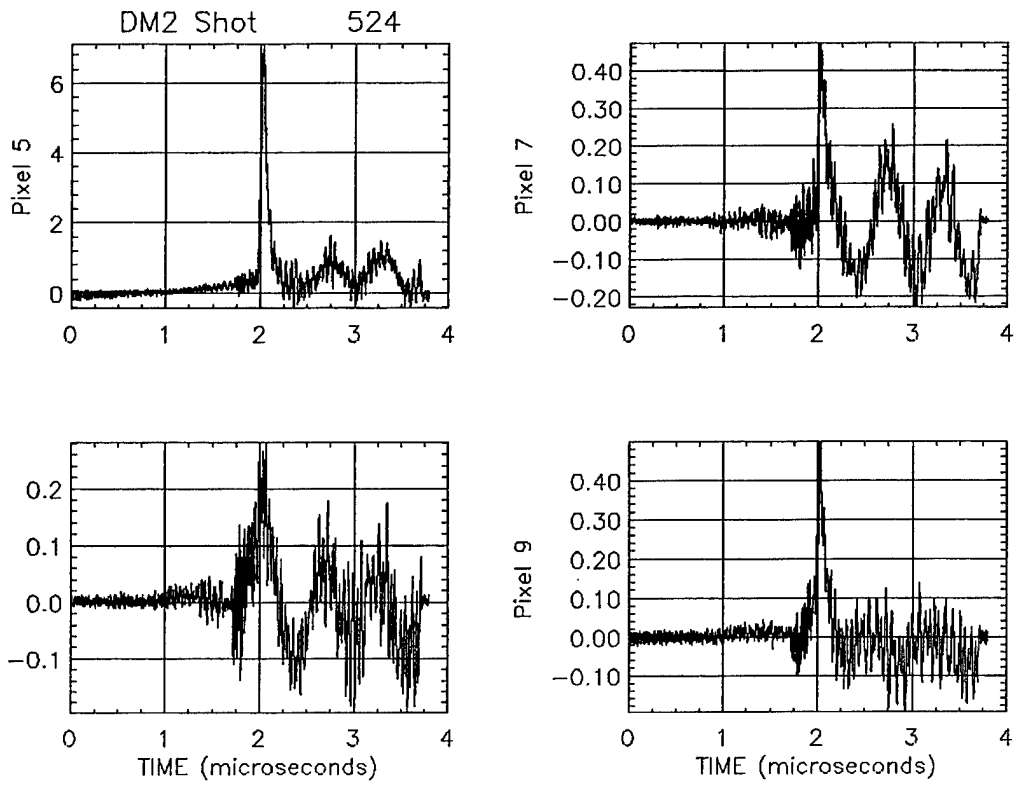

Figure 3-23. Signals digitized from pixels 5 through 9 on DM2 shot 524. As described in the text only pixel 5 from this set was biased.

The signals captured on shot 524 were corrected using the algorithm described in this section. Figures 3-24 and 3-25 show the corrected traces. Table 3-1 shows the peak value of the corrected signals. It also shows the ratio of the signals measured by the un-biased pixels to the pixels that were biased. From this table, it is evident that the crosstalk between pixels is always less than 6% and for the most part is around 3%. This is of course a worst case estimate, since in practice it is unlikely that adjacent pixels will have a range of signals from zero to peak signal. The test of the 3x3 array therefore shows that there are no problems with crosstalk or with fabrication that need to be addressed prior to the assembly of the 72-pixel camera.

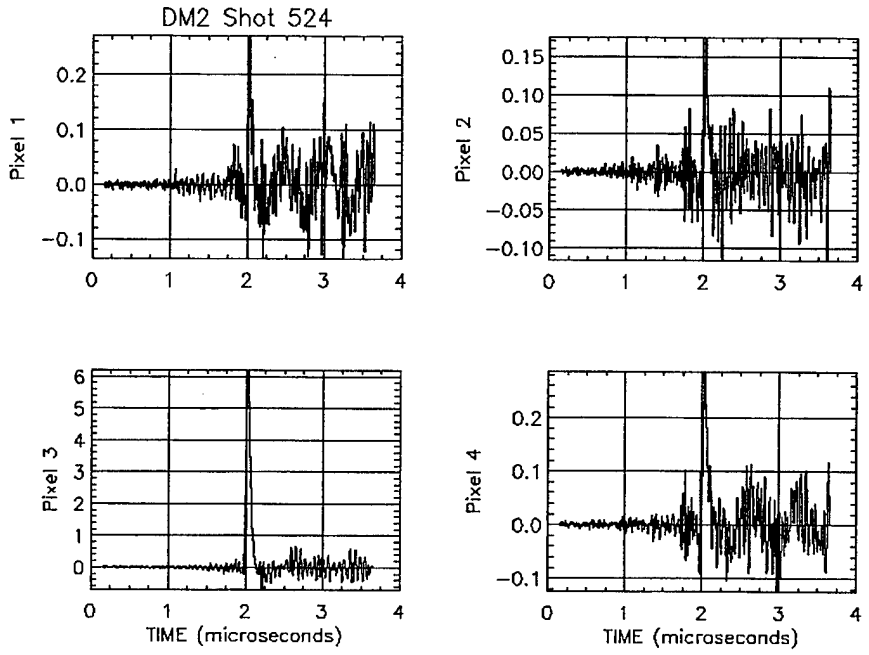

Figure 3-24. Corrected signals from pixels 1 through 4 on DM2 shot 524 using the correction algorithm described in the text.

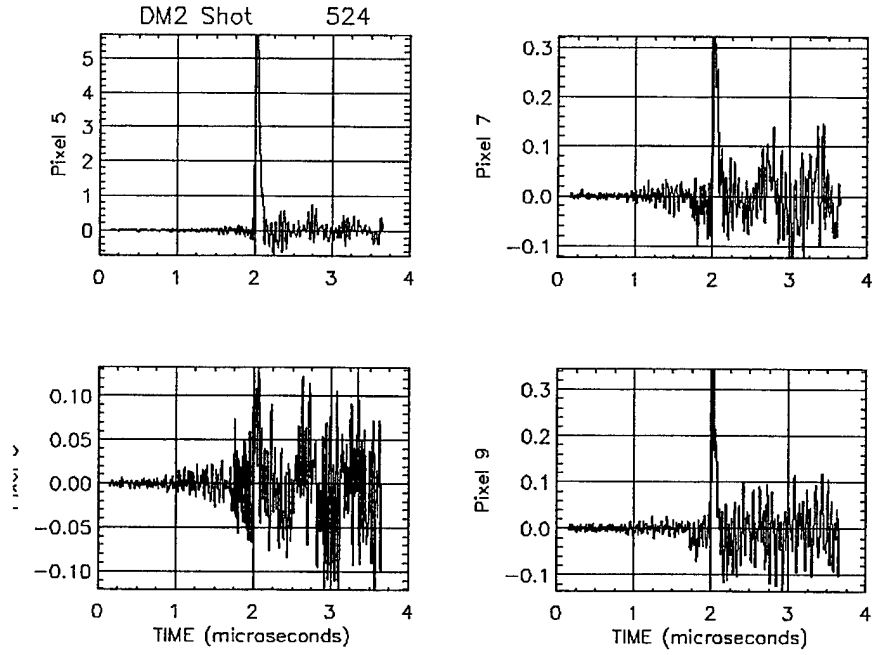

Figure 3-25. Corrected signals from pixels 5 through 9 on DM2 shot 524 using the correction algorithm described in the text.

Table 3-1. Peak signals measured on Shot 524 and their ratios to the peaks of pixels 3 and 5.

Pixel number	Peak signal	Ratio to pixel 3	Ratio to pixel 5
1	0.2693001	4.3%	4.7%
2	0.1736542	2.7%	3.0%
3	6.209703	100%	NA
4	0.2864004	4.6%	5.0%
5	5.690005	NA	100%
7	0.3220007	5.2%	5.6%
8	0.1329008	2.1%	2.3%
9	0.3444009	5.5%	6.0%

Section 4

Bias Circuit

The 72 pixel instrument will require 72 channels of digitizers and 72 bias channels. A 75 channel biasing circuit was designed and fabricated. Figure 4-1 shows the layout of this unit. There was some concern that the close proximity of so many channels might lead to crosstalk. To avoid such problems each channel is housed within its own Faraday shielded enclosure as shown in the figure. In addition, due to the use of discrete elements - capacitors and resistors - within each bias channel, there was some concern that the rise-time of the circuits might not be adequate to allow ≈1 ns temporal resolution and good signal to noise ratios. To address this issue, a prototype unit with only 3 channels was initially built. These units were tested at Sandia National Laboratory, by the kind courtesy of Dr. Guillermo Loubriel, to determine the rise-time of the bias circuits.

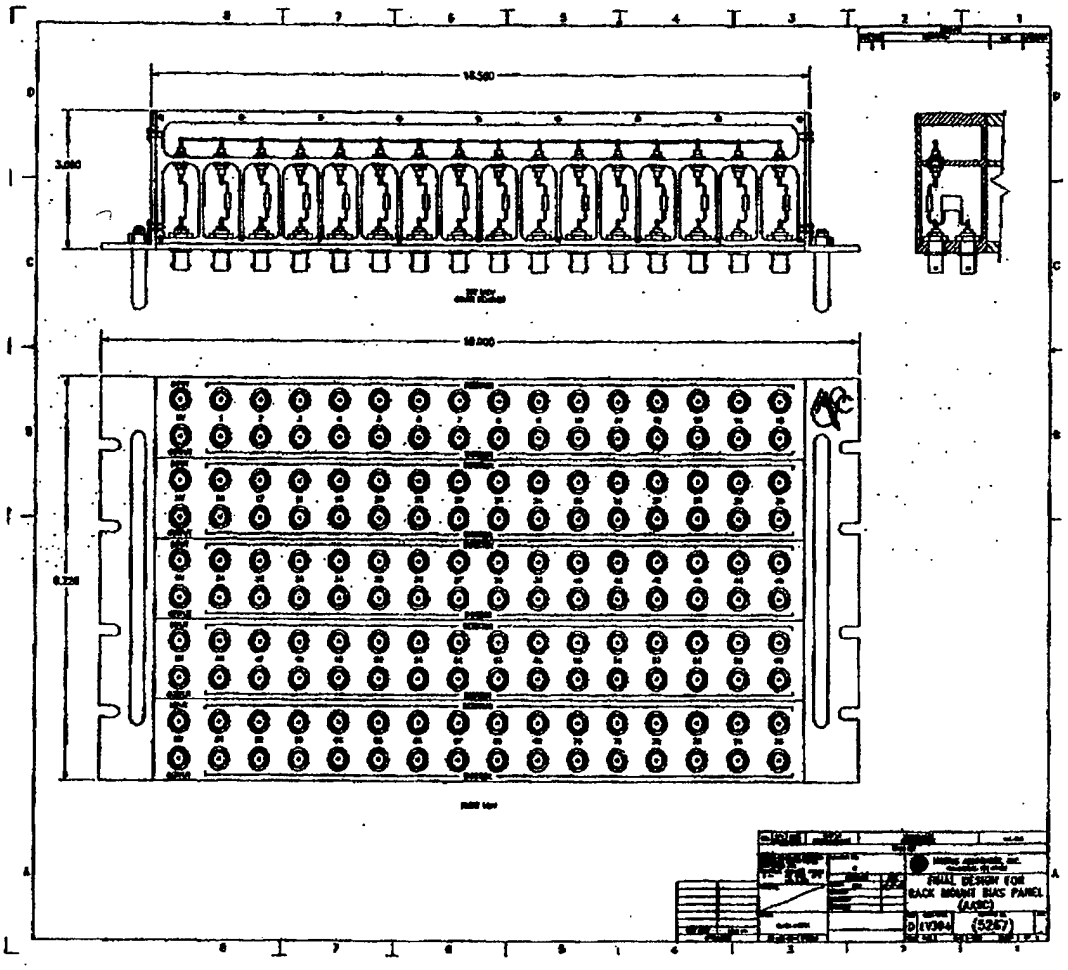

Figure 4-1. Layout of the 75 channel bias circuit and housing.

A 200 ps rise-time pulse from a Avtek pulse generator was passed through the bias circuits. The pulse temporal evolution was measured directly and through the bias circuit using a Tektronix SCD5000 5 GHz digital oscilloscope. Figure 4-2 shows the data. The direct pulse has a 200 ps rise-time while the pulse passing through the bias circuit has a 300 ps rise-time. The test was repeated with similar results for the other 2 assembled channels. It was thus established that the bias circuits are adequate and the 75 channel bias box was fabricated.

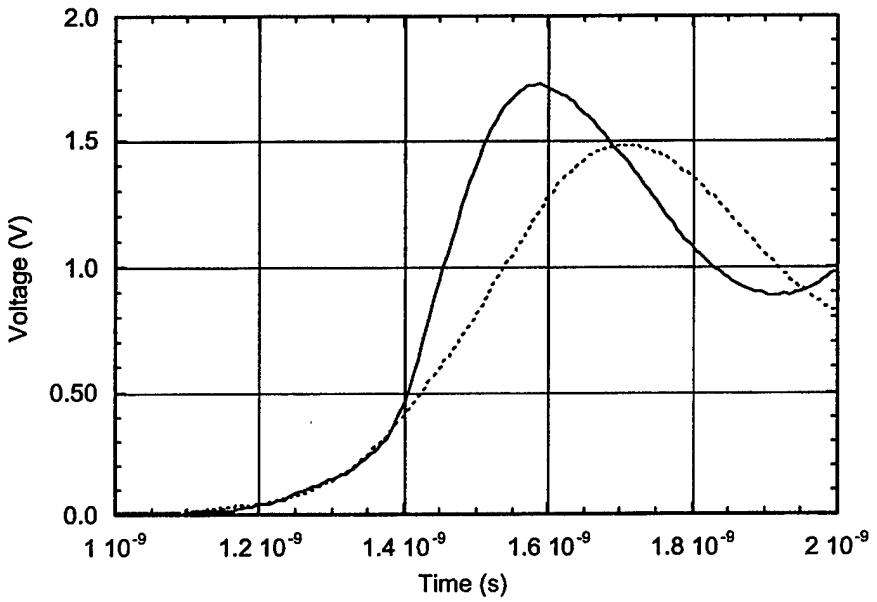

Figure 4-2. Data showing a fast pulse measured directly using a Tektronix SCD5000 5 GHz digital oscilloscope (solid curve) and passing through the detector bias circuit (dashed curve).

Section 5

Calibration at Sandia National Laboratory

The camera was calibrated at the Laser Plasma Calibration Facility at Sandia National Laboratory (SNL)[2]. The calibration facility at SNL uses a <1 ns wide, high power Nd:YAG laser operating at 532 nm focused on a solid target within a vacuum chamber to produce a plasma. For the camera calibration, the target material was Mg. The Mg plasma produced radiates in the UV and K-shell (≈1.4 keV). The pulse width of the x-radiation is about 800 ps. The UV is filtered using a 2 μm thick Al foil.

A NIST calibrated PIN diode is used to provide an absolutely-calibrated measure of the x-ray output from the laser plasma x-ray source. This diode has a slow time response, however, the output from the diode is integrated to provide a measure of the total x-ray output from the x-ray source. Figure 5-1 shows the output of the PIN diode on a typical shot. This diode was calibrated at NIST and has a sensitivity of 0.26 C/J for the 1.4 keV x-rays emitted by the Mg plasma. The diode was located 188.9 cm from the source on a beam line (called the reference) that was at 45° to the face of the Mg target. The diode has a circular active area with a 4.95-mm diameter. This is defined using a 4.95-mm diameter aperture on the face of the diode. The current generated through the diode by the x-rays is measured as a voltage using a 50-Ω terminator on the digitizer.

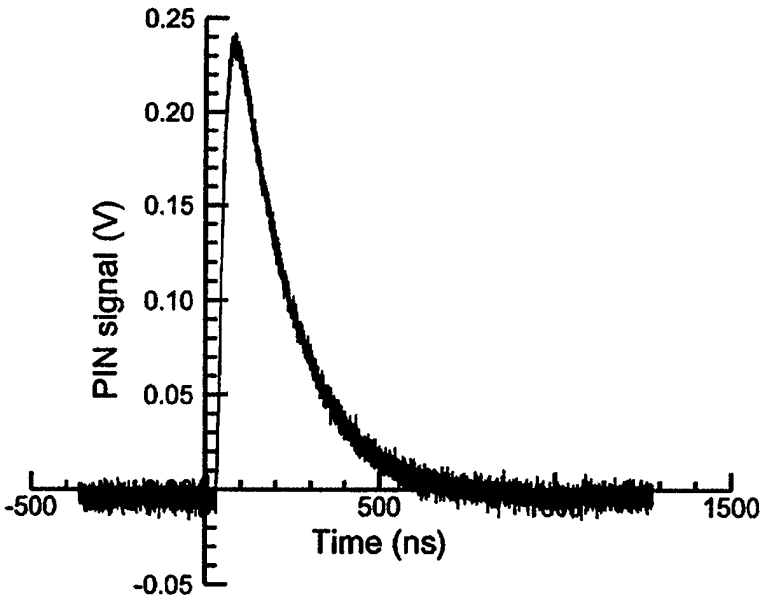

Figure 5-1. X-ray output from the laser plasma source at SNL, measured by the calibrated SNL PIN diode.

[2] Dr. R. B. Spielman of Sandia National Laboratory and Mr. L. Pressley of DTRA assisted in making these tests possible.

Assuming that the x-ray output from the source is Y Joules, the radiation incident on the diode aperture of diameter d cm at a distance of R cm from the source is:

$$\frac{Y}{2\pi R^2}\frac{\pi d^2}{4} \text{ J} \tag{5-1}$$

The charge Q generated at the diode is then:

$$0.26 \times \frac{Yd^2}{8R^2} \text{ Coulombs} \tag{5-2}$$

Thus the integral of the voltage measured at the 50 Ω terminator on the digitizer is:

$$\text{Vs} = 50 \times 0.26 \times \frac{Yd^2}{8R^2} \tag{5-3}$$

Using the values of R and d for the PIN diode and Equation (5-3), the output of the source may be calculated as:

$$Y = \text{Vs} \times 89619 \text{ J} \tag{5-4}$$

Note that the transmission of the vacuum barrier, the Al foil, has not been considered in the above calculation. This is because the same material is used to filter the diamond camera, making the knowledge of the transmission of the filter to the exact spectrum being emitted by the source irrelevant.

The diamond camera was mounted on a beam line that is at 30° to the face of the target at a distance of 52.1 cm from the source. The output of the source measured by the PIN diode may be used to determine the sensitivity of each of the diamond detectors in the camera. However, since the two beam lines used to mount the calibrated PIN diode and the diamond camera are not at the same angle with respect to the source, it is essential to first determine what fraction of the radiation measured in the calibrated PIN diode beam line is incident on a detector within the diamond camera beam line.

This was accomplished by locating another calibrated PIN in the diamond camera beam line. The second PIN diode had an aperture of 4.99 mm and was mounted 168.8 cm from the source. Using these parameters in Equation (5-3) the output measured by this detector Y_D is:

$$Y_D = \text{Vs}_\text{D} \times 70419 \text{ J} \tag{5-5}$$

where Vs_D in the integral of the voltage measured by the second detector. Table 5-1 shows the outputs measured by these two detectors in 4 successive shots. The ratio of the diamond camera beam line detector to the reference PIN diode is also listed. It is seen that the diamond camera beam line receives 89% of the flux that the reference beam line does.

Table 5-1. Ratio of output measured along the diamond camera beam line and the reference beam line.

Shot No.	Reference (ref) output	Diamond Camera (DC) beam line output	Ratio: DC/ref
1	6.48 mJ	5.75 mJ	0.89
2	5.92 mJ	5.27 mJ	0.89
3	7.11 mJ	6.36 mJ	0.89
4	7.32 mJ	6.39 mJ	0.87

Figure 5-2 shows the output of one of the 72 diamond detectors that make up the diamond camera, digitized using a Tektronix TDS684A digitizer at 5 Gsamples/sec (200 ps per point). It is clear from the trace that the limit of temporal resolution is the digitizer.

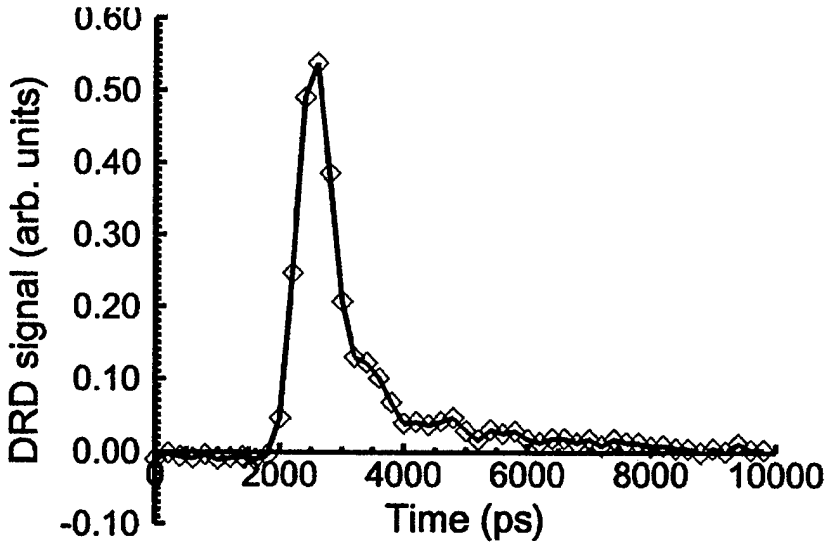

Figure 5-2. X-ray output from the laser plasma source at SNL, measured by one of the diamond detectors within the diamond camera.

The sensitivity of each of the pixels is determined by using the following algorithm. The radiation incident on a square detector of area A cm^2, located R_D cm from the source, when an output of Y Joules is measured by the reference detector is given by analogy to Equation (5-1) by:

$$\frac{0.89 \times Y}{2\pi R_D^{\,2}} A \text{ J} \tag{5-5}$$

Assuming that the detector sensitivity is S, the integral of measured voltage on the detector in Volt-seconds is given by:

$$Vs_D = 50 \times S \times \frac{0.89 \times YA}{2\pi R_D^{\,2}} \tag{5-6}$$

The sensitivity of the detector is then given by:

$$S = \frac{Vs_D}{Y} \times 3.83 \times 10^4 \text{ J} \tag{5-7}$$

There were 40 channels of digitizers available to capture data from the diamond camera. Thus, the camera was calibrated in two sets of shots. The 72 pixels in the camera are numbered according to the following convention: i,j where i represents the pixel row ranging from 1 through 6 and j represents the pixel column ranging from 1 through 12. The first 40 pixels were calibrated on the first set of shots. These were pixels 1,1 through 1,12, 2,1 through 2,12, 3,1 through 3,12 and 4,1 through 4,4. Then 8 pixels (1,1 through 1,8) of the first set were retained and other 32 swapped for new pixels (4,5 through 4,12, 5,1 through 5,12 and 6,1 through 6,12). These were then calibrated on the second set of shots The 8 common pixels were retained to provide a consistency check. All pixels were biased for all shots.

Figure 5-3 shows the data for pixels 1,1 through 3,12. The first set of shots includes shots 3,4 and 5. The second set consists of shots 7,8,9 and 11. Data from pixels 1,1 through 1,8 were acquired for all shots, the other pixels were digitized only in the first set of shots. While the calibration factors of different pixels varies the calibration factor of individual pixels does not change significantly from shot to shot. In fact, in most pixels the standard deviation of the calibration factors is less than 10%. The data show that pixel 3,9 does not work. A contact, either to the diamond or in a cable is disconnected. The sensitivity of pixel 2,12 is small, however, close examination shows that it is a working pixel. The data for pixels 1,1 through 1,8 is shown in an expanded scale in Figure 5-4.

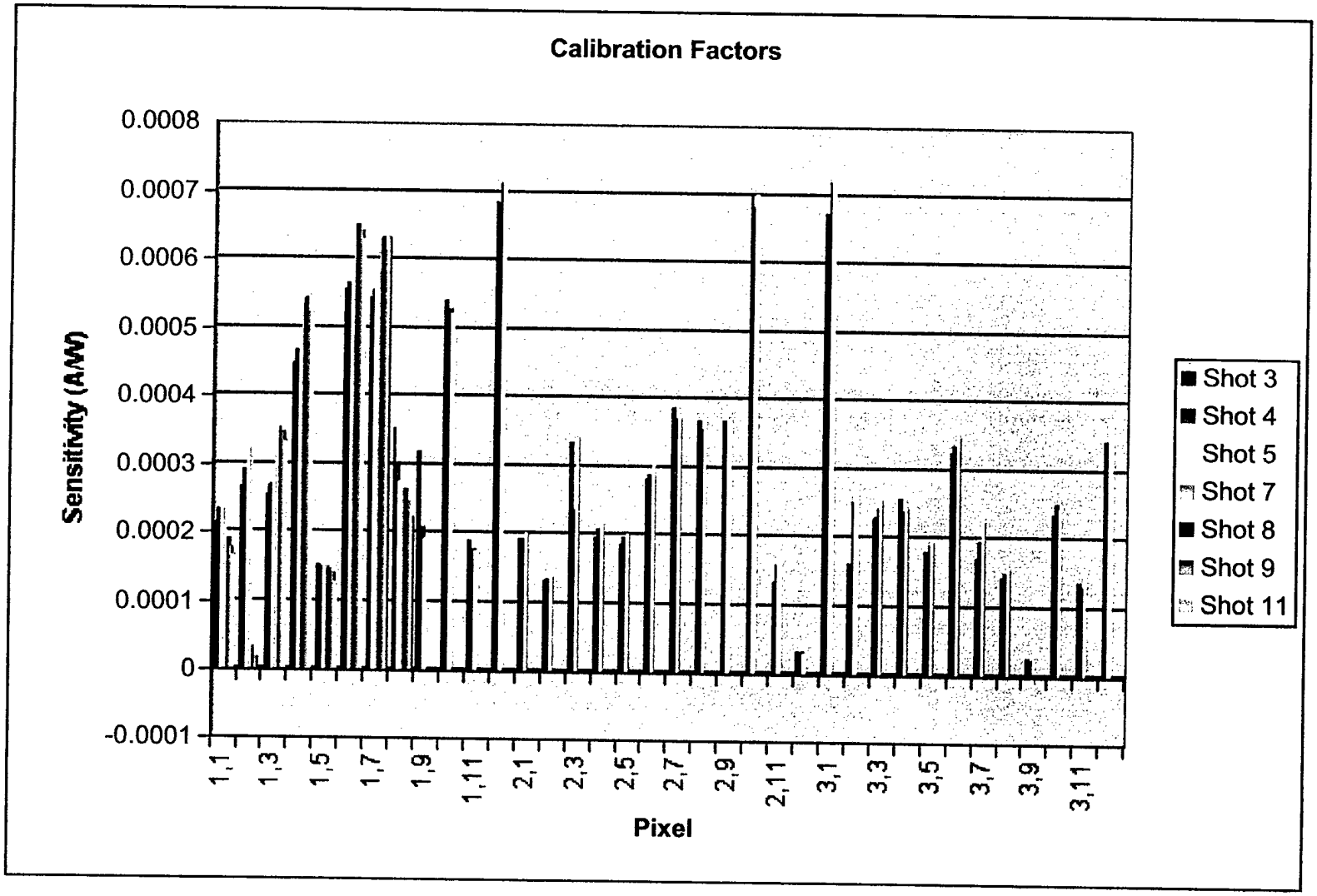

Figure 5-3. Sensitivity of pixels 1,1 through 3,12 in the diamond camera.

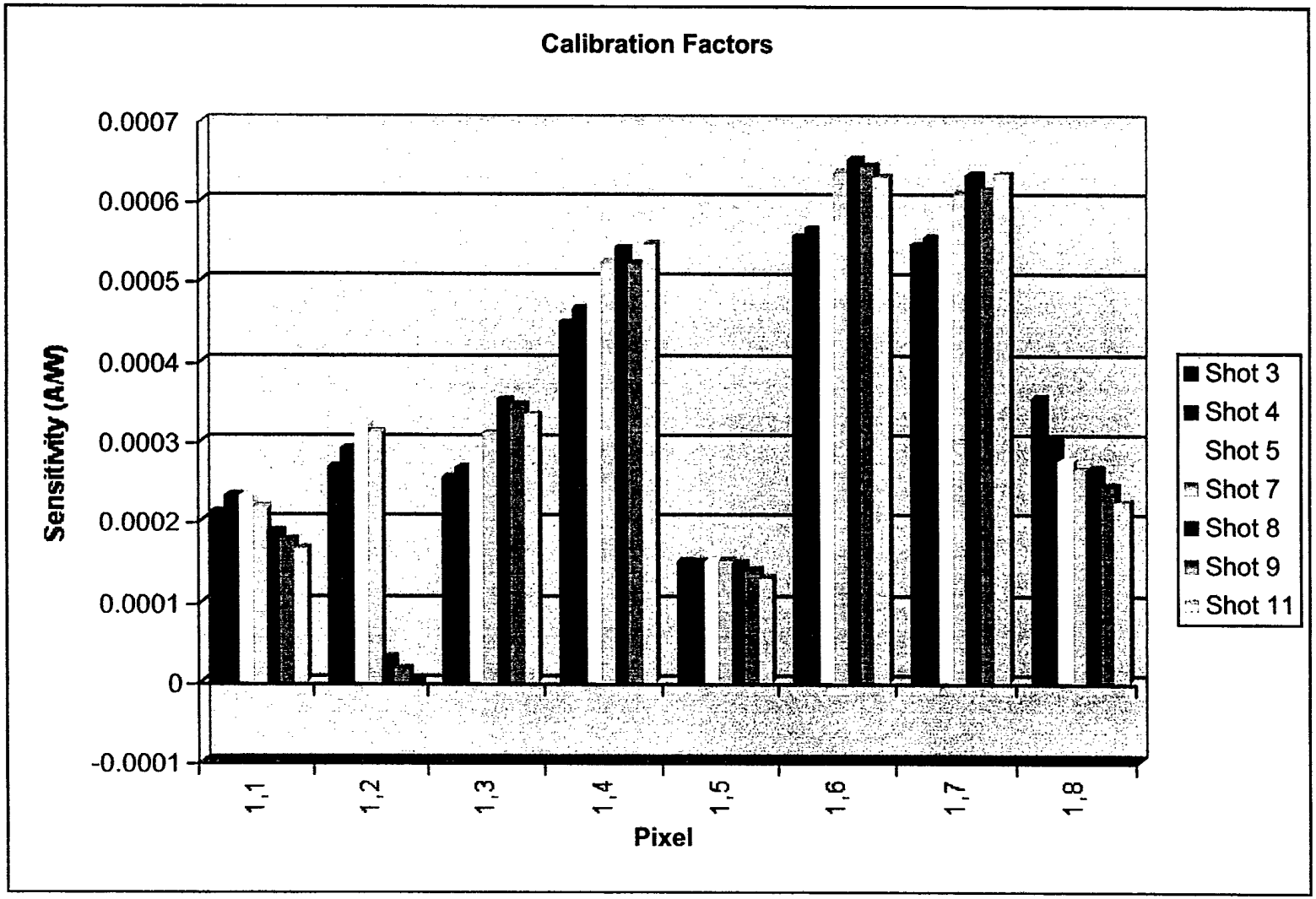

Figure 5-4. Sensitivity of pixels 1,1 through 1,8. Data from both sets of shots are shown.

Another point to be noted is that pixel 1,2 appears to have been working initially and then stopped working, as evidenced by the low sensitivity. This is not the case. The pixel was deliberately unbiased for shots 8,9 and 11 to determine if the removal of bias from one pixel changes the sensitivity of the neighboring pixels. It is seen from the data that the removal of the bias from pixel 1,2 had no effect on the sensitivity of pixels 1,1 or 1,3. In addition, on shot 9 the bias was removed from pixel 2,1 and on shot 11 bias was removed from pixels 2,1 and 2,2. Again, it can be seen that there is no change in the sensitivity of the nearest neighbors, pixels 1,1 and 1,3 on any of these shots.

Figures 5-5 and 5-6 show the data for the rest of the pixels. Data from pixels 1,9 through 3,12 are shown in Figure 5-5. Data from pixels 4,1 through 6,12 are shown in Figure 5-6. The average sensitivity and the standard deviation of the measurement are shown for each pixel in Table 5-2.

In addition to calibrating the diamond camera, five standard AASC diamond radiation detectors were also calibrated during this session at Sandia National Laboratory. These were calibrated to determine if the sensitivity changes due to detector aging. Figure 5-7 shows a standard AASC diamond detector. The detector elements are 3 mm x 1 mm in area. The detectors were located on a beam line at 45° to the target face at a distance of 34.5 cm from the source. The factor of 0.89 in Equation (5-6) can be dropped since the diamond detector beam line is at 45° as was the reference beam line. Using the distance from the source and the area of the diamond detectors, their sensitivity can be calculated from Equation (5-6) as:

$$S = \frac{Vs_{DRD}}{Y} \times 4.99 \times 10^{3} \ \ J \qquad (5\text{-}8)$$

where Vs_{DRD} is the integral of the voltage (in Volt-seconds) measured across a 50-Ω terminator on the digitizers connected to the detectors.

Table 5-3 shows the average sensitivity of the five detectors as determined on the same shots that were used to calibrate the camera and the standard deviation of the measurements. As with the detector elements in the diamond camera the standard deviation of the measurement of detector sensitivity over several shots is small and less than 10% in most cases.

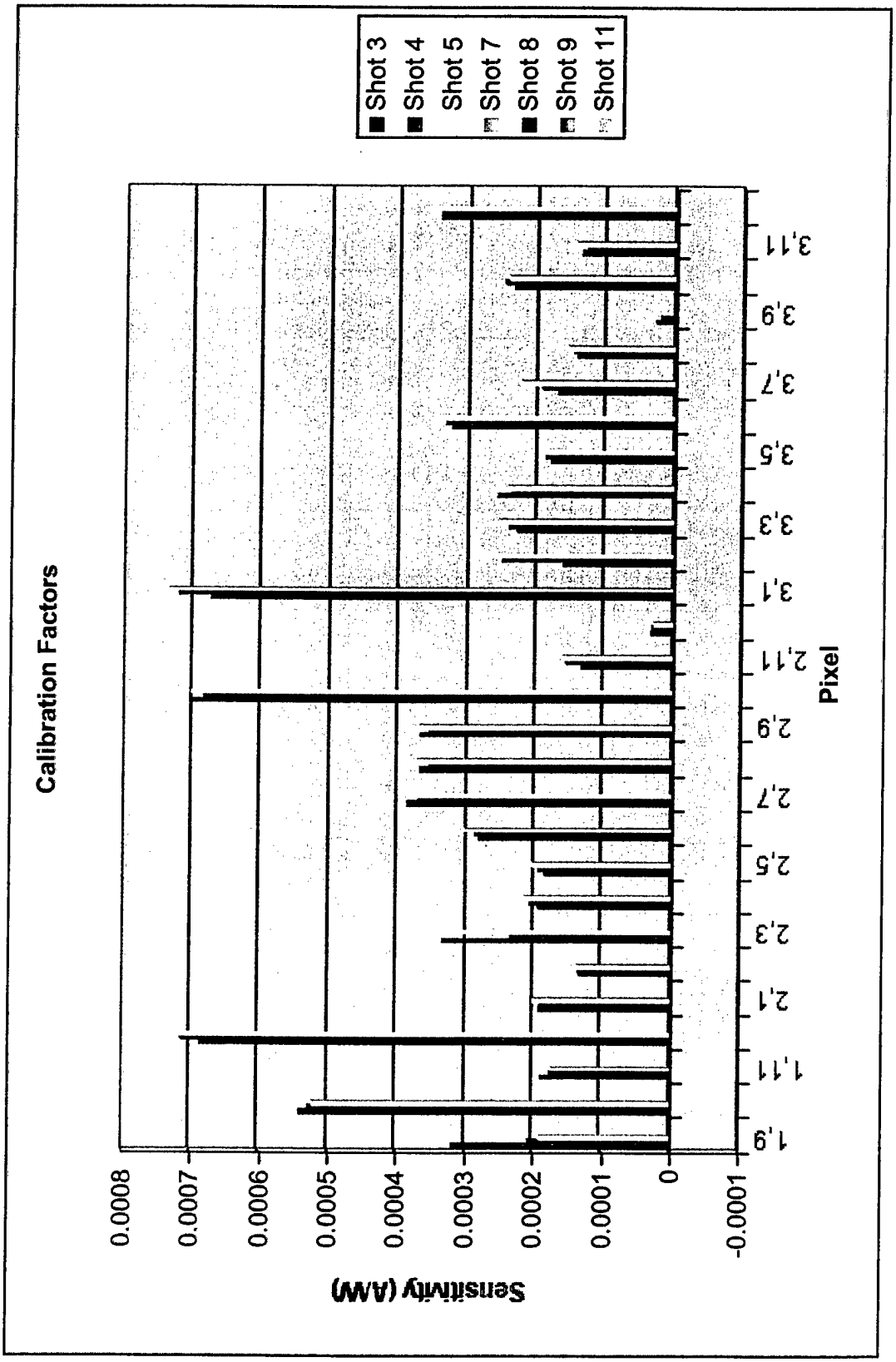

Figure 5-5. Sensitivity of pixels 1,9 through 3,12 in the diamond camera.

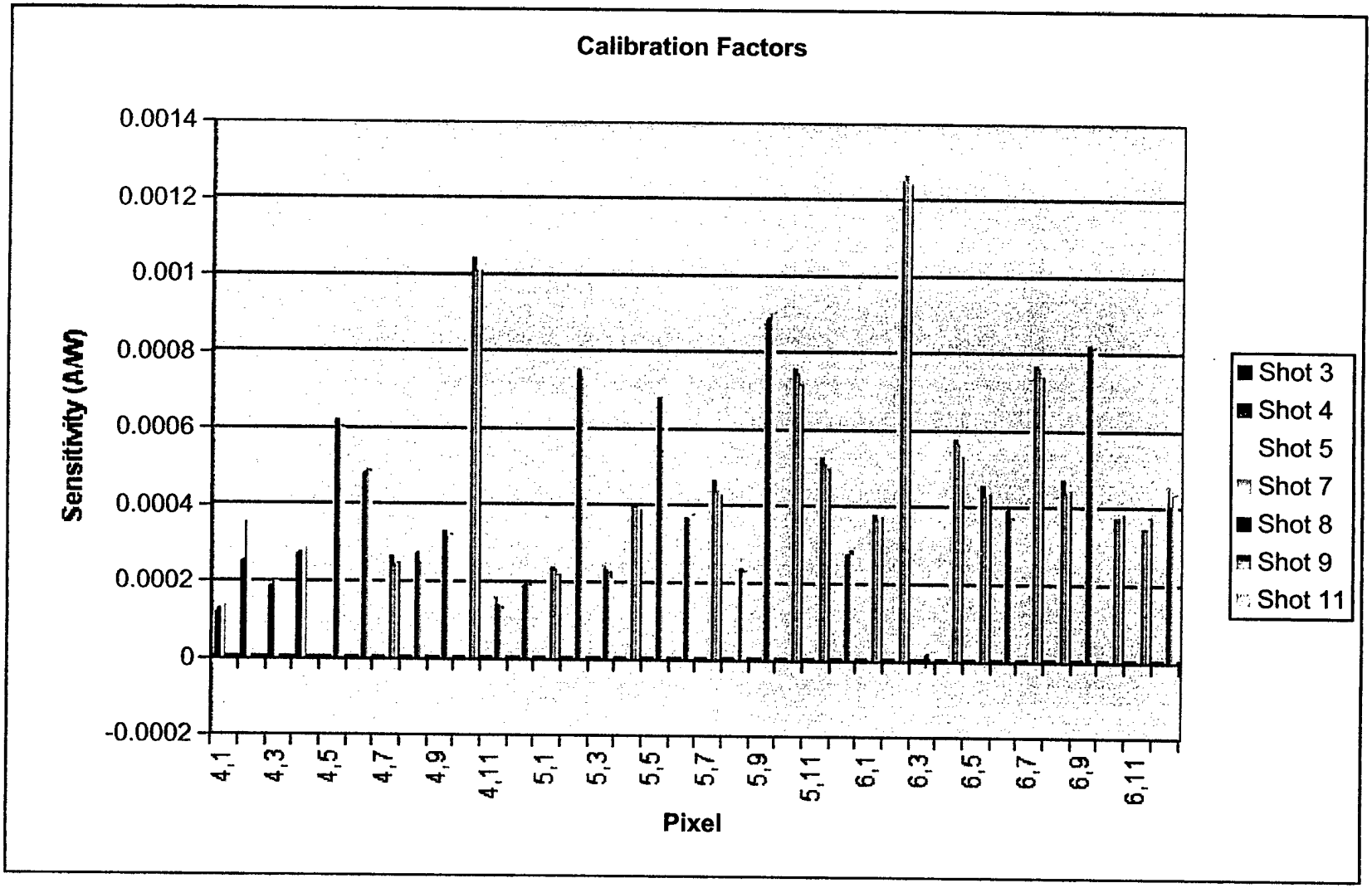

Figure 5-6. Sensitivity of pixels 4,1 through 6,12 in the diamond camera.

Table 5-2. Average sensitivity of each pixel of the diamond camera.

Pixel	Average Sensitivity (A/W)	Standard deviation %	Pixel	Average Sensitivity (A/W)	Standard deviation %
1,1	1.95E-04	18%	4,1	1.27E-04	7%
1,2	2.98E-04	8%	4,2	3.27E-04	20%
1,3	3.15E-04	14%	4,3	1.94E-04	4%
1,4	5.30E-04	14%	4,4	2.78E-04	4%
1,5	1.43E-04	7%	4,5	6.15E-04	6%
1,6	6.24E-04	10%	4,6	4.88E-04	7%
1,7	6.10E-04	8%	4,7	2.43E-04	10%
1,8	2.73E-04	14%	4,8	2.79E-04	15%
1,9	2.40E-04	29%	4,9	3.26E-04	5%
1,10	5.30E-04	2%	4,10	1.05E-03	8%
1,11	1.79E-04	5%	4,11	1.60E-04	29%
1,12	7.22E-04	6%	4,12	2.07E-04	16%
2,1	1.96E-04	3%	5,1	2.23E-04	9%
2,2	1.35E-04	3%	5,2	7.58E-04	7%
2,3	3.03E-04	20%	5,3	2.33E-04	7%
2,4	2.06E-04	5%	5,4	4.09E-04	13%
2,5	1.95E-04	4%	5,5	6.50E-04	10%
2,6	2.90E-04	4%	5,6	3.69E-04	5%
2,7	3.76E-04	2%	5,7	4.52E-04	5%
2,8	3.65E-04	3%	5,8	2.31E-04	2%
2,9	3.64E-04	2%	5,9	9.29E-04	9%
2,10	6.96E-04	2%	5,10	7.90E-04	15%
2,11	1.51E-04	10%	5,11	5.35E-04	10%
2,12	3.10E-05	6%	5,12	2.85E-04	8%
3,1	7.10E-04	5%	6,1	3.67E-04	4%
3,2	2.31E-04	27%	6,2	1.32E-03	14%
3,3	2.42E-04	5%	6,3	8.12E-06	201%
3,4	2.46E-04	4%	6,4	5.78E-04	9%
3,5	1.88E-04	3%	6,5	4.46E-04	3%
3,6	3.36E-04	4%	6,6	3.81E-04	4%
3,7	1.97E-04	14%	6,7	7.70E-04	6%
3,8	1.51E-04	5%	6,8	4.60E-04	7%
3,9	1.00E-06	160%	6,9	8.25E-04	7%
3,10	2.43E-04	3%	6,10	4.03E-04	19%
3,11	1.38E-04	6%	6,11	3.60E-04	8%
3,12	3.52E-04	4%	6,12	4.50E-04	9%

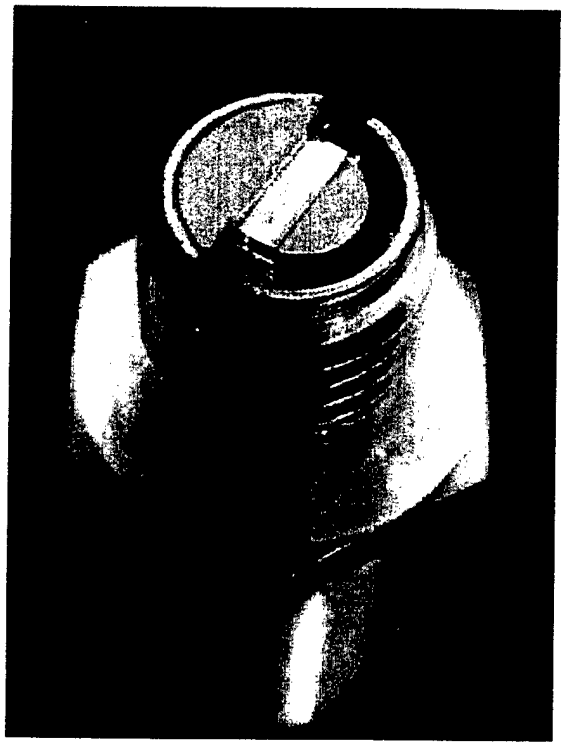

Figure 5-7. AASC standard diamond radiation detector.

Table 5-3. Sensitivity of five diamond radiation detectors also calibrated at Sandia.

Detector	Average Sensitivity (A/W)	Standard Deviation %
DRD1	3.03E-04	7%
DRD2	2.80E-04	6%
DRD3	4.99E-04	14%
DRD4	1.53E-04	6%
DRD5	2.70E-04	4%

Section 6

Camera Validation on Double-Eagle

Once the calibration of each pixel was completed, the diamond camera was ready for a validation test on Double-EAGLE. In October 1998, a test of long implosions of Ar was scheduled on Double-EAGLE. The AASC camera was given a beam line on these tests. This section discusses the details of these validation tests.

The diamond camera is shown in Figure 2-1. The camera housing ends in an 8" conflat flange that can be bolted to the end of a beam line on a simulator such as Double-EAGLE or Decade Quad. As discussed in Section 2.3, the camera images the source by the use of a pinhole (or arrays of pinholes), located between the z-pinch source and the diamond array. For the validation tests, a single pinhole was used to provide an image of the z-pinch.

Once the camera has been mounted on a beam line, it is important to align the pinhole, detector array and the z-pinch source. This was done using a bright light source, such as a small halogen lamp, at the pinch location and observing the image of the light source at the plane of the detector array. The pinhole can be moved with two degrees of freedom (as shown later in Section 6.1) to allow the image of the light source to be located directly on top of the detector array. If the light source is properly located then the z-pinch will be imaged on the detector array.

The camera may be configured to image only parts of the spectrum. A filter or group of filters may be mounted either at the pinhole location or at the diamond array to filter out parts of the spectrum emitted from the z-pinch. For example, a 1 μm Kimfol filter may be used to image photons with energies >100 eV. A 25 μm Be filter may be used to image photons with energies >1 keV. Other filters with absorption edges can also be used to selectively image only a small portion of the spectrum of radiation emitted by the z-pinch source.

Finally, the BNC connectors on the air-side of the camera housing were connected to the inputs labeled 'detector' on the 75 channel bias box. A 100 V dc voltage was required for the bias box. Internal cabling within the bias box distributes this voltage to all the detectors connected to it. The output connectors were labeled 'digitizer' and were connected to the digitizers. The cables to the digitizers were terminated in 50 Ω for optimal temporal resolution from the camera.

Only 36 pixels configured in a 6x6 array were used for this test. The lack of feedthroughs into the Double-EAGLE user screen room necessitated the use of only 36 pixels. The cables connecting the camera pixels to the bias box (located in the user screen room) were double shielded to reduce noise pickup[3]. Ten Tektronix TDS644 digitizers were rented for the duration of the experiment. These are capable of digitizing the signals from the camera at 400 ps/sample.

The voltage measured by the digitizers is proportional to the intensity of radiation incident on each of the detectors in the array. Multiplying this voltage by the sensitivity of each of the detectors provides a relative measure of the intensity at each pixel, thereby providing images of the pinch.

[3] Mr. A. Verma and Mr. J. Quintana of FC/DTRA assisted in providing these double shielded cables.

Absolute intensity images may also be obtained by taking into account the geometry of imaging and the absolute sensitivity of the diamond detectors.

A LabView program[4] running on a Macintosh PowerBook notebook computer was used to control these digitizers and analyze the data. The 36 detector elements used in these validation tests were digitized independently. These 36 linear arrays were used as the input for the data reduction program. This program is written in IDL, a data analysis and display language developed by Research Systems Incorporated.

The sequence of steps to generate images is as follows:

1. Data from the diamond detectors are digitized using digital oscilloscopes or digitizers and stored in ASCII format on the Macintosh.

2. The ASCII file is read by the analysis program. A time vector corresponding to the digitizer sampling speed is created.

3. Data from each pixel, representing the voltage developed across the 50 Ω termination resistor, is converted into the current driven through each detector by dividing the data by 50. Division by the relative sensitivity of each pixel (in A/W) yields the intensity of the radiation incident on each pixel.

4. The 36 linear arrays of N points each, where N is the number of digitizer samples captured, is then converted into N images of 6x12 element arrays. Each 6x12 element array represents a digital image of the pinch captured at the digitizer sampling rate.

5. Images with the data prior to the x-ray pulse and after the end of the x-ray pulse are then discarded. The analysis program then scales all the remaining images to the peak intensity measured over the entire duration of the x-ray pulse. Contours of equal intensity, ranging from 10 to 100, where 100 represents the brightest pixel, are drawn after the data are interpolated using a cubic spline technique. These images are stored on the Macintosh using JPEG format. They can be later viewed individually or as a movie using an image viewer such as Graphic Converter, a shareware program.

6.1 Design of Double-EAGLE Beam Line.

Figure 6-1 shows a schematic of a beam line design for Double-EAGLE. The 6" conflat flange, shown at 54.75" from the z-pinch is the flange on the Double-EAGLE vacuum chamber. Using the re-entrant design shown, the pinhole is located at 32.95" from the source. The camera is mounted downstream of a gate valve as shown in the figure. The diamond pixels are located 62.9" from the source. In the configuration shown, the camera has a 1:1 magnification. The camera can easily be re-configured with the addition of a 1.5" OD tube with 2.75" conflat flanges to reduce the distance of the pinhole to 20.96" from the z-pinch. In this case, the magnification would be increased to 2:1. Other magnifications or de-magnifications can be similarly achieved.

[4] Mr. R. Broyles of Sandia National Laboratory wrote this data acquisition software.

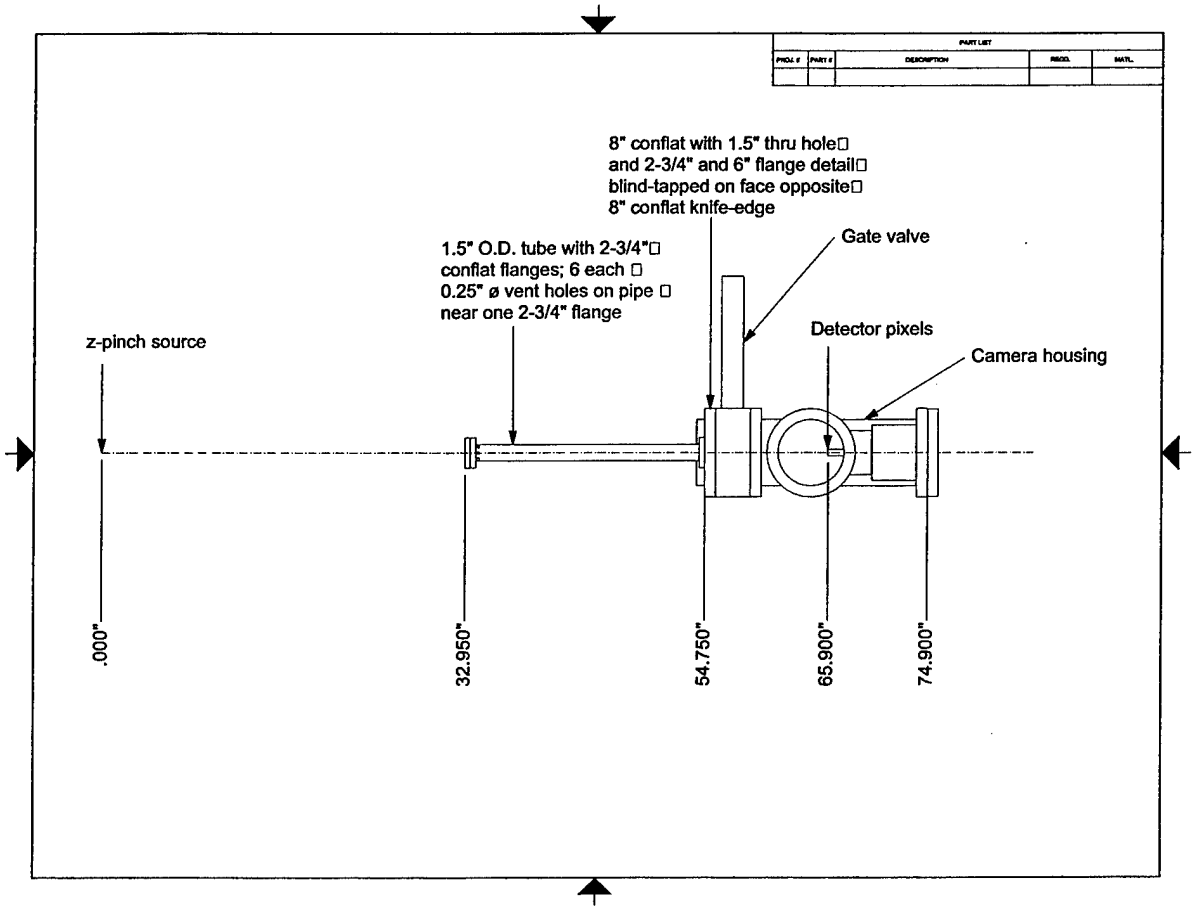

Figure 6-1. Schematic of the beam line used for the validation tests on Double-EAGLE.

The pinhole is mounted at the end of the 1.5" OD tube on a New Focus fiber optic support stage, model 9051. This stage allows for ±1.5 mm of X-Y travel to align the pinhole relative to the source and camera. The New Focus stage is mounted to the 2.75" conflat flange as shown in Figure 6-2. This mounting allows for an additional ±3 mm of travel to align the camera to the source.

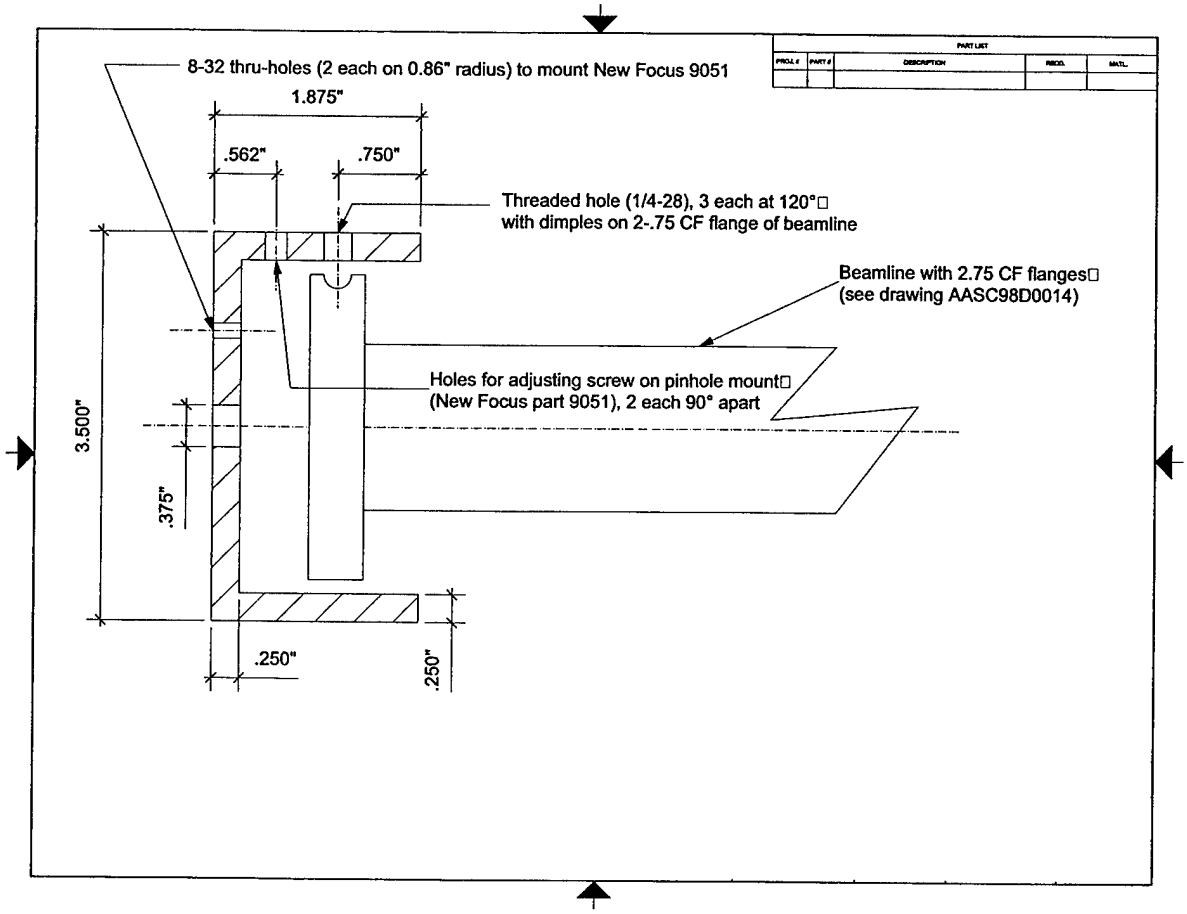

Figure 6-2. Schematic drawing showing the pinhole mount at the end of the 2.75" conflat flange.

The alignment of the diamond camera proved to be a greater challenge than anticipated. The port that was assigned for the use of the diamond camera, shown in Figure 6-3, had a 6" conflat flange welded to it to mount diamond camera. This flange was not welded properly, with the end-result that the face of the flange was not perpendicular to the axis of the port. This necessitated the use of washers to artificially bend the re-entrant section of pipe with the pinhole mount to allow proper alignment. This led to the waste of several shots with no data. However, once the alignment was completed a shot was taken with the pinhole removed to measure the flat field response of the diamond camera on Double-EAGLE. It was found that the calibration agreed to better than 10% for all 36 pixels tested on Double-EAGLE. The following sub-sections describe imaging results from diamond camera.

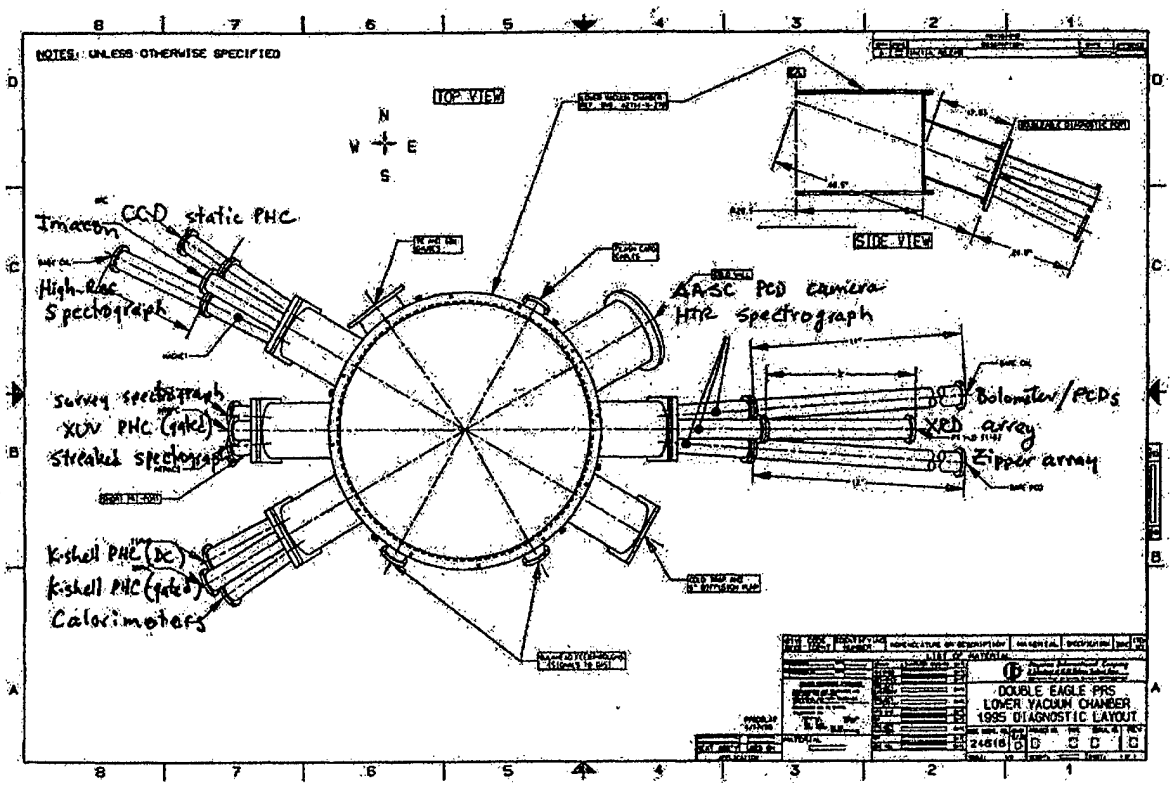

Figure 6-3. Schematic showing the beam line layout on Double-EAGLE and the beam line used for the diamond camera during the validation tests.

6.2 Spatial Resolution.

The diamond camera validation test was performed as a ride-on to the test of long implosions of Ar gas puffs on Double-EAGLE during late September, 1998 and October, 1998. An attempt was made to keep the Ar output constant, since this set of tests was being utilized by MPI to develop their own suite of diagnostics.

The diamond camera was used with two sets of filters. One was 16.9 μm of aluminized Kapton that transmits only the K-shell of Ar around 3.3 keV. Details from these shots will be presented later in this section. The second filter was 2 μm of aluminized Kimfol. This filter only blocks the visible and soft UV emissions of the pinch. Figure 6-4 shows the Ar L shell spectrum[5] and the transmission of the 2 μm Kimfol filter. Note that the filter has only a small transmission (≤10%) in the most prolific part of the spectrum (400-500 eV). The standard aluminized filters have a layer of aluminum ranging from 1500 – 2000 Å thick coated on the filter. This is done to prevent visible light and soft UV from impinging on the detector. The transmission of this Al filter to photons more energetic than 100 eV is essentially 100%.

[5] Spectrum courtesy of Dr. F. Young, Naval Research Laboratory.

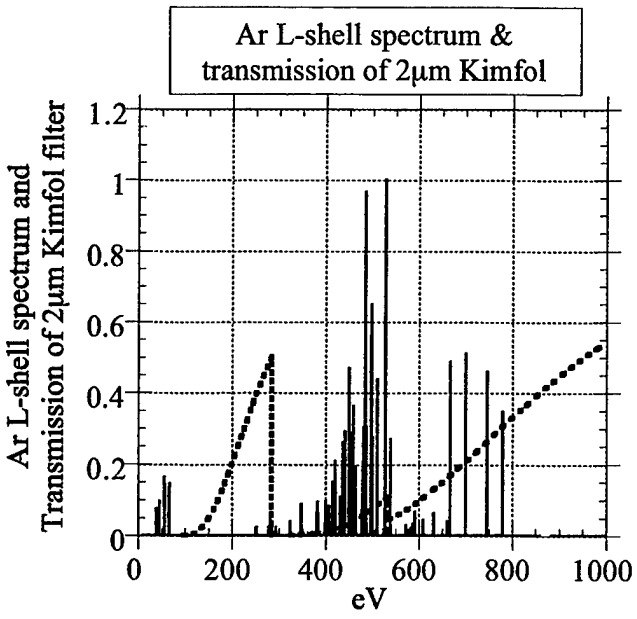

Figure 6-4. Ar L-shell spectrum and the transmission of 2 μm of aluminized Kimfol.

The spectrum of Ar L-shell radiation transmitted through the filter (2 μm thick aluminized Kimfol) is shown in Figure 6-5. The figure also shows the Kimfol transmission for reference. Note that all L-shell emissions above 100 eV are transmitted with varying attenuation.

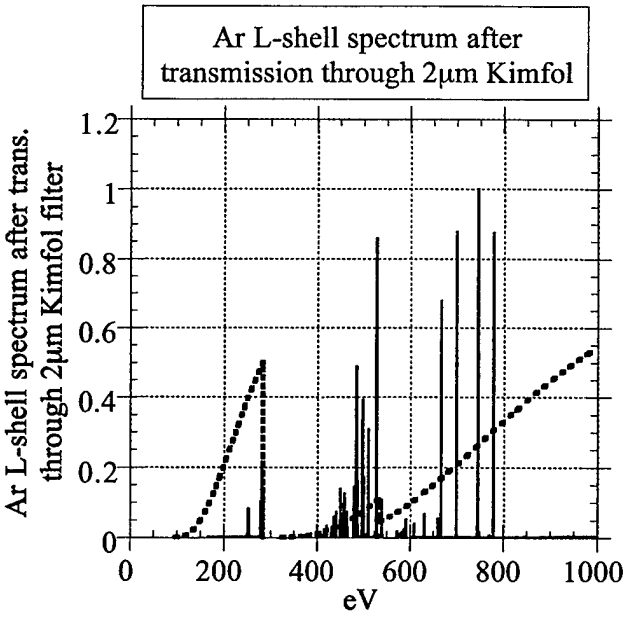

Figure 6-5. Ar L-shell spectrum as transmitted through the 2 μm Kimfol filter and the transmission of the Kimfol.

Figure 6-6 shows the integrated Ar L-shell spectrum. The top trace shows the spectrum incident on the filter. This is normalized to 100%. The figure also shows the integral of the spectrum transmitted through two aluminized Kimfol filters: 1 μm and 2 μm thick. 27% of the incident spectrum is transmitted through the 1 μm Kimfol, while 11% of the incident spectrum is transmitted through the 2 μm thick Kimfol. To this must be added the ≈100% of the K-shell spectrum that is transmitted by the filter. For a typical pinch that radiates ~10 kJ in the K-shell, the L-shell radiation is about 100 kJ. Thus ~10 kJ of this radiation is transmitted through the 2 μm Kimfol filter resulting in ~2 kJ of x-rays incident on the detector array. Therefore, the signals measured using the Kimfol filters should be about twice as large as those with the Kapton filter. This was indeed the case for this set of shots. Thus, images obtained using the 2 μm thick Kimfol filter are a good measure of the K+L shell emissions from the pinch.

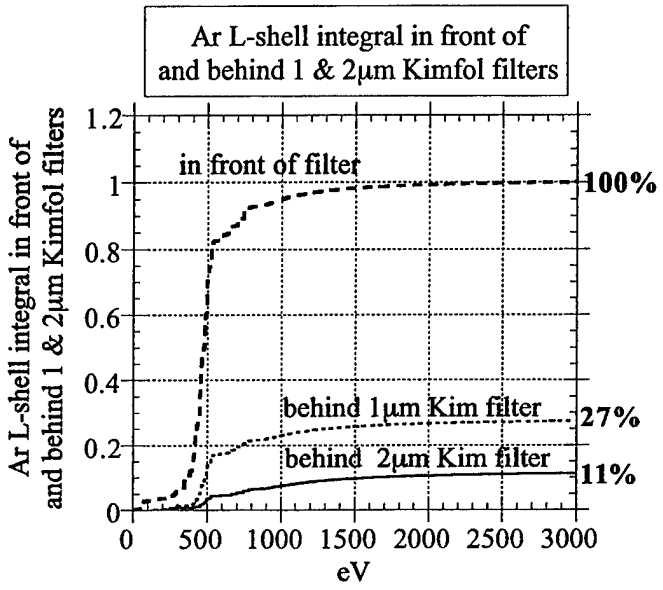

Figure 6-6. Integrated Ar L-shell spectrum in front of the Kimfol filters, behind 1 μm of Kimfol and behind 2 μm of Kimfol.

Figure 6-7 shows a sequence of four images from Shot 4067. The y-axis in the images shows the z distance as measured from the cathode. The radial extent of the pinch is shown along the x-axis. The axis of the pinch is at ≈4.5 mm. The entire sequence of 400 ps frames has been converted into a QuickTime movie and is available from the authors. The filter used to generate these images was 2 μm aluminized Kimfol. These are therefore, K+L shell images. A 0.5 mm diameter pinhole was used to image the pinch on the detector array with a 1:2.3 de-magnification. Since the beam lines are canted at 22° to the horizontal, the axial extent of the images as shown in the figure is larger than the radial extent. The field of view is thus 14.9 mm (axial) x 13.8 mm (radial) with a 2.3 mm resolution. The images are scaled to the peak intensity of all pixels during the shot. Ten levels are chosen for the contour plots at 10% increments. The noise to signal ratio is better than 1%. Therefore, the color purple, corresponding to signals from 1% to 9% in these images, represents real data.

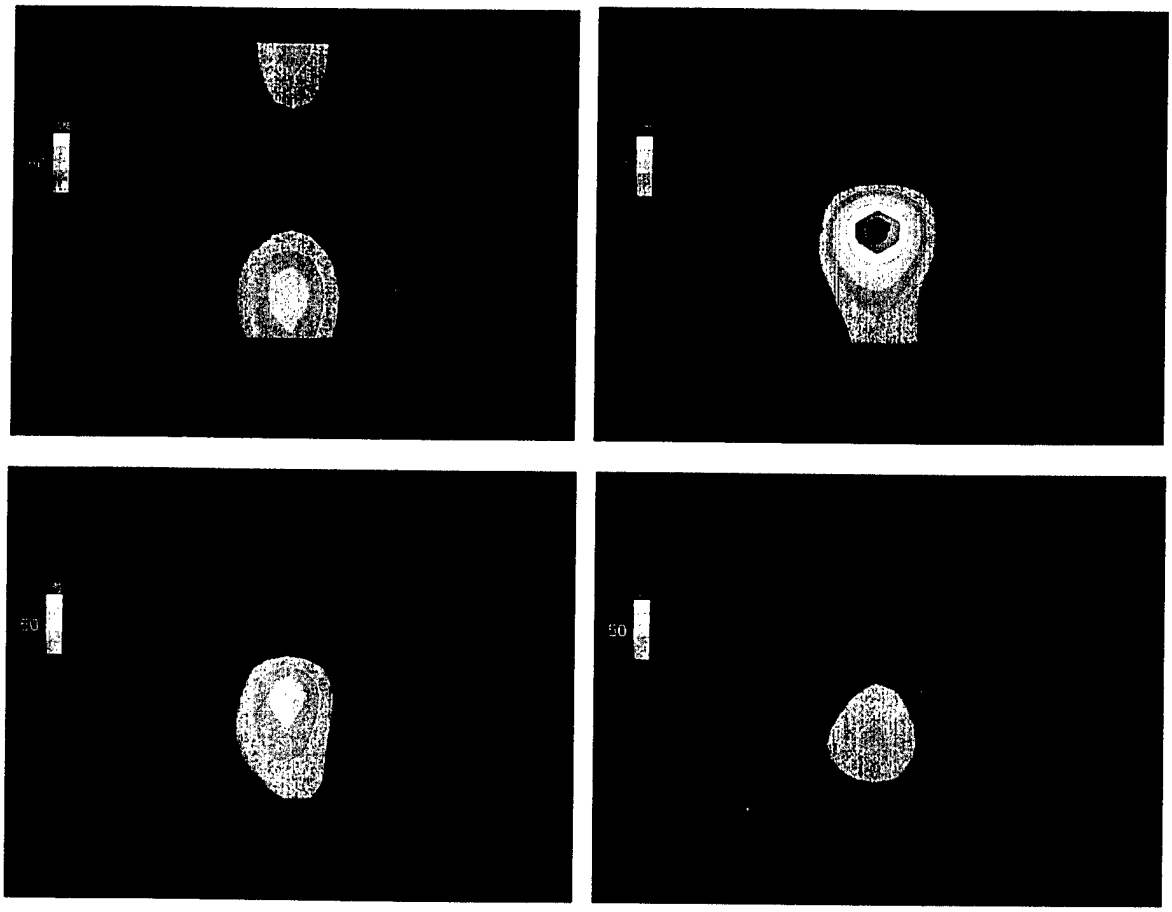

Figure 6-7. Sequence of K+L shell images from shot 4067.

In most shots similar to the one depicted in Figure 6-7, the emissions begin nearer the cathode and then the region nearer the anode lights up. The images acquired by the diamond camera can be integrated along the r direction to yield z vs. t graphs similar to those that are created by the MPI "zipper array" diagnostic. Figure 6-8 shows a comparison between the z vs. t graph created from the diamond camera data and the MPI zipper graph.

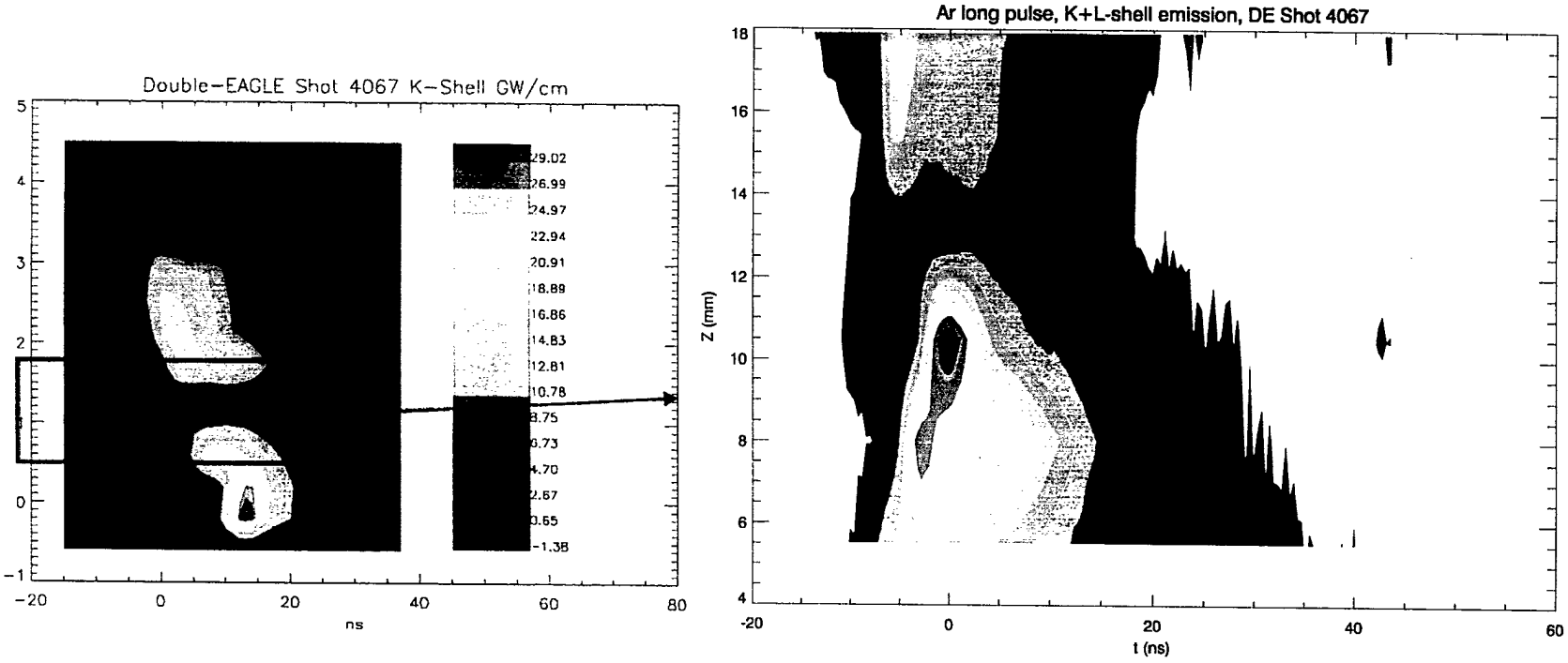

Figure 6-8. Comparison of the MPI "zipper array" image and the radially integrated z vs. t image obtained with the diamond camera. The MPI image is courtesy of Drs. J. Levine and J. Riordan of MPI.

By comparing the patterns in the two graphs, it can be seen that the AASC diamond camera is imaging the region of the pinch shown in the black rectangle in the MPI image on the left of the figure. While there is qualitative agreement between the two instruments the details of the two graphs are different. There are two main causes for these differences. The diamond camera images have a resolution of 2.3 mm for this shot, while the MPI "zipper array" has a resolution of about 4 mm. The diamond camera was filtered with 2 μm of Kimfol to image all the radiation from pinch above 100 eV. The MPI array was filtered with several layers of 0.001" Kapton to filter all but the hardest part of the K-shell spectrum of Ar. These differences in spectral content of the radiation captured by the two arrays could also explain the differences in images.

In summary, the diamond camera has been shown to image the z-pinch plasma with good spatial resolution. A comparison with the MPI "zipper array" shows that this camera also provides valuable zippering information, while also revealing radial information that a linear array such as the "zipper array" cannot access.

6.3 Temporal Resolution.

Figure 6-9 shows a sequence of four K+L shell images from another shot on Double-EAGLE. Evidence of spikes and bubbles in the luminosity of the pinch are evident. Again, a QuickTime movie has been created of all the 400 ps frames that may be obtained from the authors. As in the previous figures, the emissions begin near the cathode and then spread towards the anode.

Another important feature of these images is that the luminous regions appear to a series of smaller regions. This is to be contrasted with the single continuous regions that appear to be formed when looking at either time integrated or time resolved images (created with gated micro-channel plates). Since the brightly emitting regions appear to move up and down in the axial direction, a time-integrated image will wash out the motion and reveal only a continuous region of luminosity. Gated time resolved images have the problem that the dynamic range of the gated micro-channel plate (MCP) instruments is not large, leading to saturated images. Another problem is that in most gated MCP cameras the best time gate is 5 ns. Averaging over this duration also tends to wash out the images.

Figure 6-10 shows three frames acquired by the diamond camera on shot 4066 (the same shot displayed in Figure 6-9). If the first frame is timed to be at t = 0 ns, the second frame is at t = 800 ps and the third frame is at t = 2.8 ns. In the first frame, three regions of luminosity or bubbles are clearly seen. Just 800 ps later, the second bubble that was higher than and to the right of the lowest bubble in the first frame appears to have been swallowed up the lowest bubble, creating what looks like a spike. In the third frame, the spike appears to have shrunk back within the lowest bubble with a dramatic increase in intensity of the lowest bubble. Now a simulated frame captured using a 5 ns gate is created. This frame is created by adding the images captured in 12 successive frames acquired at 400 ps each. This simulated image, coincident in time with the images shown in Figure 6-10 is shown in Figure 6-11. There is no hint of the formation of the three bubbles, the spike and then the coalescing into two bubbles. All that is visible in this image is two bubbles. This is dramatic evidence of the utility of the diamond camera when comparing it to the gated MCP based time resolved cameras.

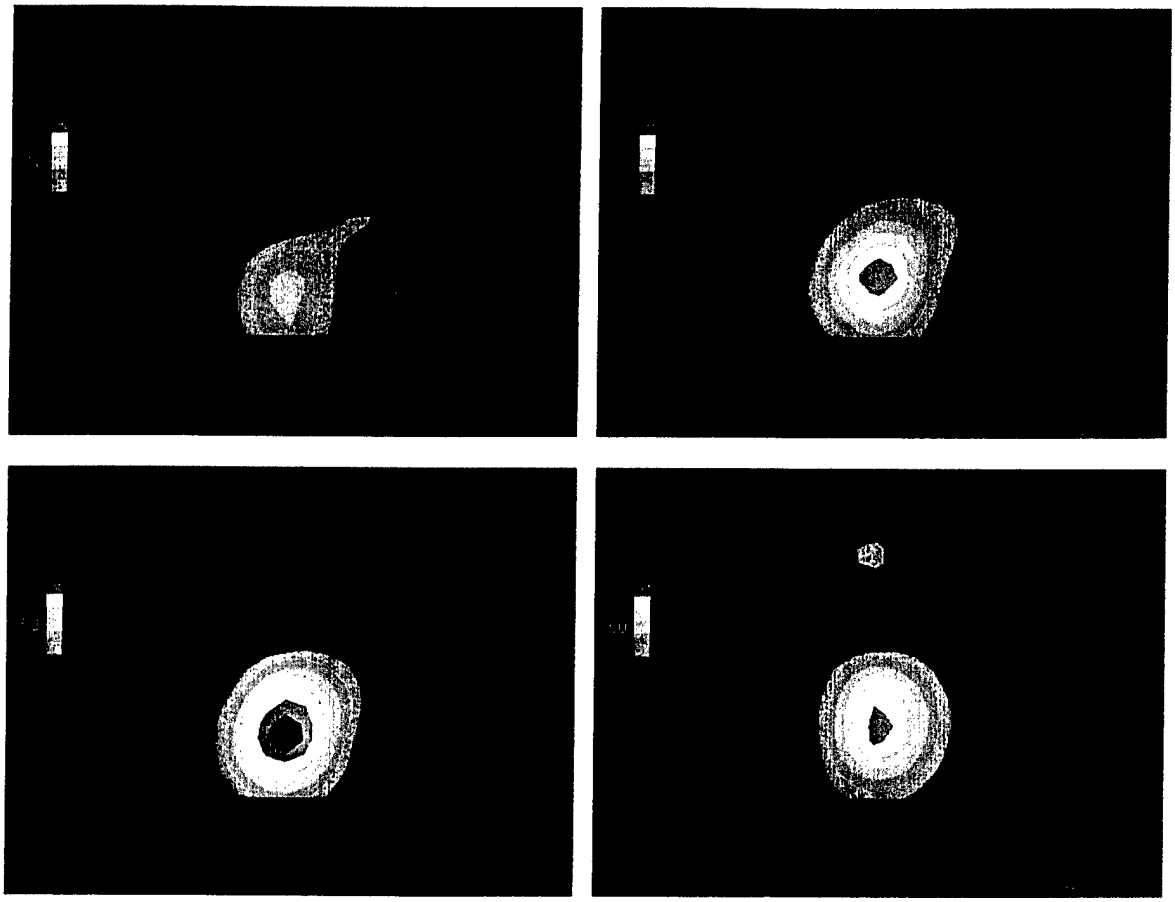

Figure 6-9. Sequence of four K+L shell images from shot 4066.

The 400 ps frame captured in this validation test is also not the limit of the camera. It has been shown that frames with 200 ps may be acquired during the calibration at Sandia National Laboratory. Even the 200 ps frame was a limit of the digitizer used in those tests. It may be possible to capture images with 100 ps temporal resolution with this camera, a feat no other instrument is capable of. This may be of vital importance in understanding the dynamics and stability of the implosions and for the design of higher power, higher fidelity and sources that are more efficient.

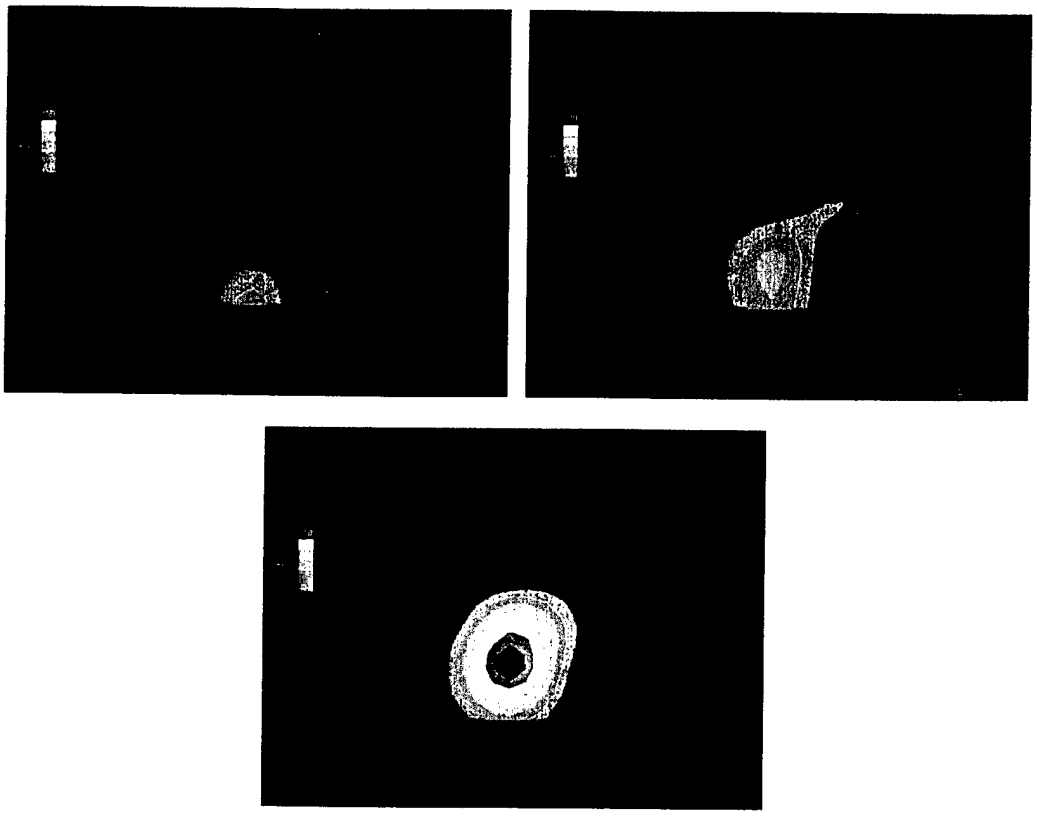

Figure 6-10. Three 400ps frames from shot 4066, separated by 0, 800 ps and 2.8 ns.

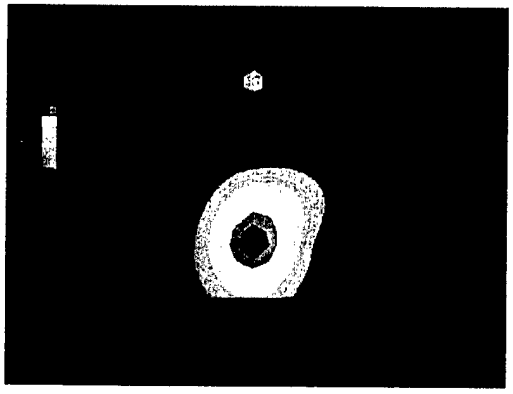

Figure 6-11. A composite 5 ns frame created from the 400 ps images acquired in shot 4066, incorporating the three frames showed in Figure 6-10.

6.4 Comparison of K-shell and K+L Shell Images.

K-shell images were acquired using the diamond camera filtered with 16.9 μm of aluminized Kapton. Figure 6-12 shows four images of the K-shell emitting regions of the Ar plasma in shot 4063. Qualitatively the images appear to be quite similar to those captured using the softer filter, thereby including the K and the L-shell emitting regions. As before, the region closer to the cathode starts emitting sooner than the region closer to the anode. There is also an appearance of radial motion of the emitting regions.

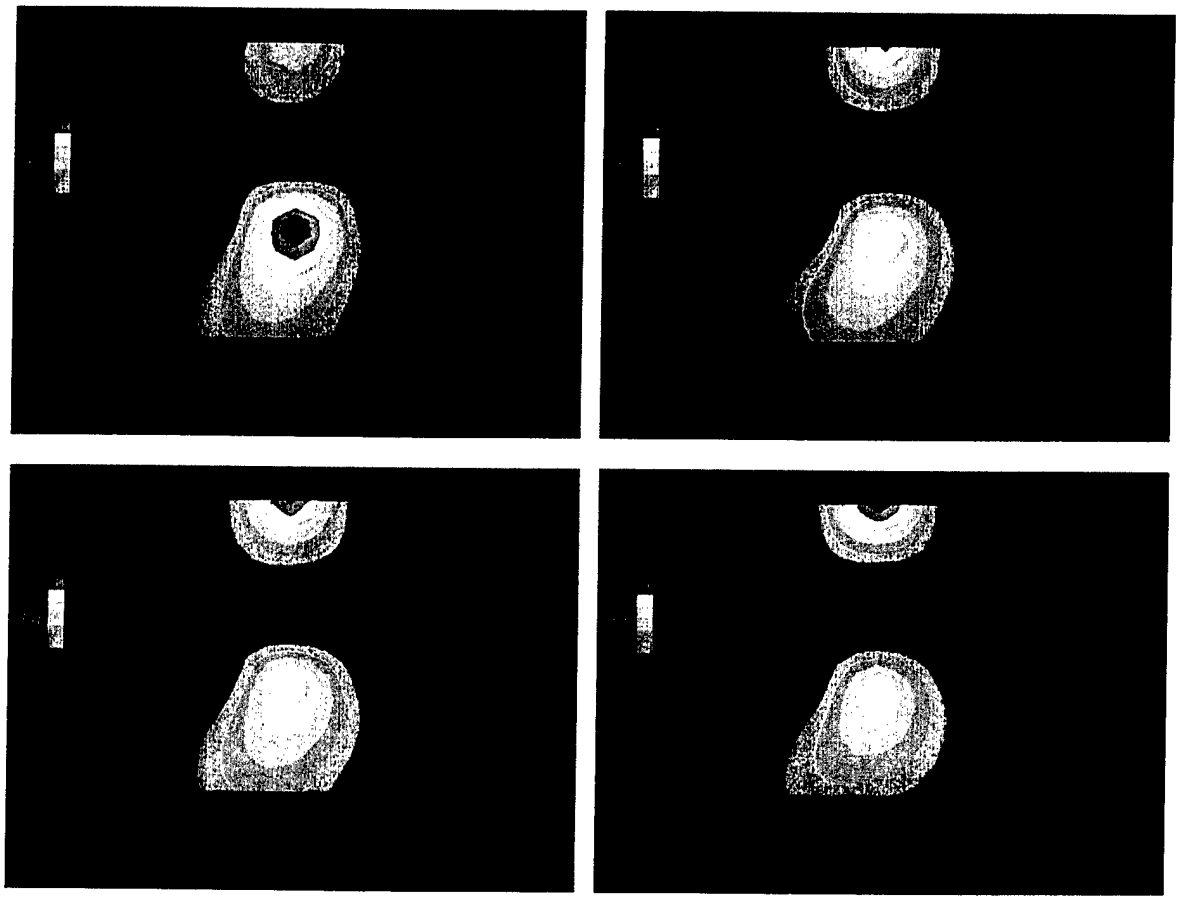

Figure 6-12. Sequence of four K-shell images from shot 4063.

While the images of the K-shell and the K+L shell emissions were not captured on a single shot, it is possible to compare them on different shots. In this particular set of shots, the pinch conditions were maintained constant because diagnostic development was the primary focus of the test series. Figure 6-13 shows the 400 ps frame at the peak of x-ray emissions from two shots of Double-EAGLE, one filtered for K+L shell (on the upper half) and the other of the K-shell (on the lower half).

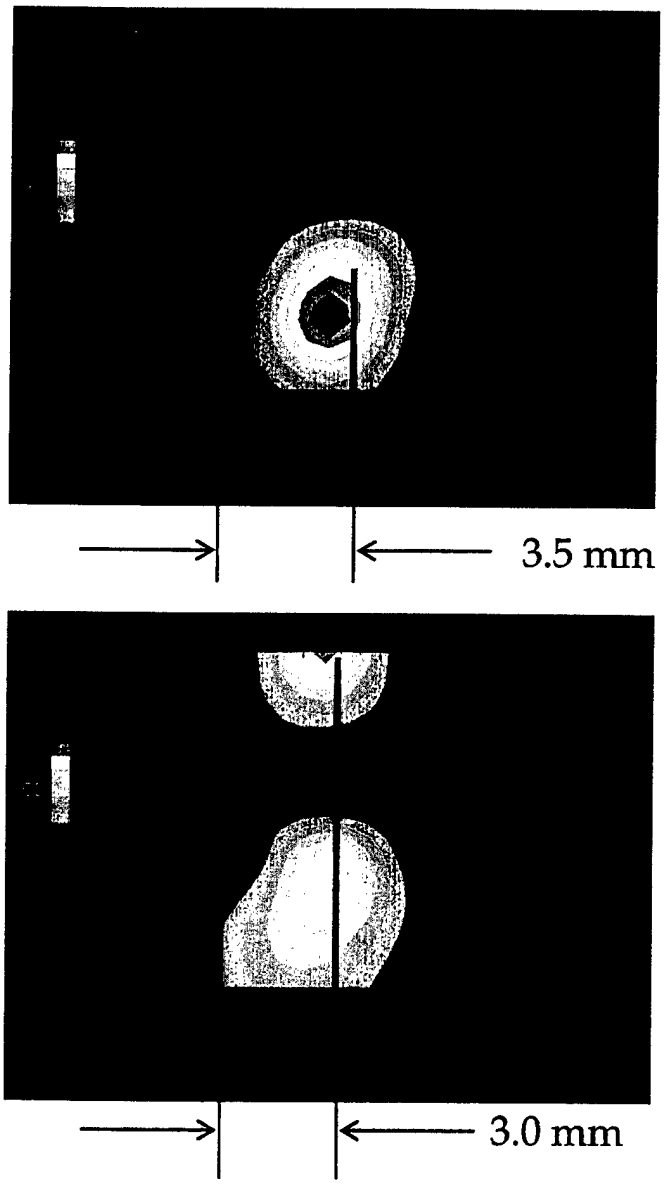

Figure 6-13. 400 ps frames at the peak of x-ray output from two shots. The frame on the upper half is a K+L image, the frame on the lower half a K-shell image.

The diameter of the K-shell emitting region is found to be about 3 mm and the diameter of the K+L shell region around 3.5 mm. Since the emitting region appears to be small bubbles, it is logical to stay that the ratio of the K-shell to K+L shell emission region is $(3.0/3.5)^3 \approx 60\%$. Apruzese has estimated that only 15% of the total mass is emitting K-shell radiation. This fact does not agree with the measured emission volumes. The explanation may lie in the fact that these images do not detect mass, but only luminous regions and that some of the mass may be emitting photons that are softer than 100 eV, the cut-off for the 2 μm Kimfol filter used here.

6.5 Effect of Magnification.

Images were acquired using two different magnifications. The previous sub-sections have presented data acquired with a 1:2.3 de-magnification. The camera was also configured to image the emissions from the pinch with a 1:1 magnification. With the 0.5 mm diameter pinhole, this translates to a 1 mm resolution in the z-pinch source. Figure 6-14 shows a four image sequence of K-shell emission from shot 4060 acquired with 1:1 magnification. A QuickTime movie of these images has also been made and is available from the authors.

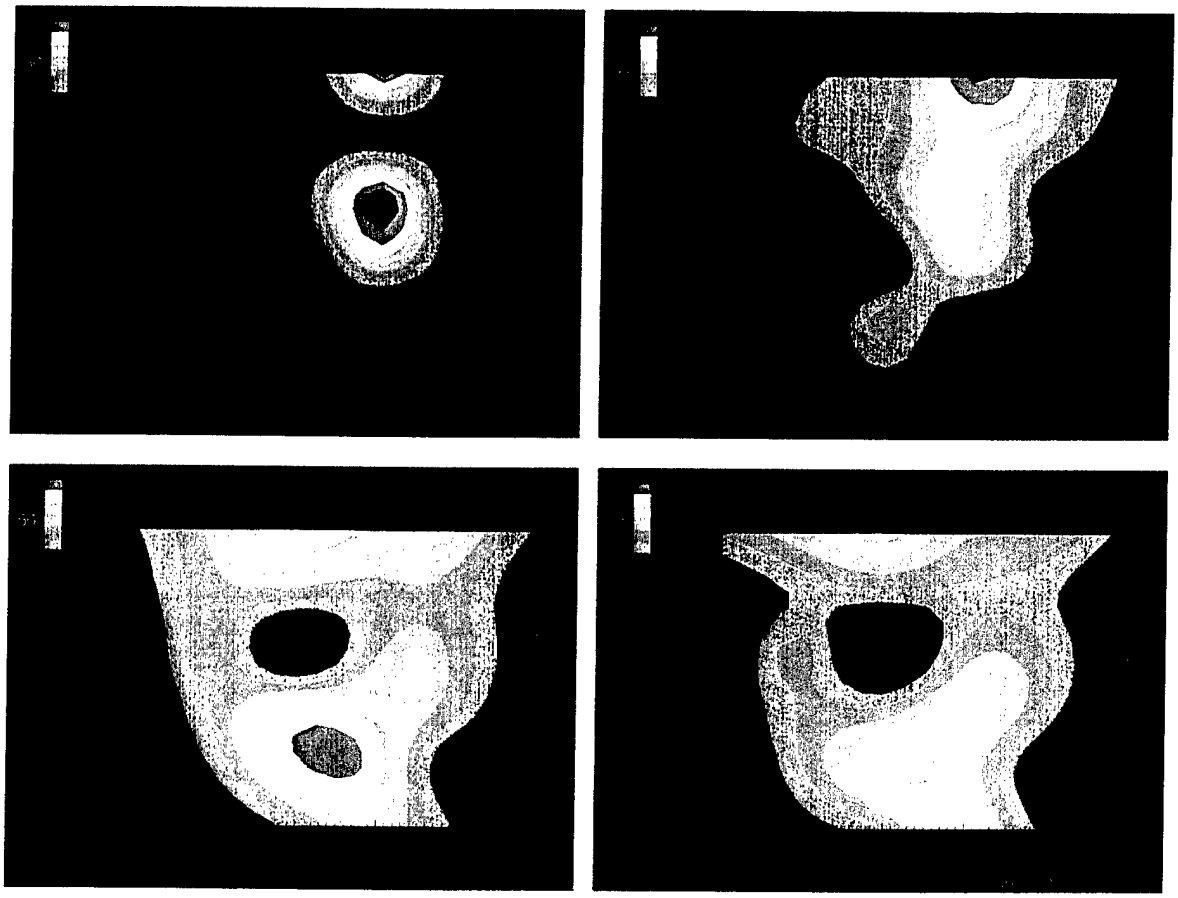

Figure 6-14. Sequence of four K-shell images from shot 4060, acquired with 1:1 magnification.

An interesting point to note in this set is that the emissions appear to start from a region closer to the anode. From this point on the familiar spikes, bubbles, winks on and off and radial and axial movement of the bubbles and spikes is evident. It is interesting to note that with the change in magnification the images appear to be more uniform than the images that have a larger spatial extent.

The increased magnification and resultant better spatial resolution allow us to determine the radial extent of the pinch better. Figure 6-15 shows two 400 ps frames at the peak of the x-ray output from two different shots. The camera was filtered in both shots to image the K-shell emissions. The vertical lines in both images represent the 3 mm diameter mark. It is clear that both images show that the size of the K-shell emitting region is about 3 mm in diameter.

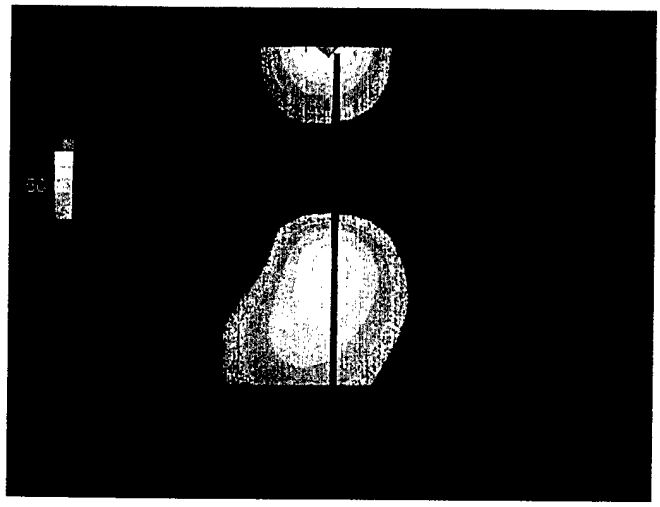

1:2.3 image

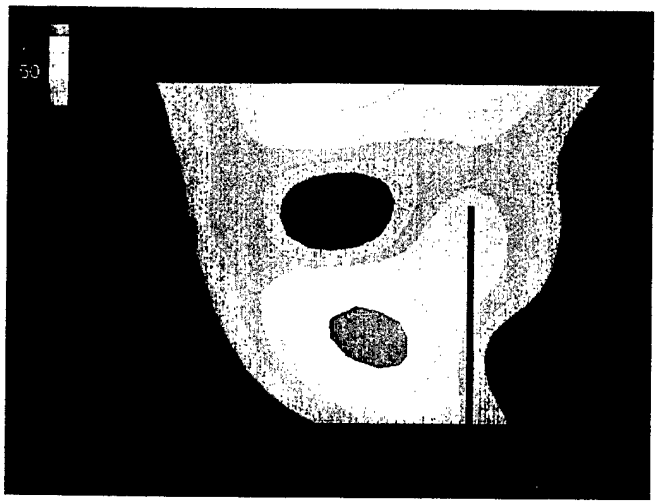

1:1 image

Figure 6-15. Comparison of two 400 ps at the peak of x-ray output. The image in the upper was acquired with 1:2.3 de-magnification, the image in the lower half with 1:1 magnification.

The diamond camera has been shown to be capable of producing images with 1:1 magnification to get good spatial resolution and with 1:2.3 de-magnification to get good spatial extent. It is possible to increase the magnification even further to image the plasma with 3:1 magnification and thus 0.3 mm spatial resolution. If the 12 pixel rows are aligned along the radius of the pinch then a 4 mm radial region could be images with 0.3 mm resolution. With the right digitizers 200 ps, temporal resolution can be achieved. This is would provide an insight into the dynamics of the pinch and the instability growth that has to date not been explored experimentally.

6.6 Cable Multiplexing.

One drawback that has been pointed out of this diamond camera is that it requires 72 channels of fast digitizers to capture data from the 72 pixel camera. Should the number of pixels be increased to make the camera even more versatile, this problem would get worse. There is, however, a bright spot in this scenario of gloom. The x-ray emissions from the z-pinch source last for about 30 ns. Most fast digitizers provide at least 10,000 point records, frequently higher. Digitizing at the rate of 200 ps/sample this translates to a 2 μs record length. If the signal from individual detectors could be delayed with respect to other pixels then they may be multiplexed to take advantage of the long record length provided by the digitizers and reduce the number of channels required. For example if four channels were delayed ≈80 ns with respect to each other the number of digitizer channels required for the 72 pixel camera would be reduced to 18!

To this end, an experiment was conducted during the validation tests to prove feasibility. A length of LMR-400 cable (0.5" diameter) was used to provide a 120 ns delay between two pixels. The signal from one of the pixels of the camera was connected to a power tee. One of the two outputs of the power tee was connected to the digitizer to provide a measure of the raw signal from the digitizer. The other end of the power tee was connected to the delay cable and then added to the primary signal itself. The data from one shot of this test are shown in Figure 6-16. The primary signal is shown in black. The delayed signal, added to the primary signal is shown in red. It was found that there was no temporal degradation of the pulse. The magnitude of the signal dropped to about 85% of its original value, a factor that can be corrected by simple arithmetic manipulation of the data. The attenuation will be lower for ≈80 ns delays. The use of four such delays in sequence should not be a problem. The cost of such a delay line multiplexer will not be prohibitive either. A rough order of magnitude estimate suggests that it might cost as little as ≈$15k.

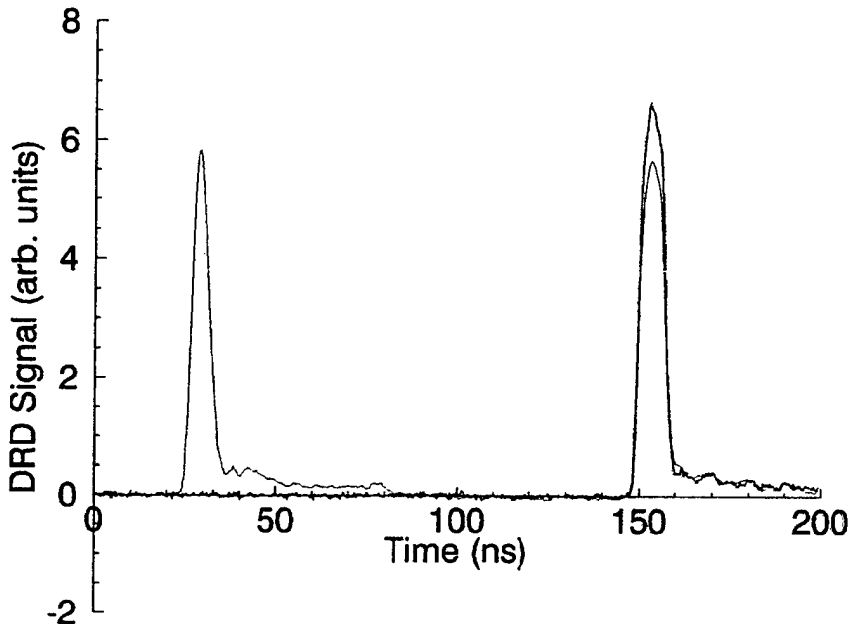

Figure 6-16. Temporal trace of a single pixel from the diamond camera (black) superimposed on a multiplexed trace (red) consisting of the original trace (left peak) and a ≈120 ns delayed version of the trace (right peak).

Section 7

Conclusion

The diamond camera has been successfully designed, fabricated, calibrated and validated on a test sequence on Double-EAGLE. The original RFP had called for a spatial resolution of 1 mm and a temporal resolution of 1 ns. The instrument was to have been capable of providing some spectral resolution, by imaging both the x-rays and extreme UV. All the goals for this RFP have been met or exceeded.

The camera provides spatial resolution better than 1 mm. The temporal resolution is better than 400 ps. Both EUV and soft x-ray emissions from an Ar pinch have been imaged.

At the end of the program the diamond camera was taken back to Sandia National Laboratory to re-calibrate the individual pixels to determine the change in sensitivity, if any, due to pixel aging. The details of these measurements are in the next sub-section. This report concludes with a discussion of some future experiments with the diamond camera.

7.1 Second Calibration at SNL.

The diamond camera was shipped to SNL to re-calibrated in June 1999. However, the crate containing the camera was dropped by FedEx (the carrier chosen for the shipment). This resulted in damage to the camera. The last section of the camera containing the diamond detectors broke free of the connector plate. This caused several of the detector cables to snap and some diamonds to be disconnected from the shims and cables. A total of 19 detectors was left with no contact to the external circuit. Other diamonds in the array were raised, lowered or bent relative to their original position. Figures 7-1 and 7-2 show the camera after the shipping damage. FedEx has denied responsibility for the damage. Given that shipping/receiving at SNL was also involved in handling the crate before AASC inspected it for damage, there is potential for ambiguity as to the responsible party. AASC continues to press the claim with FedEx, but it does not appear hopeful .

At SNL, emergency repairs were conducted on the camera to rearrange all the pixels to re-create the diamond array. Then the pixels were calibrated for a second time. In addition, the five AASC standard diamond radiation detectors (DRD) were calibrated again. These detectors had not been used in the year between the two trips to Sandia. Figure 7-3 shows the new sensitivity of these detectors and the old calibration. The data points represent the average sensitivity determined from several shots. The error bars on the measurements represent the standard deviation. It is seen that the detector calibration is stable over the duration of one year.

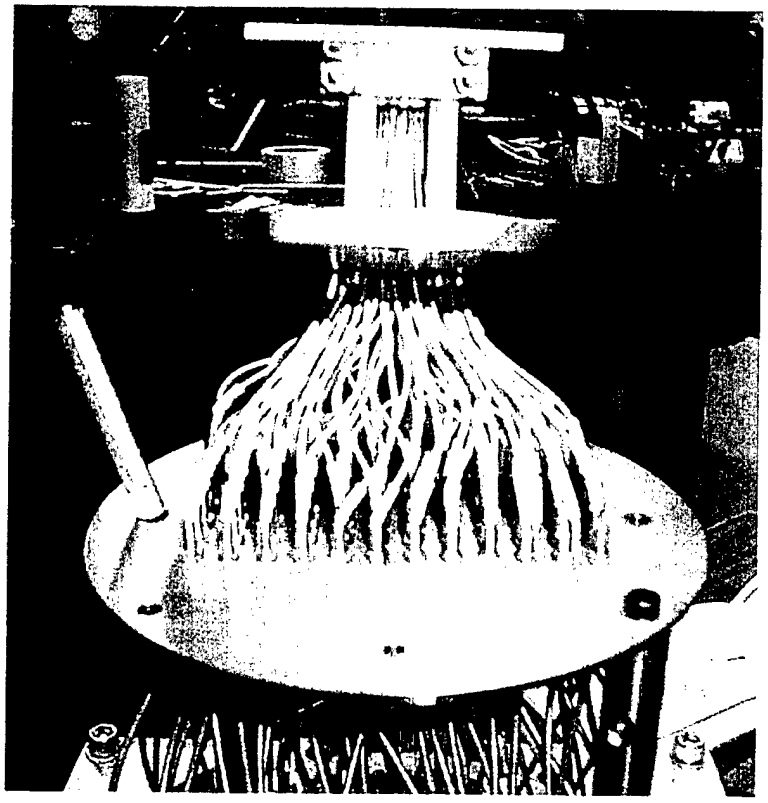

Figure 7-1. Photograph showing shipping damage to the diamond camera.

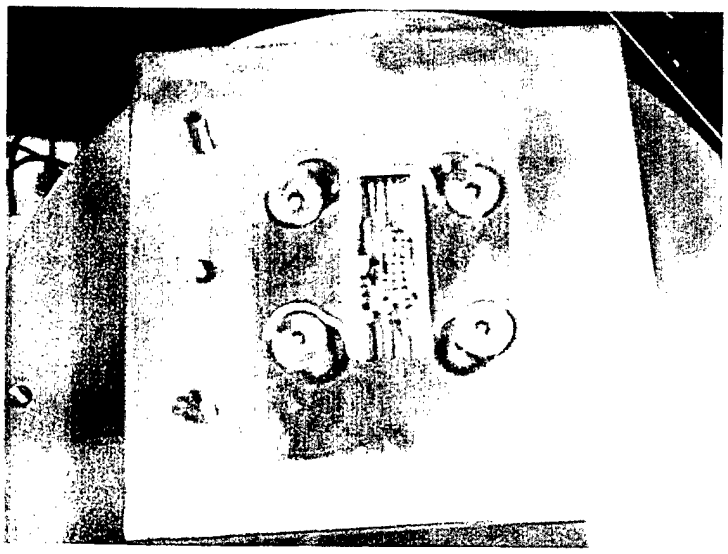

Figure 7-2. Photograph showing damage to the detector array face.

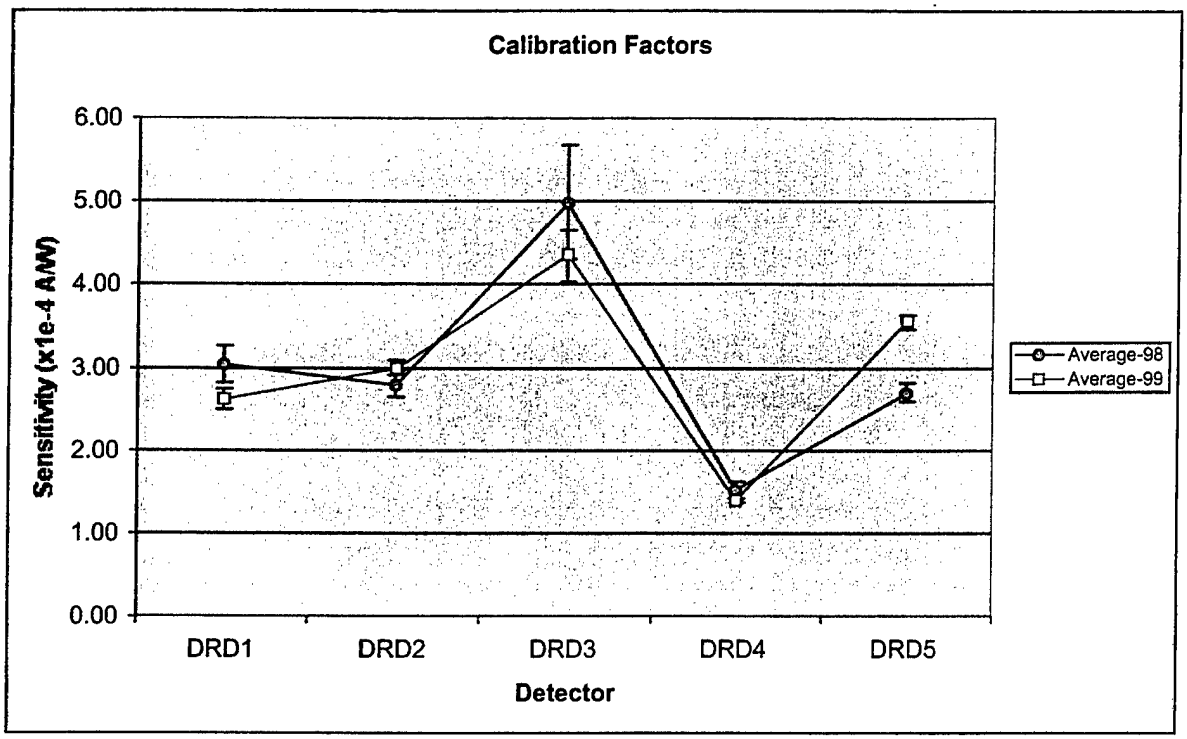

Figure 7-3. Comparison of the sensitivity of five AASC diamond radiation detectors measured in September 1998 and in June 1999.

In addition to the new calibration of the diamond detectors, the temporal response of the diamond detectors was measured with greater accuracy. Sandia National Laboratory has just acquired 3 GHz, 10 Gsample/sec digitizers from Tektronix. Digitizing at 100 ps/sample provides a better measure of the temporal resolution possible with diamond detectors. Figure 7-4 shows two DRD traces. The upper trace is from the 1999 calibration acquired at 100 ps/sample. The lower trace is from the 1998 calibration acquired at 200 ps/sample. A quick glance shows that the 200 ps/sample digitizer is not accurate at finding the peak of the DRD signal. Since the rise time of the x-ray pulse from the laser plasma source is less than 1 ns, digitizing at 200 ps/sample provides less than 5 points to determine the rise time. The peak is hard to detect due to its sharpness. However, digitizing at 100 ps/sample clearly reveals the peak, resolves the rise time using 10 points and clearly shows the x-ray pulse decay. This test also demonstrates that the diamond detectors are capable of 100 ps resolution. Since the diamond camera consists of an array of similar detectors, it can be argued that the diamond camera also has a 100 ps temporal resolution.

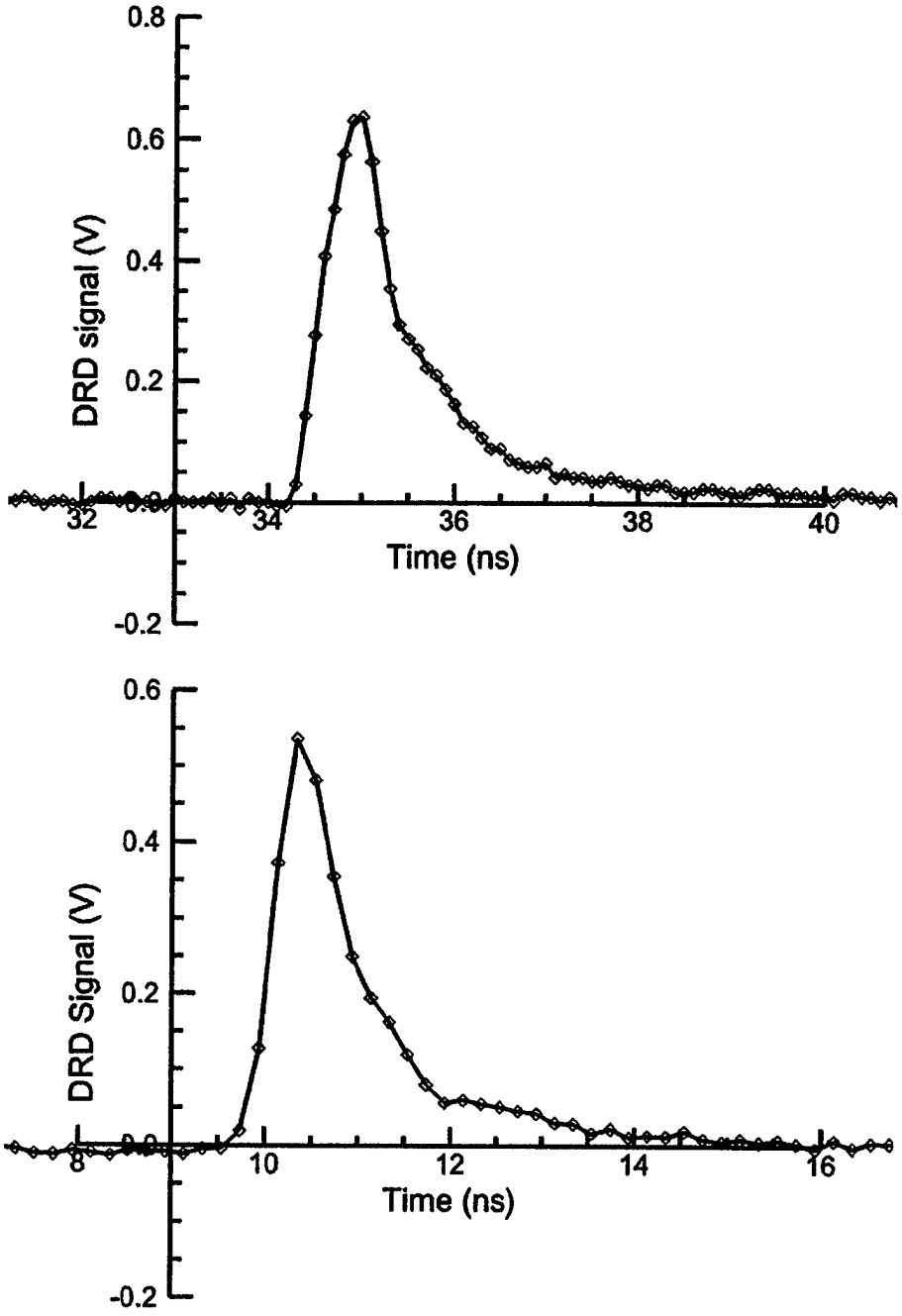

Figure 7-4. X-ray output from the laser plasma calibration source as measured by a DRD. The upper trace was acquired in 1998 at 200 ps/sample. The lower trace was acquired in 1999 at 100 ps/sample.

The diamond camera was also calibrated again, despite the fact that it was damaged in shipment. The calibration was performed to determine if such damage would change the calibration of at least those pixels that had survived. A similar procedure to that described in section 5 was used to calibrate the detectors. Figures 7-5, 7-6 and 7-7 show the results of this calibration (red data points and trace). The traces are drawn only to aid the eye in identifying pixels. The calibration performed in 1998 is also shown in the figures in blue. The average sensitivities determined over several shots are shown as the data points. The error bars shown in both cases represent the standard deviation of the measurement.

Nineteen detectors are not connected to the external circuit due to cable damage or the diamond coming unsoldered from the shim connecting it to the cables. Of the remaining number 35 pixels have a sensitivity that is less than 30% different from the previous calibration. The others have sensitivities that are more disparate. There is one very good reason why the calibration factors of the diamond camera have changed far more than that of the diamond detectors. The damage to the camera has resulted in a changed location of the detectors with respect to each other. Some of the detectors may be shadowing others in the new configuration and may be located such that the scattered radiation from one detector may be irradiating another, increasing the sensitivity of some of the detectors. In addition, the stress of the motion of individual detectors with respect to its nearest neighbors could have caused a change in the Ohmic contact between the detector element and the external circuit. This changes the sensitivity of the detector.

It is hoped that the diamond camera will be repaired and restored to its original condition. With this is mind the final section of this report provides some suggestions for future work with the camera.

7.2 Future Work.

The diamond camera was validated on Double-EAGLE using only half of the 6x12 array, due to a limitation in the number of cable feedthroughs available in the user screen room. Using the entire array to image the pinch at a 1:2.3 de-magnification will provide a 30 mm axial field of view, covering the entire pinch. This will provide valuable information about the nature of the spikes and bubbles that were apparent even in the restricted view of the validation tests.

The typical z-pinch is about 30 mm long with a 3 mm diameter. The 6x12 aspect ratio of the camera may be best used by aligning the 6 columns along the radial direction. Using a pair of spatially separated crossed slits, different magnifications for the radial and axial dimensions may be achieved. For example, the radial direction might be resolved with 1:1 magnification, while the axial direction might be resolved with 1:2.5 de-magnification to cover the entire pinch.

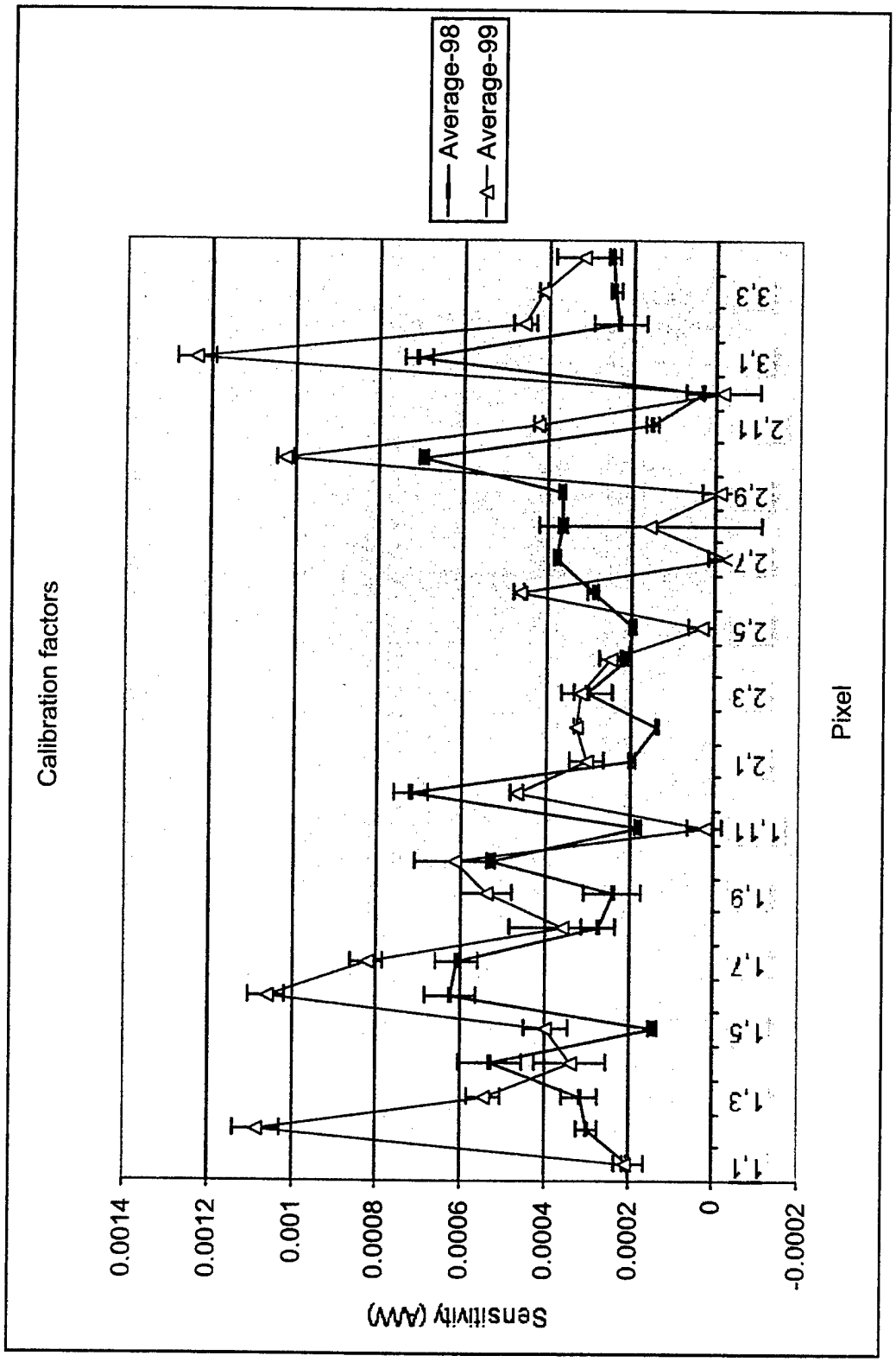

Figure 7-5. Calibration factors for pixels 1,1 through 3,4.

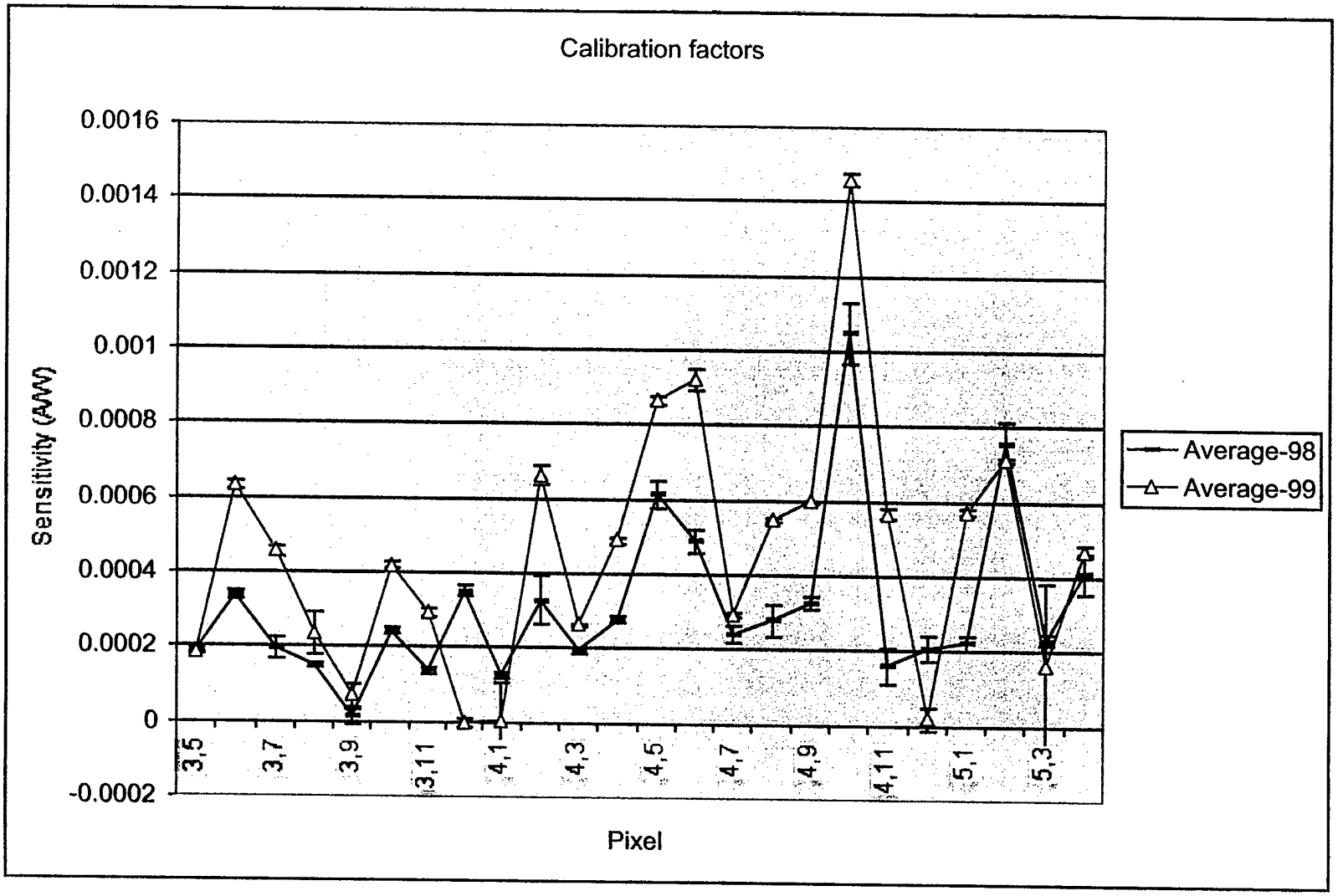

Figure 7-6. Calibration factors for pixels 3,5 through 5,4.

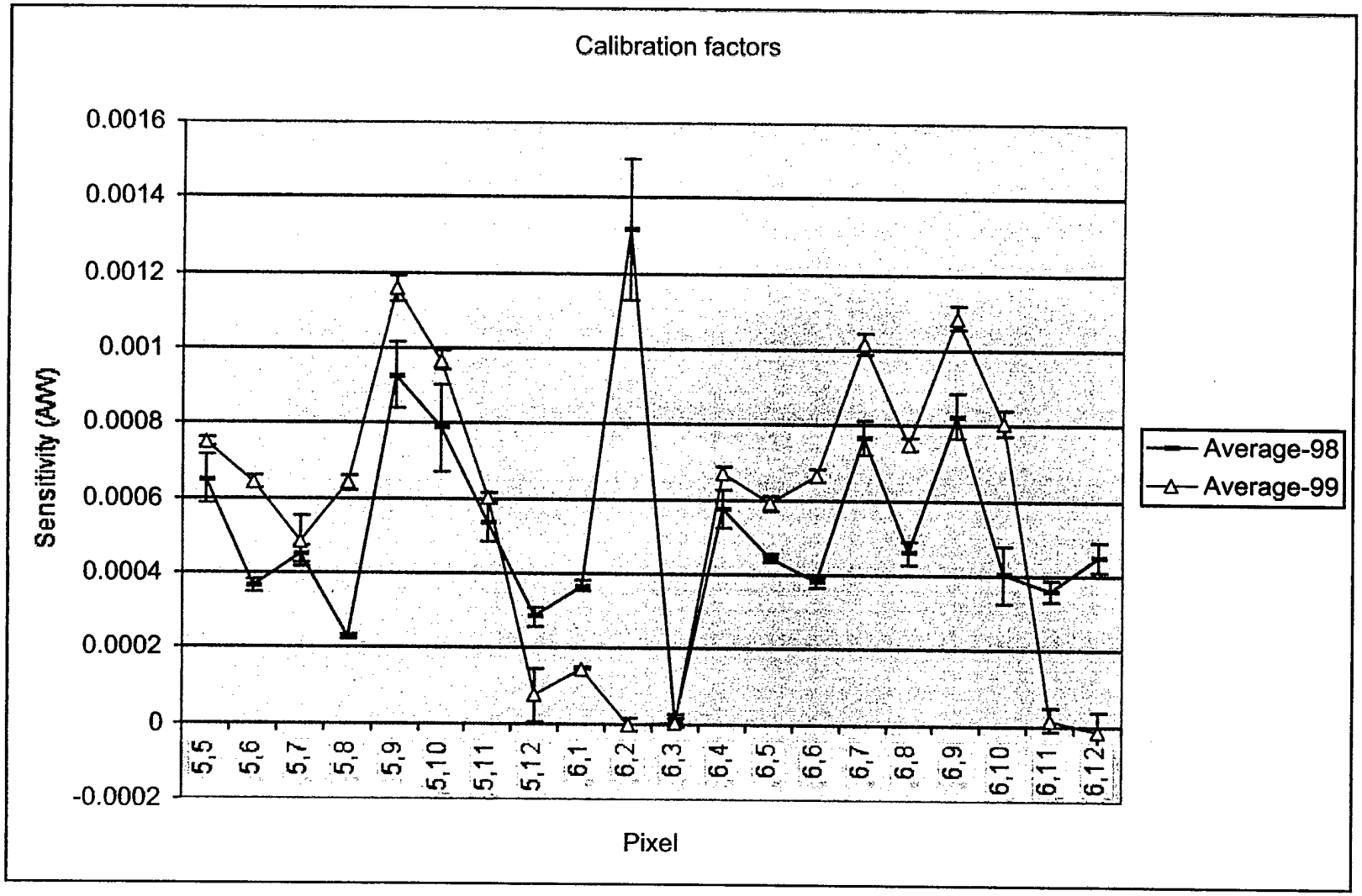

Figure 7-7. Calibration factors for pixels 5,5 through 6,12.

The same theme might be expanded further as shown in Figure 7-8. A pair of crossed slits may be used to image the pinch. In this case, a 1:1 magnification would be used in the radial direction. A 1:5 de-magnification would be used in the axial direction to image the entire pinch and the two slits would allow simultaneous measurement of the K-shell *and* K+L shell emissions from the pinch. In this configuration, the two images may be digitally subtracted to determine the regions of the pinch that emit L-shell radiation. This will provide information on the initial phase (radial run-in) of the pinch and shed light on the development of instabilities. Further, when the size of the K-shell image grows to within 50-75% of the K+L shell volume, the implosion would be optimized. When the implosion is far from optimum for K-shell emission, typically <30% of the volume might emit in the K-shell.

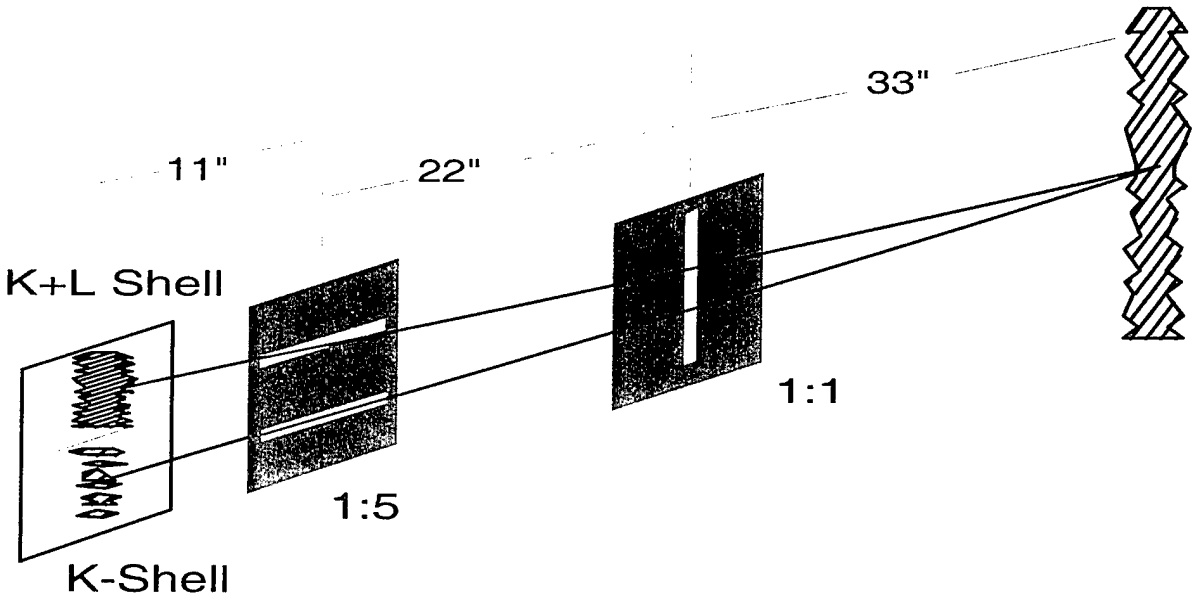

Figure 7-8. Suggested configuration of double slits to image both the K and K+L shell emissions on a single shot.

An upgrade of the camera to 6x16 pixels will prove to be a valuable addition to the camera's capabilities. In this case, the configuration showed in Figure 7-8 may be modified to use only 1:3.5 de-magnification to image the entire pinch and capture simultaneously the K and K+L shell emissions from the pinch. The cable delay multiplexer (4 pixels multiplexed into a single digitizer channel) described earlier will be an invaluable addition, reducing the number of digitizer channels required for the 6x16 camera from 96 to 24.

Section 8

References

Gudden, V.B. and Pohl, R., ZEITSCHRIFT FUR PHYSIK, Vol. 17, 170, 1923. (UNCLASSIFIED)

Kania, D.R., Landstrass, M.I., Plano, M.A., Pan, L.S., and Han, S., DIAMOND AND RELATED MATERIALS, Vol., 2, 1012, 1993. (UNCLASSIFIED)

Krishnan, M., Prasad, R.R., Qi, N., Gurtman, G., Rice, M., Murphy, H., Steen, P., and Parks, D., "IMPROVE X-RAY YIELD, SPECTRAL FIDELITY AND PERFORMANCE OF PHOENIX PRS: FINAL REPORT," Report No. aasc96TM-37, 1996. Available from Dr. M. Krishnan at (510) 483-4156 x 202. (UNCLASSIFIED)

Pan, L.S., Han, S., Kania, D.R., et al., JOURNAL OF APPLIED PHYSICS, Vol. 74 (2), 1086, 1993. (UNCLASSIFIED)

Pan, L.S., Han, S., Kania, D.R., Plano, M.A., and Landstrass, M.I., DIAMOND AND RELATED MATERIALS, Vol. 2, 820, 1993. (UNCLASSIFIED)

Pan, L. S. and Kania, D.R., DIAMOND: ELECTRONIC PROPERTIES AND APPLICATIONS, Kluwer Academic Publishers, Boston - Dordrecht - London, 1993. (UNCLASSIFIED)

Prasad, Rahul R., Tzonev, Ivon V., Peterson, Gus G., Gensler, Steve, and Krishnan, Mahadevan, "RADIATION IMAGING DIAGNOSTIC FOR PLASMA RADIATION SOURCES", Annual Progress Report for contract DSWA01-96-C-0171, Report No. aasc97TM-49, 1997. Available from Dr. Prasad at (510) 483-4156 x 204 or prasad@aasc.net. (UNCLASSIFIED)

Spielman, R.B., REVIEW OF SCIENTIFIC INSTRUMENTS, Vol. 63, 5056, 1992. (UNCLASSIFIED)

Spielman, R.B., Hsing, W.H., and Hanson, D.L., REVIEW OF SCIENTIFIC INSTRUMENTS, Vol. 59 (8), 1804, 1988. (UNCLASSIFIED)

DISTRIBUTION LIST

DTRA-TR-99-42

DEPARTMENT OF DEFENSE

DEFENSE ADVANCED RESEARCH
PROJECTS AGENCY (DARPA)
3701 NORTH FAIRFAX DRIVE
ARLINGTON, VA 22203-1714
ATTN: DED
ATTN: MTO/J. ZOLPER
ATTN: SP/M. OBLE

DEFENSE THREAT REDUCTION AGENCY (DTRA)
ALBUQUERQUE OPERATIONS
1680 TEXAS STREET SE
KIRTLAND AFB, NM 87117-5669
ATTN: TDTD/G. LU
ATTN: TDTDN/D. BALL

DOD MISSILE DEFENSE AGENCY
JOINT PROGRAM OFFICE (NMD-JPO)
1725 JEFFERSON DAVIS HIGHWAY, SUITE 12021
ARLINGTON, VA 22202-4102
ATTN: E. HUDAK

DEFENSE TECHNICAL INFORMATION CENTER
8725 JOHN J. KINGMAN ROAD, SUITE 0944
FORT BELVOIR, VA 22060-6218
ATTN: DTIC

DEPARTMENT OF THE ARMY

US ARMY NUCLEAR AND CHEMICAL AGENCY
7150 HEELER LOOP, SUITE 101
SPRINGFIELD, VA 22150-3198
ATTN: ATNA-ZA/C. DAVIDSON
ATTN: AD LIBRARY

ARMY SPACE AND MISSILE
DEFENSE TECHNICAL CENTER (SMDTC)
P.O. BOX 1500
HUNTSVILLE, AL 35807
ATTN: SMDC-TC-WV/P. SIMPSON

DEFENSE THREAT REDUCTION AGENCY (DTRA)
8725 JOHN J. KINGMAN ROAD, MSC-6201
FT. BELVOIR, VA 22060-6201
ATTN: TD/D. LINGER
ATTN: TDN/COL. D. DEFOREST
ATTN: TDNS/L. PRESSLEY
ATTN: TDNS/LTC B. BREDEHOFT
ATTN: TDNS/R. DAVIS 5 CYS

DOD MISSILE DEFENSE AGENCY
7100 DEFENSE PENTAGON
WASHINGTON, DC 20301-7100
ATTN: ST/C. INFOSINO
ATTN: TER/J. MCCOMB

DOD MISSILE DEFENSE AGENCY
JOINT PROGRAM OFFICE (JPO)
P.O. BOX 1500
HUNTSVILLE, AL 35807-3801
ATTN: JNI-EH/D. PIERCE

ARMY RESEARCH LABORATORIES
2800 POWDER MILL ROAD
ADELPHI, MD 20783-1197
ATTN: AMSRD-ARL-SE/J. PELLEGRINO
ATTN: AMSRD-ARL-SE-DP/S. SCOZZIE

ARMY TEST AND EVALUATION COMMAND
4501 FORD AVENUE
ALEXANDRIA, VA 22302
ATTN: TECHNICAL DIRECTOR/B. BARR

WHITE SANDS MISSILE RANGE
DEPARTMENT OF THE ARMY
NUCLEAR EFFECTS DIVISION
WHITE SANDS, NM 88002-5176
ATTN: STEWS-NE/J. MEASON

DISTRIBUTION LIST

DTRA-TR-99-42

DEPARTMENT OF THE NAVY

NAVAL RESEARCH LABORATORY
4555 OVERLOOK AVENUE, SW
WASHINGTON, D.C. 20375-5000
ATTN: CODE 6700/S. OSSAKOW
ATTN: CODE 6720/J. DAVIS
ATTN: CODE 6720/W. THORNHILL
ATTN: CODE 6720/J. APRUZESE
ATTN: CODE 6770/G. COOPERSTEIN
ATTN: CODE 6770/R. COMMISSO
ATTN: CODE 6370/G. HUBLER

NAVAL SURFACE WARFARE CENTER
DAHLGREN DIVISION
11720 DAHLGREN ROAD
DAHLGREN, VA 22448-5100
ATTN: CODE G23/J. PARTAK
ATTN: TECHNICAL LIBRARY

NAVY STRATEGIC SYSTEMS PROGRAMS
REENTRY SYSTEMS BRANCH
NEBRASKA AVENUE COMPLEX
287 SOMERS COURT, NW
WASHINGTON, DC 20393-5446
ATTN: SP28/B. HANNA

NAVAL SURFACE WARFARE CENTER
CARDEROCK DIVISION
9500 MACARTHUR BOULEVARD
WEST BETHESDA, MD 20817-5700
ATTN: CODE 682/R. STARK - 227-5668

DEPARTMENT OF ENERGY

UNIVERSITY OF CALIFORNIA
LAWRENCE LIVERMORE NATIONAL LABORATORY
P.O. BOX 808
LIVERMORE, CA 94551-9900
ATTN: REPORTS LIBRARY

LOS ALAMOS NATIONAL LABORATORY
P.O. BOX 1663
LOS ALAMOS, CA 87545
ATTN: REPORTS LIBRARY

SANDIA NATIONAL LABORATORIES
ATTN: MAIL SERVICES
P.O. BOX 5800
ALBUQUERQUE, NM 87185-0459
ATTN: C. DEENEY, MS 1194
ATTN: C. COVERDALE, MS 1159
ATTN: M. HEDEMANN, MS 1159
ATTN: D. MCDANIEL, MS 1194

DEPARTMENT OF THE AIR FORCE

AIR FORCE OPERATIONAL
TEST AND EVALUATION CENTER
8500 GIBSON BOULEVARD, SE
ALBUQUERQUE, NM 87117
ATTN: AFOTEC CN/M. WILLIAMS

AIR FORCE RESEARCH LABORATORY
3550 ABERDEEN AVENUE, SE
KIRTLAND AFB, NM 87117-5776
ATTN: DEHP/J. DEEGAN
ATTN: DEHP/G. KIUTTU

AF SPACE AND MISSILE CENTER
2420 VELA WAY
SUITE 1467/A8
EL SEGUNDO, CA 90245-4687
ATTN: SMC/XR/COL W. GARDNER

ARNOLD ENGINEERING DEVELOPMENT CENTER
100 KINDEL DRIVE, SUITE A327
ARNOLD AFB, TN 37389-1327
ATTN: AEDC/CD/A. GOLDSTAYN

ARNOLD ENGINEERING DEVELOPMENT CENTER
1099 AVENUE C, SUITE 106R
ARNOLD AFB, TN 37389-9010
ATTN: AEDC/DO/R. POLCE

ARNOLD ENGINEERING DEVELOPMENT CENTER
1088 AVENUE C
ARNOLD AFB, TN 37389-6700
ATTN: AEDC/DOS/CAPT E. BONNER
ATTN: AEDC/DOS/LT. N. TRACEY

DISTRIBUTION LIST

DTRA-TR-99-42

DEPARTMENT OF DEFENSE CONTRACTORS

ALAMEDA APPLIED SCIENCES CORPORATION
2235 POLVOROSA AVENUE, SUITE 230
SAN LEANDRO, CA 94577
ATTN: M. KRISHNAN
ATTN: P. COLEMAN
ATTN: J. TOMPSON

ALME AND ASSOCIATES
6020 SOUTH RICHMOND HWY #204
ALEXANDRIA, VA 22303
ATTN: J. DAVIS
ATTN: S. SEILER

HY-TECH RESEARCH CORPORATION
104 CENTRE COURT
RADFORD INDUSTRIAL CENTER
RADFORD, VA 24141
ATTN: E. YADLOWSKY
ATTN: R. HAZELTON
ATTN: J. MOSCHELLA

ITT INDUSTRIES
2560 HUNTINGTON AVENUE
ALEXANDRIA, VA 22303
ATTN: C. FORE
ATTN: R. BRENINGER
ATTN: R. MCLAREN

ITT INDUSTRIES
P.O. BOX 15012
COLORADO SPRINGS, CO 80935-5012
ATTN: M. LYNCH
ATTN: T. STRINGER

KTECH CORPORATION
2201 BUENA VISTA, SE
ALBUQUERQUE, NM 87106-4265
ATTN: F. DAVIES
ATTN: D. LEPELL

NORTHROP GRUMMAN INFORMATION TECHNOLOGY
2100 WASHINGTON BOULEVARD
ARLINGTON, VA 22204
ATTN: I. VITKOVITSKY

TITAN PULSE SCIENCES DIVISION
2700 MERCED STREET
SAN LEANDRO, CA 94577-0599
ATTN: P. SINCERNY
ATTN: H. SZE
ATTN: S. WONG

OTHER GOVERNMENT

ITT INDUSTRIES
ITT SYSTEMS CORPORATION
1680 TEXAS STREET, SE
KIRTLAND AFB, NM 87117-5669
ATTN: DTRIAC 2 CYS